WA School of Mines: Minerals, Energy and Chemical Engineering

Department of Exploration Geophysics

Monitoring Pressure and Saturation Changes in a Clastic Reservoir from Time-lapse Seismic Data Using the Extended Elastic Impedance Method

Sergey Shevchenko

This thesis is presented for the Degree of Doctor of Philosophy

of

Curtin University

April 2023

Declaration

To the best of my knowledge and belief, this thesis contains no material previously published by any other person except where due acknowledgement has been made.

This thesis contains no material which has been accepted for the reward of any other degree or diploma in any university.

Sergey Shevchenko

Signature:…….

Date: …31/07/2023….

To my lovely wife Lena.

Abstract

Reservoir monitoring is an important aspect in the management of field development for optimisation of hydrocarbon recovery. Application of time-lapse seismic technology in this process makes it economically viable. This thesis presents an integrated study of the calculation of the pressure and saturation changes within the producing reservoir by applying the Extended Elastic Impedance (EEI) concept.

Based on AVO (Amplitude Versus Offset) principles, the EEI concept has been used by the oil industry in exploration and development projects mainly for the prediction of lithology and fluid. I propose and demonstrate a method that estimates pressure and saturation changes in the reservoir by applying EEI to time-lapse seismic data. The method is based on the fact that time-lapse seismic data processed at EEI specific χ angles using linearised EEI AVO crossplot projections can discriminate changes of particular rock properties in the producing reservoir that relate to changes in reservoir pressure and water saturation. The technique has been tested successfully to detect and discriminate both pressure and saturation changes at the producing Enfield oil field in the North West Shelf of Western Australia, where water injection wells were used to enhance oil production. The reservoir has complex geological settings and is complicated by compartmentalization. It is also impacted by the thin bed effect in parts of the field.

One can determine the EEI rotation angles that are optimally sensitive to changes in water saturation and pressure. I obtained an optimal EEI rotation angle χ=+42° for saturation changes by applying the Gassmann fluid-substitution approach to log data from the Enfield wells, and then using the ln(AI) and ln(GI) crossplot method. I obtained an optimal EEI rotation angle χ=-79° for pressure changes using the field operator's rock-physics model, based on laboratory velocity-pressure data measured on Enfield well core plugs.

While those EEI rotation angles are, respectively, the most sensitive to changes in water saturation and pressure, they are not necessarily uncontaminated by changes in the other parameters. The EEI angle for shear moduli, found to be χ=-60° for Enfield from log data, can also be used for pressure prediction as it should not be affected by the fluid changes. Qualitative analyses show the mapped distribution of EEI changes in shear modulus angle (-60°) is very similar to that of the optimal pressure-changes angle (-79°) obtained from rock-physics data. On the other hand, the rotation angles often found to be useful for exploration and development for bulk modulus (χ=+13°) and Lamé parameter (χ=+21°) appear to be much less useful for time-lapse monitoring of fluid-saturation and fluid-pressure changes.

All the rotation angles listed above were applied to the time-lapse seismic data at Enfield. Seismic reflectivity and inversion domains were used for comparison and analysis as the final rotated volumes. As expected, the results for these two domains are similar but the inversion results are noisier than the seismic reflectivity results.

I analysed the reliability of seismic volumes utilising normalised root mean square function (NRMS) and found that the volumes rotated to small angles showed high repeatability, but the volumes rotated to larger angles showed lower repeatability. Therefore, the large-angle rotated volumes should be used cautiously.

The limited access to company reports, low reproducibility of the publicly available seismic data and the complexity of the reservoir architecture limited my interpretation and results. Nonetheless, my qualitative and quantitative results are encouraging and supported by field production data.

This technically simple approach should be useful in the analysis of time-lapse seismic data processed by modern techniques and would help the management of reservoir using straightforward procedure.

ACKNOWLEDGMENTS

I would like to express my deep gratitude to Professor Wayne D. Pennington from Michigan Technological University for his genius to my opinion idea that led to the basis of this thesis, and also for his guidance, patience, and generosity in helping me with this project. I would also like to thank Professor Boris Gurevich from Curtin University for the support, and valuable and constructive suggestions during the planning and development of this research work.

I would also like to thank Robert Verstandig for his prompt help with IT support.

Table of Contents

List of Figures

List of Tables

Chapter 1

1. Introduction

An important objective of oil and gas field development is maximizing hydrocarbon recovery from producing reservoirs. A key factor in this process is the reservoir monitoring methods that allow observing changes in the producing reservoirs over time. The technology can monitor the changes in reservoir fluid saturations, measure past and current locations of displacing fluid fronts, and subsequently predict how these fluids will be distributed in the future.

The traditional way to monitor the reservoir is using data from the wells (Murphy, 1952). The advantages of the method are that well data show accurate changes in pressure, water cut, gas/oil ratio, and temperature showing the changes in the reservoir dynamics. The main limitation of the method is well information is only limited to the proximity of the wellbore, and infill wells are expensive. The well-based monitoring particularly becomes problematic when the reservoir has inhomogeneous lithology and structural complexity, which is very common.

In the 1990s, oil companies began to use time-lapse or 4D seismic surveys (repeated 3D surveys acquired at intervals of between several months and several years) to observe seismic data changes caused by changes in elastic properties of rocks. Time-lapse seismic gives an overall view of the reservoir and shows what is happening between wells. These surveys improve reservoir management by detecting structural and lithological compartments, circumventing geological zones, detecting gas coming out-of-solution, and monitoring water and gas movement during reservoir production. The introduction of 4D seismic has led to increased flow rates, improved reservoir recovery factors, and reserves calculation of the fields. Additionally, it helps in the planning of infill drilling and reduces the risk in the well

success rates. Therefore, 4D seismic complements Enhanced Oil Recovery (EOR) procedures already used by reservoir engineers and has proved to be a valuable tool (Jack, 2017). Yet, the seismic interpretation in the early years of 4D seismic was mostly qualitative.

In the 2000s, the quality of acquisition and processing of seismic data improved dramatically. For example, the enhancement of the accuracy in positioning data from earlier surveys and then carefully repeating tidal and equipment states, plus the use of steerable sources and streamers, were developed in response to the 4D survey needs.

These developments allowed the seismic data interpretation to provide more accurate seismic reservoir characterization by applying Angle Versus Offset (AVO) and pre-stack inversion techniques. The monitoring of the changes in reservoir fluid saturation and pressure are among them and are most critical in reservoir monitoring. Differentiating between fluid and pressure changes is challenging, as they can work in opposite ways. For example, when water is injected into a reservoir to support oil production, the pore pressure tends to increase. In this case, the reservoir matrix expands, cracks open, and therefore the rock softens, resulting in decreasing acoustic impedance from seismic data. At the same time, when injected water replaces oil, the acoustic impedance increases. Thus, changes of acoustic impedance alone cannot differentiate between pressure and saturation changes. However, analysis of AVO attributes (such as elastic impedance (EI)) can resolve these issues.

For most reservoirs, pressure effects in combination with fluid saturation effects create changes in seismic response, and it is often difficult to separate between the two effects from conventional seismic data. There are of course other production-related changes that also will have an impact on time lapse seismic data, for instance, gas injection, temperature changes, etc. In this study, however, the focus is on developing a methodology for discrimination between pore pressure and fluid saturation changes, assuming that other effects are negligible within the area of interest that covers oil and water legs.

Chapter 2

2. Background

2.1 Amplitude versus offset (AVO) method

In the 1960s and 1970s, quantitative interpretation of seismic data was largely based on post-stack inversion, which, for each layer, provided one parameter: acoustic impedance (a product of P-wave velocity and density). In the 1980s, an AVO method was developed, based on the idea that the change of reflection coefficient with the angle of incidence can provide additional information about the shear modulus variations (since at oblique incidence, P wave reflection and refraction involves energy conversion into reflected and transmitted S-waves). Mathematically, the angular variation of the reflection coefficient is described by Zoeppritz's (1919) equations as a set of four simultaneous equations. These equations are complicated and cumbersome to use in many applications. Subsequent authors, such as Bortfeld (1961) and Richards and Frasier (1976) simplified the equations to one using assumptions of weak contrast between elastic properties of adjacent layers. Aki and Richards (1980) and Shuey (1985) further simplified them resulting in equations that have enjoyed popular usage in practical applications.

Aki and Richards (1980) described the P-wave amplitude response as a function of angle θ at an interface as linearization of the Zoeppritz equations where the P-wave reflection coefficient R_p is a function of P-wave velocity V_p, S-wave velocity V_s, and density ρ, with subscripts (1,2) indicating the overlying and underlying formations, respectively:

$$R_p(\theta) = A + B\sin^2\theta + C\sin^2\theta\tan^2\theta, \tag{1.1}$$

where

$$A = \frac{1}{2}\left(\frac{\Delta V_p}{V_p} + \frac{\Delta\rho}{\rho}\right),\ B = \frac{\Delta V_p}{2V_p} - 4\left(\frac{V_s}{V_p}\right)^2\left(\frac{\Delta V_s}{V_s}\right) - 2\left(\frac{V_s}{V_p}\right)^2\left(\frac{\Delta\rho}{\rho}\right),\ C = \frac{1}{2}\frac{\Delta V_p}{V_p},$$

$$\Delta V_p = V_{p2} - V_{p1},\ \Delta V_s = V_{s2} - V_{s1} \text{ and } \Delta\rho = \rho_2 - \rho_1,$$

$V_p = \frac{V_{p2} + V_{p1}}{2}$, $V_s = \frac{V_{s2} + V_{s1}}{2}$, $\rho = \frac{\rho_2 + \rho_1}{2}$ and $\left(\frac{V_s}{V_p}\right)^2 = \frac{(V_{s1}/V_{p1})^2 + (V_{s2}/V_{p2})^2}{2}$.

Shuey (1985) reformulated the Aki and Richards (1980) approximation in terms of V_p and Poisson's ratio. For moderate angles of incidence, the third term in both Aki and Richards (1980) and Shuey (1985) approximations, which scales with $\sin^2\theta\tan^2\theta$, is negligibly small, and thus it is common to use a 2-term approximation

$$R_p(\theta) = A + B\sin^2\theta\,. \tag{1.2}$$

The term *A* is often called the Intercept (or zero-offset reflection R_0) and *B* the Gradient. Equation (1.2) enables one to calculate the reflectivity at any incident angle and therefore to generate seismic datasets that effectively differentiate and highlight lithology and fluids at specific angles. Importantly, two terms can be visualized in an AVO crossplot.

2.2 Extended Elastic Impedance

EEI methodology has been used in the exploration and development projects for the oil and gas industry for the last twenty years. It was introduced by Whitcombe (2002) and mainly has been used for lithology and fluid prediction using AVO analysis of seismic data.

Connolly (1999) introduced Elastic Impedance (EI) as a generalisation of acoustic impedance for variable incidence angle and defined it as:

$$EI(\theta) = V_p^a\, V_s^b\, \rho^c, \tag{1.3}$$

where $a = 1 + \sin^2\theta$, $b = -8k\sin^2\theta$, $c = (1 - 4k\sin^2\theta)$, $k = \left[\frac{V_s}{V_p}\right]^2$.

The EI concept gained popularity as a way of visualizing the linearised AVO over the observable range of incident angles (Connolly, 1999; Hendrickson, 1999). Whitcombe (2002) improved on this technique through normalisation by average values of V_p, V_s, ρ, defining the normalised EI as:

$$EI(\theta) = V_{po}\,\rho_o\left[\left(\frac{V_p}{V_{po}}\right)^a\left(\frac{V_s}{V_{so}}\right)^b\left(\frac{\rho}{\rho_o}\right)^c\right],$$

where V_{po} = average V_p, V_{so} = average V_s, ρ_o = average ρ.

The visualization of these parameters is usually done in a crossplot of B versus A (Gradient versus zero-offset amplitude). Whitcombe et al. (2002) extended the linearised EI AVO crossplot projections by relating the angle of incidence, θ, to an angle of axis-rotation, χ by $\sin^2\theta = \tan\chi$, yielding

$$EEI(\theta) = V_{po}\,\rho_o \left[\left(\frac{V_p}{V_{po}}\right)^p \left(\frac{V_s}{V_{so}}\right)^q \left(\frac{\rho}{\rho_o}\right)^r\right] \quad (1.4)$$

where $p = \cos\chi + \sin\chi$, $q = -8k\sin\chi$, $r = \cos\chi - 4k\sin\chi$.

Whitcombe et al. (2002) also demonstrated that important rock-physics parameters correspond to optimal χ angles. They used Gardner's rock parameters (Gardner et al., 1974) to calculate optimal χ angles for bulk modulus χ=+12.4° and Lame's parameter χ=+19.8° but both can be within the range from χ=+10° to χ=+30°. The shear modulus corresponded to χ=-51.3° (ranging from χ=-30° to χ=-90°). Those authors proposed to use angles χ=+12.4° and χ=-51.3° for discriminating geological parameters such as fluid and lithology effects respectively (Table 1). This concept is commonly used in exploration and field development studies (e.g., Simm and Bacon, 2014).

The EI concept can be extended to Aki and Richards (1980) 3-parameter linearized solution (Eq. 1.1), which includes additional estimation of the density parameter ρ (Ball et al., 2018); but it is often impractical because the third term is very noisy in real seismic data; this is beyond the scope of this study.

2.3 Time-lapse seismic data applications for reservoir monitoring

Monitoring of the producing hydrocarbon reservoir using time-lapse seismic data has been of strong interest for geoscientists in the field development for at least the last twenty years. Tura and Lumley (1999) introduced and applied a method to discriminate reservoir pressure and water saturation changes for time-lapse seismic data for a field in the Gulf of

Mexico. It was based on angle dependency of P-wave reflection amplitudes using pre-stack inversion for both P-wave and S-wave impedance changes over the reservoir. They also demonstrated that time-lapse AVO data can be used to exploit the fact that the shear modulus is generally sensitive to pressure changes and that fluid saturation changes affect the bulk modulus. The method allowed them to quantitatively estimate pressure or saturation throughout the reservoir by calibrating the seismic amplitudes in the time-lapse AVO crossplots with well production under the assumption that only pressure and saturation significantly change during production.

Brevik (1999) developed and evaluated quantitative method to estimate changes in saturation and pressure in the reservoir using various time-lapse seismic amplitude and travel time related properties. He presented a least-squares inversion method based on a rock physics model to invert P- and S-wave travel time differences for pressure and saturation changes and tested it on a synthetic model.

Merkel et al. (2001), predicted the effect on acoustic properties of the reservoir from the pressure and saturation changes as the result of field production. They used Duffy and Mindlin (1957) acoustic models along with the well logs, laboratory core measurements and downhole testing data. The reservoir was a turbiditic clean well-sorted sand with 27-29% porosity from the oil field in the Gulf of Mexico. The measured acoustic properties of the reservoir, under the in-situ varying conditions of pressure and saturation, were compared with theoretical predictions.

Landro (1999, 2001), derived formulas for computing saturation- and pressure-related changes from time-lapse seismic data and tested the method on the Gullfaks field at North Sea. Mathematically, he solved the changes in pressure and fluid saturation as separate equations with the coefficients of the Ro (Intercept) and G (Gradient) as the parameters. Then he used near- and far- offset stacks as an input data to calculate Ro and G coefficients in

order to compute volumes representing changes in pressure and fluid saturation. Additionally, he applied regression coefficients as the functions of the reservoir rock and fluid properties. He revealed that some leakage problems were observed from the pressure attribute cube into the saturation attribute cube and vice versa with fewer leakage problems. The method nevertheless discriminates well between fluid-saturation and pore-pressure changes.

Meadows et al. (2002) conducted a rock physics study for the Schiehallion field in the North Sea using laboratory core measurements to derive the dry bulk moduli (K_{dry}) and shear moduli (μ_{dry}) as functions of porosity (φ) and effective pressure (P_{eff}). They used dry compressional velocity, shear velocity, dry bulk density and porosity measurements from well cores. They presented two conclusions that provided the link between changes in rock and fluid properties and the resulting seismic data response for time-lapse studies. First, K_{dry} vs P_{eff} core measurements fitted best by a logarithmic function and the μ_{dry} vs P_{eff} data fitted best by a polynomial curve. Second, 2D surface in 3D dimension fits of K_{dry} and μ_{dry} over porosity (φ) and effective pressure using all the core data simultaneously are more useful and accurate than separate 1D graph fits over φ and P_{eff} for each individual core.

Cole et al. (2002) presented a method to estimate pressure and saturation from 4D seismic pre-stack data attributes based on a nonlinear rock physics forward modelling inversion method, and applied it to a data set from Schiehallion field in the North Sea. They used P and S time-lapse impedance changes as an inversion input, using rock physics model of pressure and saturation change based on laboratory measurements of core samples. The output was maps of pressure and saturation changes. The results agreed with the expected pressure increase near injector wells and decrease near most producers. The saturation results, however, were problematic as they showed gas saturation increases near several injectors, which is unlikely due to water injection at these wells. The authors also proposed a method to quantify the uncertainties as sensitivity functions in pressure and saturation estimates.

Lumley et al (2003) developed a crossplot inversion method to estimate pressure and saturation changes using time-lapse seismic attributes and applied it to the Schiehallion and Gullfaks oil fields producing reservoirs in the North Sea. In both these fields the injector wells were used to support production from clastic reservoirs. The authors used time-lapse prestack seismic attributes that were calculated and extracted such as Near and Far offset or angle amplitudes, AVO attributes such as Shuey's A and B parameters, and prestack seismic inverted P-wave and S-wave data that crossplotted against each other. Pressure and saturation change maps were calculated using these attributes.

Some previous studies have also been undertaken at Enfield field, where high-pressure water-injection assisted production, and where our approach is tested. Two studies and the interpretation by operator (Woodside Energy) of this field are of particular interest here as I compare them with my results.

Smith and others (Smith et al., 2008) monitored pressure and saturation effects as the results of production using 4D seismic at Enfield. They observed the differences as "soft" and "hard" amplitude anomalies from full stack data as pressure and saturation change, respectively. They also modelled pressure and saturation changes for appraisal wells, using log-based models, core data and synthetic seismic with the results as intercept and gradient plot for each well. The plot presented the best fit for water saturation and pressure changes as χ=+60° and χ=-50° respectively as an average for four wells (Appendix A, A.5, Figure 31). Then they used modelling results to create pseudo-pressure and pseudo-saturation differences as the attribute maps (Appendix A, A.5 Figure 41).

4D inversion volume interpretation was conducted by the operator for the field using Acoustic Impedance and Poison Ratio data in crossplots and as ratios to map changes in the pressure and gas or water saturation presented in Appendix A, A.5, Figure 40b (Smith, 2008).

Saul and Lumley (2015) also studied changes in pressure at Enfield 4D seismic data. They developed a method based on rock physics diagnostics to define the pressure sensitivity of rock properties including changes in the grain contact cement. They observed changes in near- to mid-angle stack seismic amplitudes and inferred from them changes within the reservoir as the result of pressure increase and suggested that the weakening of the sandstone matrix is a primary cause of these changes.

Some other efforts to apply EEI to time-lapse seismic data were presented by Dai and Mei (2014), who briefly presented an effort for the estimation of fluid saturation and pressure changes to an offshore Angola oil field. The authors did not provide a methodology for the χ angle calculation for pressure change (ΔP) and saturation change (ΔSw). They provided results as maps of ΔP and ΔSw with no geological, well positions, and other important information for the field on their maps that could help to analyse and assess their results. Oddly, they proposed to use the same angle $\chi = 10°$ for ΔP and ΔSw properties.

Chakrabortya et al. (2020) used modelled log data in a hypothetical case. They used log data from two wells collected at different stages of the production of the reservoir from the unknown producing gas field to model seismic synthetic response. They used data from these two well logs to correlate in terms of production-related petrophysical effects and to establish a time-lapse rock physics template. They used three types of lithology: shale, water sand and gas sands to calculate rock-physics parameters as bulk modulus, and shear modulus to generate elastic log response (Vp, Vs, Rho) at certain effective stress (as P pressure), porosity and saturation state. They used the above data to calculate ΔEEI (χ) using Whitcombe et al. (2022) formula for the previously modelled range of pressure/saturation conditions with the results as most sensitive angles for ΔP $\chi = 0°$ and ΔSw $\chi = +40°$. They used EEI domain template to calculate maximum sensitive angle $\chi = +5°$. Contradictory in the end, they just applied an orthogonal angle of 90° to the ΔSw $\chi = +40°$ to find $\chi = -50°$ as the most sensitive

for ΔP ignoring their calculated results. Thus, they have only been able to find the most sensitive angle χ for saturation change. Moreover, the authors have not applied their results to seismic data to verify the results.

Chapter 3

3. Approach

3.1 The concept

The change in seismic response in time-lapse data due to production can be caused by saturation and/or pressure changes. The saturation changes can be described by the Gassmann equation (Gassmann, 1951; Geertsma and Smith, 1961), which describes rocks in terms of bulk moduli of a two-phase medium (fluid and mineral matrix) and can be written as:

$$\frac{K_{sat}}{(K_o - K_{sat})} = \frac{K_d}{(K_o - K_d)} + \frac{K_{fl}}{\varphi(K_o - K_{fl})} ,$$

where K_{sat} is the bulk modulus of the fluid saturated rock, K_o is the bulk modulus of the matrix material, K_d is the bulk modulus of the dry rock frame, K_{fl} is the bulk modulus of the pore fluid and φ is the porosity.

The saturated bulk modulus (incompressibility) depends on the dry frame bulk modulus and on the relative incompressibility of the fluid in the pores. The bulk modulus is related to the compressional velocity V_p, shear velocity V_s and density ρ:

$$K_{sat} = \rho \left(\left(V_p\right)^2 - \frac{4}{3}(V_s)^2 \right).$$

The saturation changes affect the density ρ and therefore the bulk modulus K. The saturation change does not affect the shear modulus μ as fluids have no resistance to shear (Simm and Bacon, 2014):

$$\mu_{sat} = \mu_d,$$

where μ_{sat} is the shear modulus of the fluid saturated rock and μ_d is the shear modulus of the dry rock frame.

Note that the relative changes of porosity (and hence density) due to changes of fluid pressure are usually much smaller than relative changes of both bulk and shear frame moduli

(Hicks and Berry, 1956). This suggests that changes in density are indications solely of saturation changes, while changes in rigidity are indications solely of pressure changes. Therefore, the separation of the changes in density and shear modulus related to changes in seismic data would help isolate the changes in saturation and pressure respectively.
The shear modulus (rigidity) can be calculated using EEI applied to rock-physics data Whitcombe et al. (2002). They used Dong (1996) approximation of the Zoeppritz equation, which identified optimal angles for specific rock properties, and Gardner et al. (1974) rock-physics parameters as approximations to calculate shear modulus, bulk modulus and Lame parameter λ (Table 1).

I seek a streamlined approach to extracting pressure changes and fluid-saturation changes from time-lapse seismic data. In this study, I use available rock-physics studies to predict optimal EEI rotation angles for pressure changes to apply to time-lapse seismic data, and I also extract shear modulus changes from that seismic data, recognizing that this is exclusively related to pressure changes and not contaminated by fluid-saturation changes, although it may not be the angle that is most sensitive to pressure changes.

While one way to find changes in fluid saturation would be to seek an optimal rotation angle χ that is associated with density. However, seismic amplitudes are known to be relatively insensitive to density, particularly in a two-parameter approximation. Hence I use Gassmann modelling and predict a χ angle that is optimally sensitive to changes in fluid content and apply it to seismic data. To the extent that this angle is not contaminated by pressure changes, it can be assumed to reliably indicate changes in fluid saturation.

3.2 Application of EEI

I propose a method to utilize to differentiate fluid changes and pressure changes from time-lapse seismic data and illustrate this method on Enfield reservoir, where both changes co-exist during production at the locations above the oil-water contact (OWC), but where,

below the OWC, we expect only pressure changes from water injection. The method is based on use of EEI for pre-stack seismic data and uses angle rotations designed to optimize observation of changes in these two parameters. I used ΔRo (Intercept) and ΔG (Gradient) domain as the difference of Monitor minus Base survey time-lapse data as the amplitudes change from the seal-reservoir interface interpreted for both volumes. Figure 1 – Figure 3 (inspired by the figures of Simm and Bacon, 2014) show three simple models of changes within the reservoir due to production (pressure and/or saturation change): fluid-saturation change for oil sand to brine sand due to injection (Figure 1), fluid-pressure increase in brine sand below the oil-water contact due to injection (Figure 2), and changes in both saturation and pressure in the oil sand due to injection (Figure 3). Within each of these figures, (a) through (e) demonstrate AVO crossplot projections in three domains as follows: a – shows linearised two-term AVO plot with θ as the angle of incidence (Whitcombe et al., 2002), b – d - show rotation of the axes to the AVO crossplot angle χ with corresponding angle of incidence θ: $\sin^2\theta = \tan\chi$ (Whitcombe et al., 2002), e –amplitude difference of time lapse Intercept/Gradient volumes rotated at χ=0°, +13° and +42°. All data and illustrations in the thesis use positive standard polarity (Sheriff and Geldard, 1995), in which a positive zero-offset reflection coefficient corresponds to an increase in acoustic impedance.

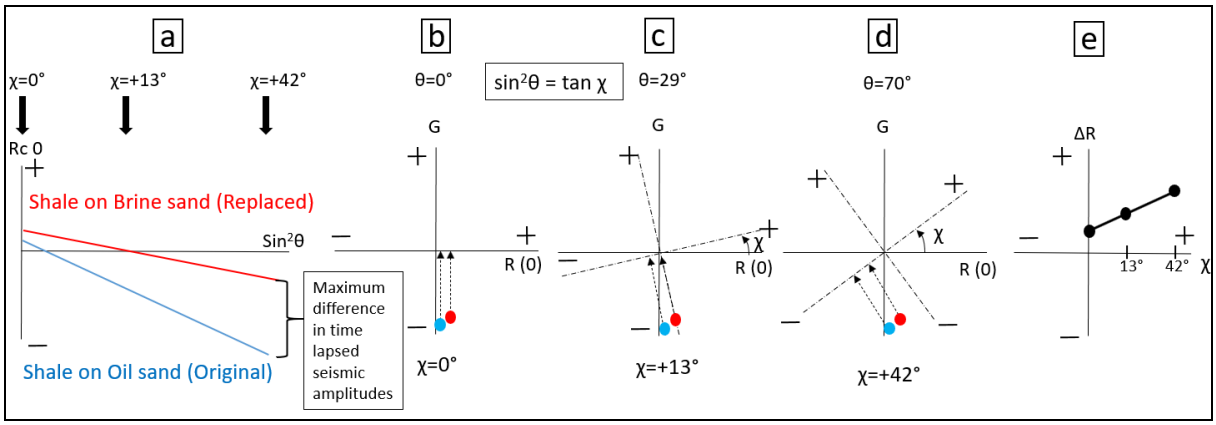

Figure 1. Simple model of shale over sand interface for time-lapse data due to a change in saturation only (oil to water as a result of brine injection). This and the following two figures also present the

model at three χ angles for rotated Intercept/Gradient volume corresponding to three different projection domains, and a summary diagram for three rotation angles of interest in each scenario. See text for a detailed explanation.

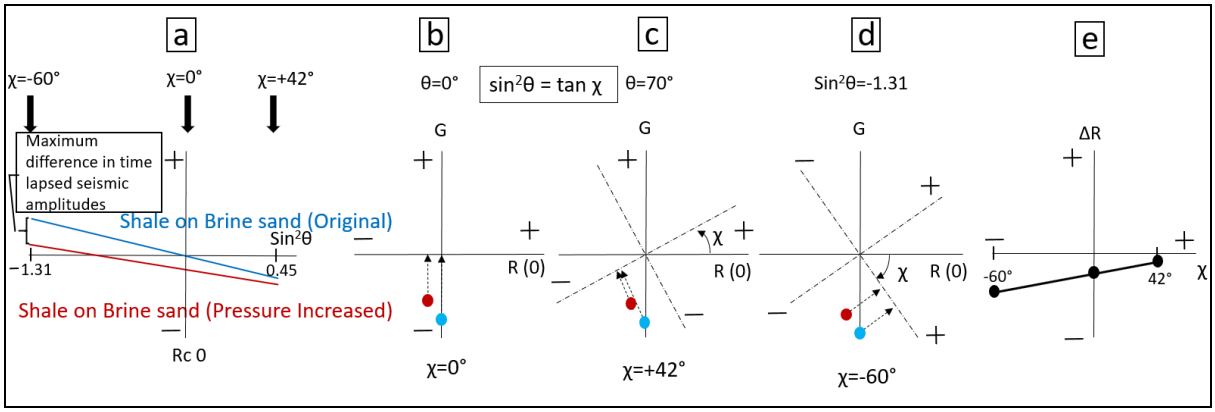

Figure 2. Simple model of shale over brine sand interface for time-lapse data due to a change in pressure only (as appropriate in the water sand below oil-water-contact) shown in presentations similar to those in Figure 1.

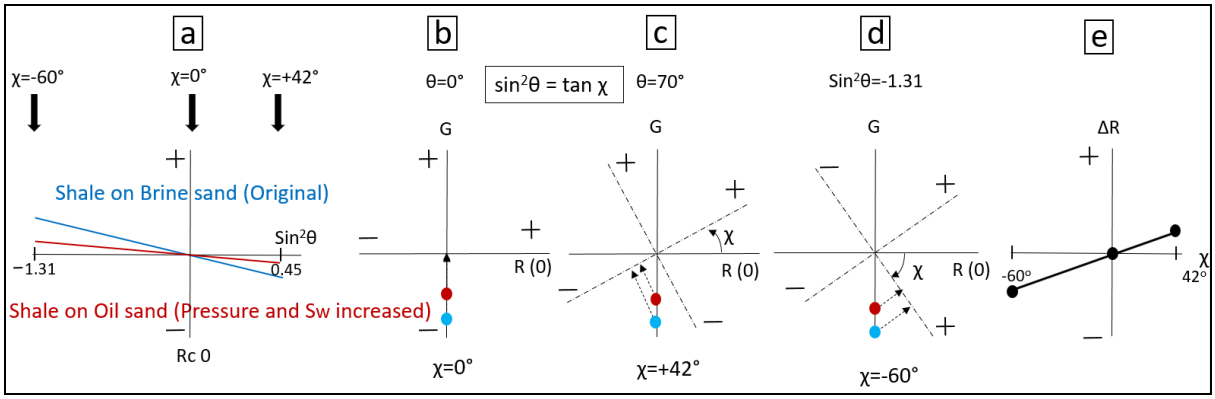

Figure 3. Simple model of shale over sand interface for time-lapse data due to changes in both pressure and saturation shown in presentations similar to those in Figure 1.

3.3 Pressure changes

As discussed in Chapter 1, the shear modulus is unaffected by fluid changes in the formation, but is affected by changes in effective pressure; as a result, a time-lapse change observed in EEI at an angle corresponding to a shear modulus change should indicate changes in effective confining pressure, and not changes in fluid content. This implies that

the χ angle for the shear modulus change should be 90° from the angle for fluid changes; this observation may be useful in evaluating other predictions of optimal angles, or the validity of Biot-Gassmann and other assumptions in any individual study. The angle χ corresponding to the shear modulus change can be computed by calculating it from logs (Table 1), and is often found to be -50° to -60° (Whitcombe et al., 2002).

An alternative approach to find the angle most sensitive to pressure changes is through laboratory studies of core samples, or by making assumptions of the lithology and using comparisons with other rocks whose pressure response is known. Such an approach may give an angle that may not be 90° from the fluid saturation angle. The decision as to which approach (shear-modulus angle or most-sensitive angle) to use in the future studies may depend on what data are considered more reliable. It may be advisable to use both approaches and compare the results.

3.4 Fluid saturation changes

Through Biot-Gassmann we know that the bulk modulus is affected by fluid changes, but the bulk modulus is also affected by changes in effective confining pressure, so the bulk modulus should not be used as the fluid indicator in time-lapse studies where appreciable pressure changes may be expected. Perhaps the most straightforward method is to model the predicted changes in elastic properties (and AVO behaviour) from fluid substitutions from log data and use the rotation angle that is found to be optimal to observe those changes. Alternatively, the orthogonal angle can be used to that is most sensitive to changes in pressure; this angle would be sensitive to anything other than pressure, and because we assume only fluid changes and pressure changes take place in the reservoir, the angle would correspond only to fluid changes, even if not optimally sensitive to them.

A note on orthogonality and optimal sensitivity: In a world designed for the convenience of geophysical interpreters, the χ angles most sensitive to pressure changes and to fluid

changes would be 90° apart. Unfortunately, it appears that in many cases the angles are nearly orthogonal, but not exactly. The investigator may wish to examine five angles, two of which are optimally sensitive to pressure changes and to saturation changes, two of which are orthogonal to those, and the angle for shear modulus. One would hope that the angle optimal for saturation changes is nearly orthogonal to that for shear modulus, in which case those are the only two angles needed; one's definition of "nearly orthogonal," however, should be backed up by comparisons with results from the other angles.

Chapter 4

4. Enfield 4D seismic data

4.1 Geological settings

The Enfield oil field is located within the Exmouth Sub-basin of the offshore Northern Carnarvon Basin, which is on the North West Shelf on Australia's continental margin (Figure 4). The sub-basin contains Triassic to Quaternary sediments (Figure 5). Initially, during the Mesozoic Age, the area underwent a phase of intra-cratonic sag, resulting initially in the deposition of the Locker Shale as deep marine sediments and subsequently the fluvio-deltaic Mungaroo Formation. During the Late Triassic and Early Jurassic, subsidence had become restricted with the development of the Exmouth Sub-basin rift basin. Two rifting events took place during development of the basin. First, the rifting and breaking away of Argo Land in the Early-Mid Jurassic. Second, the rifting and breaking away of Greater India in the Early Cretaceous.

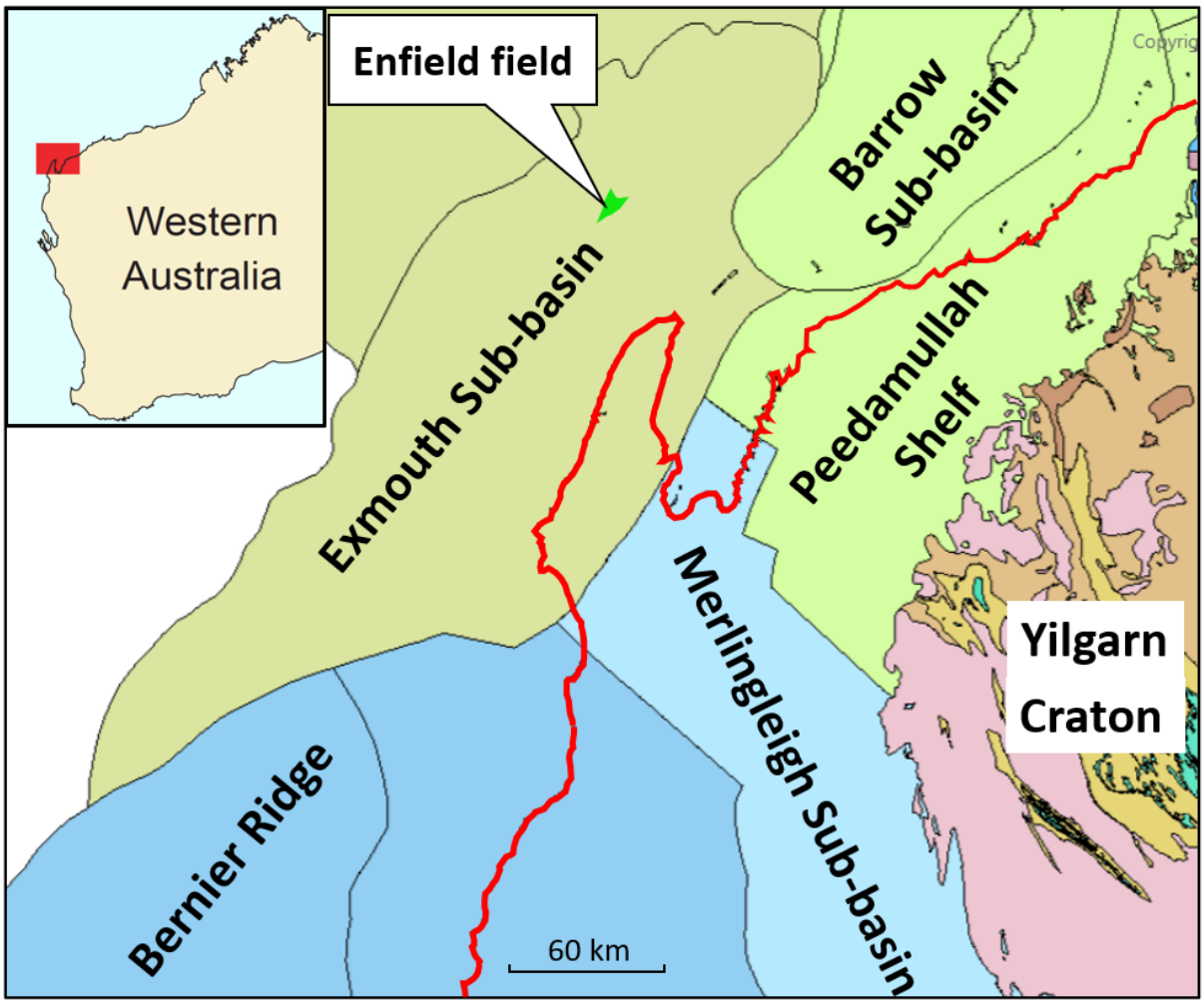

Figure 4. Major tectonic units of the Northwest Shelf Region (modified from GeoVIEW.WA GIS-based mapping system available in the public domain. Government of Western Australia Department of Mines, Industry Regulation and Safety).

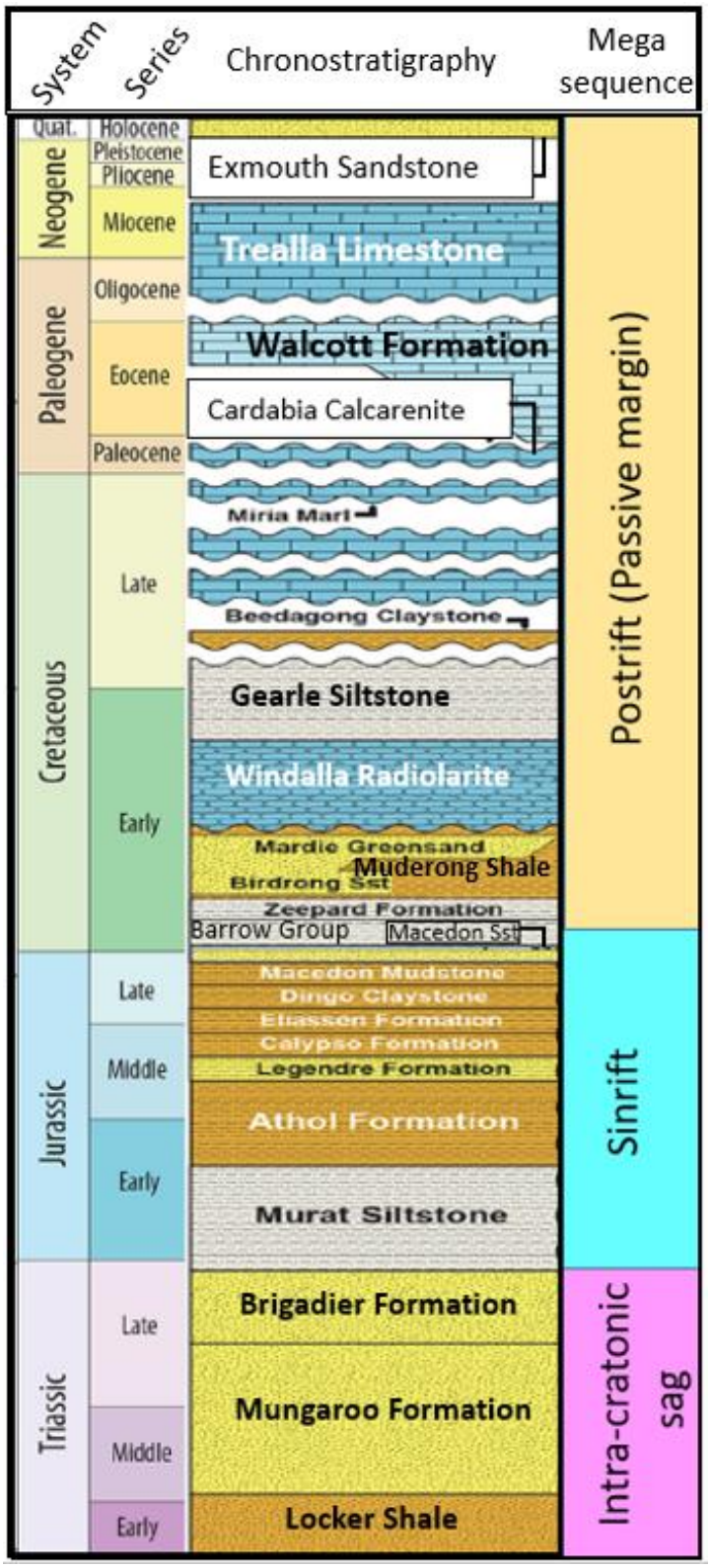

Figure 5. Simplified Chronostratigraphic chart with the main tectonic development phases of the Exmouth Sub-Basin, modified from Longley et al., (2002).

Throughout Early to Mid Jurassic, the basin experienced a deep-water environment with deposition predominantly of fine-grained sediments. By the end of the Jurassic, during the first rift phase, a relic basin topography remained. In this environment, the Barrow Delta was deposited with sedimentation of the Barrow Group during the second Early Cretaceous syn-rift period.

The Macedon Sandstone of the Enfield reservoir was developed as the basal part of the Barrow Group. It was deposited during a lowstand, which represents the onset of the tectonism (uplift in the south of the basin and downwarp to the north), resulting in the formation of the overlying Barrow Delta. Early deposition of the Macedon Sandstone appears to have been in a shallow water shoreface environment but was later formed by turbidity deposits in a deep water environment. The channels that transported sediments into the basin through structurally controlled topographic lows such as submarine canyons have been identified by various investigators (Tindale et al. 1998, Bussell et al., 2001).. These channels are oriented parallel to a series of large-scale northeast trending terraces that step down to the west and have a major impact on basin topography. The Macedon Sandstone is overlain by the Macedon Mudstone that represents distal clays of the northwards prograding Barrow Delta (Willis, 2003).

From Early Cretaceous, the main tectonic event was the break-up and departure of Greater India from Australia, resulting in the development of the North West Shelf into a passive margin. The Barrow Group sediments were reworked and deposited as the Birdrong Sandstone, later overlain by the Mardie Greensand, a glauconitic-rich transgressive sequence deposited in a shallow shelf environment. Next sequence was the deposition in a deep marine environment of the Muderong Shale as a regional seal caused by a significant sea level rise over the basin. The Gearle Siltstone and Beedagong Claysone were deposited as the

siliciclastic sedimentation continued into the Late Cretaceous, later developing into a carbonate system, which continued through the Tertiary up to the present day (Willis, 2003).

4.2 Enfield field setting

The Enfield oil field, which produced oil from 2006 to 2017, is located within the offshore Carnarvon Basin in Western Australia and was operated by Woodside Petroleum. The field is a north-westerly dipping structure sealed laterally by two major normal faults (Figure 6). The reservoir rocks are Late Jurassic "soft" Macedon Sandstone of average 24% porosity sealed by "hard" Macedon Mudstone. The reservoir consists of an Upper Reservoir of amalgamated turbidites with 10-25m thickness and a Lower Reservoir of locally developed channelised turbidites with thicknesses of over 50m (Figure 7). The two reservoirs are separated by 1-2m thick shales interpreted as a major flooding surface. Numerous faults combined with the relatively thin reservoir and a complex depositional architecture created a limited fluid flow pathways, baffles and barriers that are difficult to predict (Hampson, 2012; Smith et al., 2008).

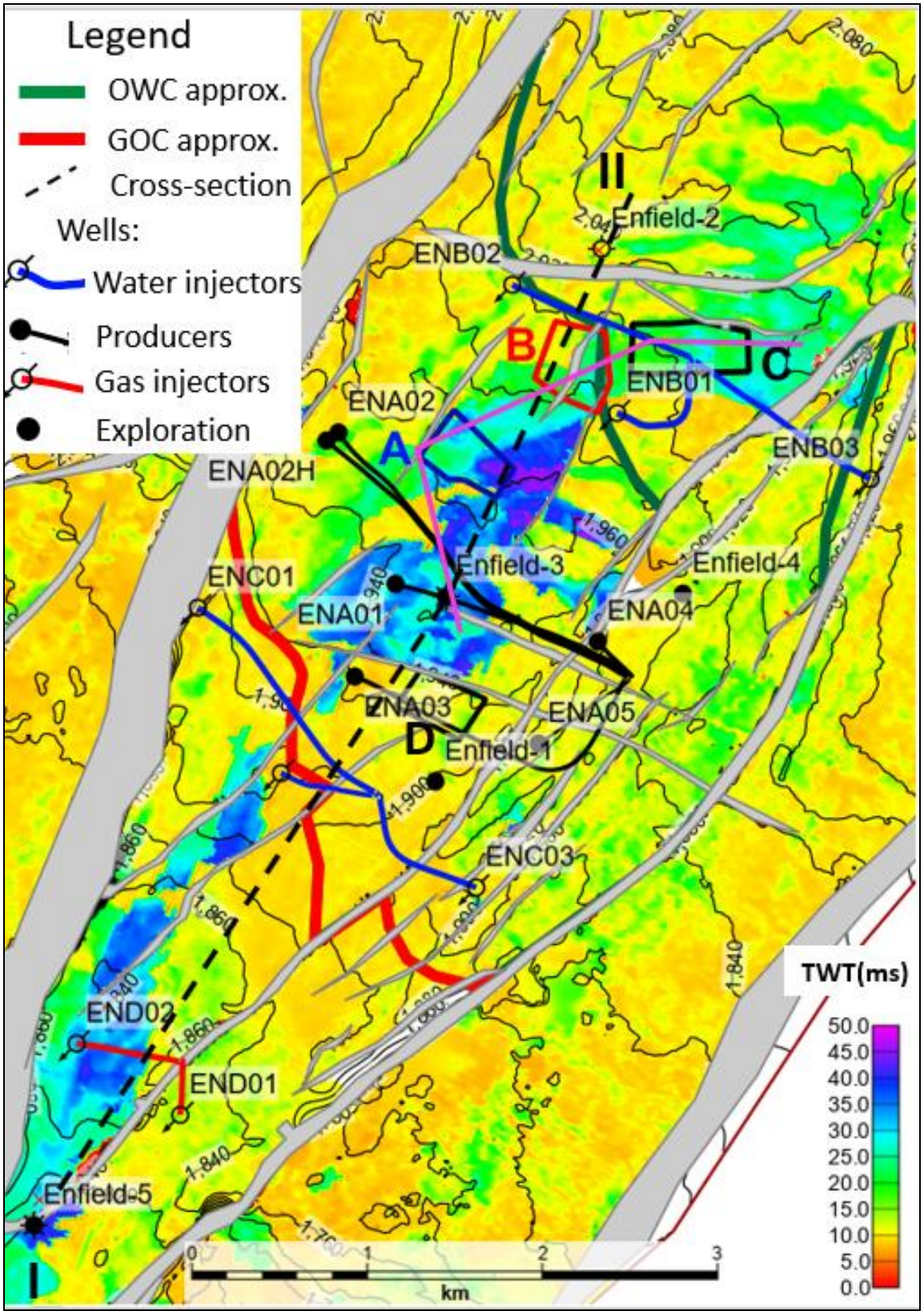

Figure 6. Enfield two-way time structural map shown as labelled contours to Top Macedon sandstone (ms) and Isopach Macedon sand reservoir shown as the colour. The labelled polygons are areas in which quantitative studies were conducted, and injection and production wells at the time of Monitor

survey are shown. General dip is down to the northeast. The thin-bed artifacts in the seismic data were determined by the modelling for the reservoir thickness 10ms and less (Appendix B, B 2.4). This is consistent with other authors (Saul and Lumley, 2015). I-II dash line is the seismic cross-section in Figure 7 below. Seismic synthetic modelling arbitrary line is shown as magenta line.

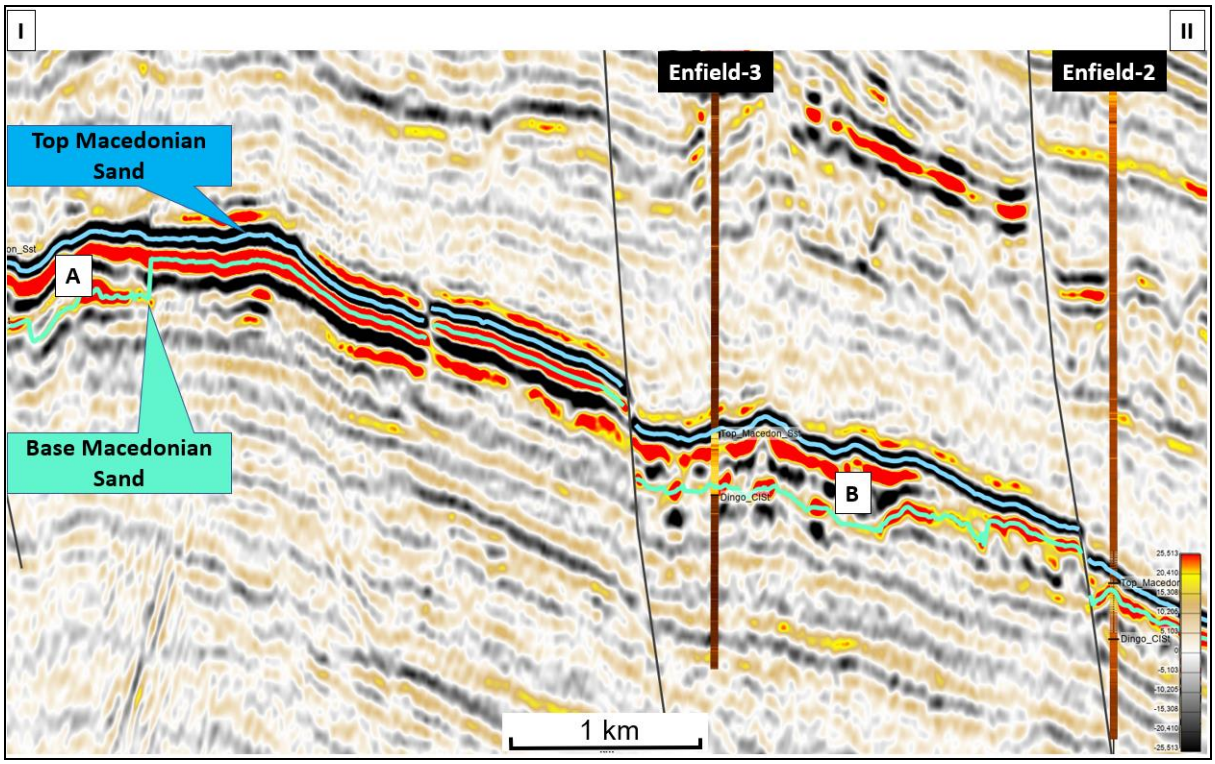

Figure 7. Interpretation of the Top and Base Macedonian reservoir on the seismic cross-section I-II on Figure 6 through the wells Enfield-3 and Enfield-2. Thick channelised turbiditic sequence shown as A and B.

We have chosen Enfield for this study because it was developed using high-pressure water injection, some of it below the oil-water contact (OWC), where it underwent strong pressure changes without a change in fluid content, while other areas underwent both pressure and fluid changes. In addition, earlier time-lapse seismic studies showed that the elastic properties of the formation are pressure-sensitive (Smith et al., 2008; Saul and Lumley, 2015, Bentley, 2010).

Enfield 4D survey was the first dedicated time lapse survey in Australia. The baseline seismic survey was acquired in 2004 prior to development of the field (Han, 2004). The 2007 monitor survey was acquired in the same direction as the 2004 survey, repeating source and receiver positions as closely as possible in order to reduce 4D noise due to differences in ray paths. At the time of the monitor acquisition in 2007 (Wickham et al., 2007) the field had three horizontal and two deviated oil producers, two gas injectors in the gas cap, three deviated water injectors at the OWC and three deviated water injectors at the GOC (Figure 6). All listed geological and field development technical complexities made prediction of saturation and pressure changes from 4D data particularly valuable but also quite challenging.

4.3 Data quality and availability

The first baseline and first monitor surveys were initially processed by PGS in 2007 (Wickham et al., 2008). CGGVeritas reprocessed the same datasets in 2008 with higher-quality results as the technology for time-lapse processing was being developed contemporaneously (Chan et al., 2009). Unfortunately, the only data publicly available is that which was processed in 2007. The operator conducted another two time-lapse surveys in 2008 and 2011, but these data are not accessible to us. I used the initial Base seismic survey "BaseP" that was acquired in 2004 and the Monitor "M1P" survey was acquired in 2007, seven months after the field commenced oil production. (I use the "P" designation in order to emphasize that these processed data sets are not the same as those used by other investigators.) The two surveys (BaseP from 2004 and M1P from 2007) were processed by the same contractor, with the preservation of amplitudes with AVO studies in mind, in order to monitor changes in the reservoir due to production. The data consist of near (8°-18°), mid (19°-30°), far (30°-41°) and ultra-far (41°-51°) partial angle stacks and is of fair quality for AVO applications. The main problems associated with the data quality included: 1. Diffracted multiples from channels projected smiles into reservoir, and no the nearest offsets

on the monitor data correspond to about 8° angle of incidence. 2. Post migration CDP statics are very poor, so the gathers are not flat and are quite noisy (Chan et al., 2008). I improved the data quality by applying Residual Move Out (RMO) (details in Appendix B, B 1.6, Figure 53-54). I did not use the RMO corrected ultra-far stacks in this study due to their low quality (Figure 48).

The quality of the seismic volumes was assessed by calculating time-lapse seismic non-repeatability as normalised root mean square (NRMS) (Kragh and Christie, 2001, Kragh and Christie, 2002, Eiken et al., 2003). Because I found that the repeatability varies with offset, I also calculated NRMS for intercept and gradient volumes, and for the seismic volumes after rotation to angle ranges of interest to us (Appendix B, B 1.7, Figure 55-57). I found that the intercept volume demonstrated high repeatability, but the gradient volume was less repeatable. As a result, the volumes rotated to small angles also showed high repeatability, but the volumes rotated to larger angles showed lower repeatability; the large-angle rotations should be used cautiously (Figure 8).

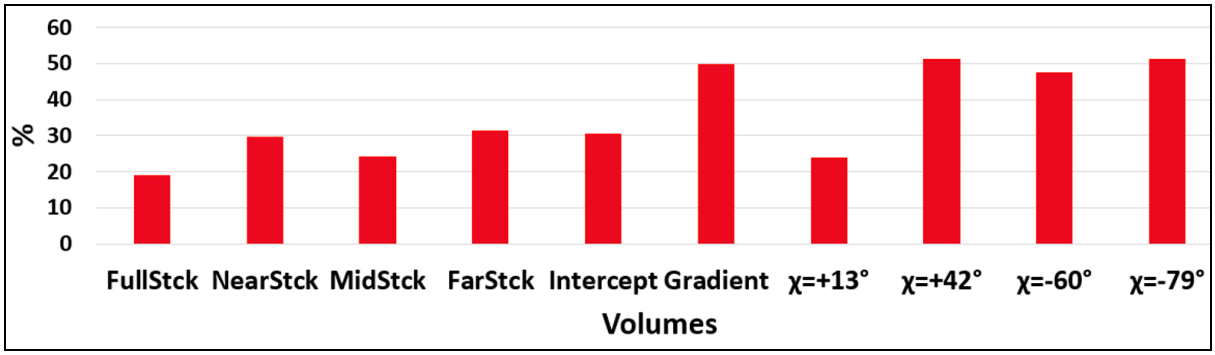

Figure 8. NRMS for seismic volumes within polygon A for time window covering from Top Macedon to 700ms above Top Macedon horizon.

The detailed description of data quality control and data conditioning is presented in the Appendix B chapter.

4.4 Seismic data processing and interpretation

4.4.1 General approach

Exploration and appraisal wells Enfield-1, 2, 3, 4, 5 (Figure 6) were used for structural interpretation and Enfield-2, 3, and 4 wells, having a publicly available full array of logs (V_p, V_s, Rho), were used in AVO and Inversion processing and interpretation. Top Macedon Sand horizons have time shifts between BaseP and M1P surveys up to -10 ms, mainly around injectors (Appendix A, Figure 21). This is likely the result of the collapse of the top reservoir due to high injection pressure damaging the formation by weakening grain contacts (Saul and Lumley, 2015). Therefore, rather than subtract one three-dimensional volume from another, I used values extracted along horizons within the BaseP and M1P volumes separately, and then obtained their differences (always subtracting the values of BaseP from M1P).

Previous investigators (Bentley, 2010; Saul and Lumley, 2015) found that thin-bed effects tended to overwhelm the AVO response in many parts of the field, and my observations are consistent with that. The detailed analyses of the thin bed's effect is presented in Appendix B, B 2.4. I restrict our detailed analyses to areas where the beds are relatively thick. I have chosen three polygons within the field, where I tested our model quantitatively. Polygon A is in the vicinity of the producer wells, roughly the same distance from the southern and northern injectors (Figure 6); here we anticipated little change in either the pressure or saturation. Polygon B is within the oil leg just above the OWC, where we expect an increase in both water saturation and pressure due to nearby injector ENB01. Polygon C is within the water leg and close to injector ENB01, where we anticipate a large increase in pressure but no change in saturation. To choose polygon shapes I used several constraints at the same time: 1. Similar size, but not necessarily equal as calculation of average values were used which does not affect the statistics. 2. Within a thick reservoir.

3. Away from the faults if possible. 4. The C polygon was intended to be similar as in Saul, M., and D. Lumley, 2015 work to compare results.

Commercial software DUG Insight, 2021 (DownUnder GeoSolutions) was used for seismic data processing and interpretation. This included modules: Explorationist, Image Gather Processing and Gather Attributes. For the inversion and AVO modelling I used CGG Hampson-Russell Software (GeoSoftware). Although there is no direct link between these two software packages, the compatibility and flexibility in communication between two packages to run a single project are excellent.

4.4.2 Structural interpretation

Two horizons were interpreted for structural interpretation using BaseP and M1P Full Stack volumes: Top Macedon Sand and Base Macedon Sand for both volumes. The horizons were tied to exploration and appraisal Enfield 1-5 wells using check-shot velocity data. Manual amplitude snapping was used for interpretation initially for every 5-10 Inline/Crossline (inline spacing is 25 m, and crossline is 12.5 m), depending on structural complexity, and then a propagator was used to accomplish the interpretation of the horizon. These horizons were used for amplitude extraction from seismic and inversion volumes.

4.4.3 Amplitude extractions

Amplitude extraction was performed for qualitative and quantitative calculations. The function of Simple Average Amplitude function with +5 ms and -5 ms extraction window from the interface between the seal (Macedon Mudstone) and the reservoir (Macedon Sand) was used to extract amplitudes for seismic reflectivity volumes. For inversion volumes, I used Top Macedon Sand – Base Macedon Sand window and Absolute Minimum amplitude extraction function.

4.4.4 Intercept/Gradient volumes computation

The final RMO corrected angle stacks of Near (8°-19°), Mid (19°-30°) and Far (30°-41°) were used to compute Intercept and Gradient volumes for BaseP and M1P surveys. At each sample, the process calculates the linear regression of the amplitudes using ordinary least squares and returns the Intercept, Slope and Goodness of fit (QC value) volumes. The Intercept and Slope of the regression line are the first two terms, A and B, in the two-term linearized Shuey approximation of the Zoeppritz (Eq. 1.2).

4.4.5 Amplitude versus Angle (AVA) angle rotation

Seismic reflectivity Intercept and Gradient attribute volumes were used to calculate AVA rotated volumes. The computation was done using DUG Insight software (DUG Insight, 2021) that uses the algorithm:

$$R(\chi) = \text{Intercept Volume} * \cos(\chi) + \text{Gradient Volume} * \sin(\chi)$$

where χ is the targeted rotation angle (Appendix A, A.2, Figure 22 − Figure 25).

4.4.6 Inversion processing

Model-based EEI inversion was done using a background model based on pre-production Enfield-2, Enfield-3 and Enfield-4 well logs for both the BaseP and M1P surveys. Ideally, it would be best to use the logs acquired at the time of the M1P survey. Initially, the operator planned to do logging of the wells drilled after Monitor survey but this was not done due to technical problems. Inversion for the rotated volumes was performed using CGG Hampson-Russell software. The Model-based inversion was utilized with soft constraints and a low frequency model derived from logs. The software calculates the Elastic Impedance logs for the targeted χ angles using P-wave, S-wave and density logs.

The Elastic Impedance for targeted χ angle, P-wave, S-wave and density logs was then used to invert AVA seismic reflection Intercept/Gradient targeted χ angle rotated volumes (Appendix A, A.2, Figure 22 −Figure 25).

Chapter 5

5. Application of EEI method to Enfield data

5.1 Saturation optimal EEI angle determination

The most straightforward method to model the predicted changes in elastic properties (and AVO behaviour) is from fluid substitutions based on log data and use the rotation angle that is found to be optimal to observe those changes. To determine EEI angle for the fluid saturation discriminant, I used AI vs GI crossplot method proposed by Whitcombe and Fletcher (2001). I used data from Enfield-2, -3, -4 wells for the pay zone, where fluid-substitution calculations were conducted by the operator for brine-, oil-, and gas-saturated conditions, using Gassmann fluid-substitution, log data, and perhaps other insights available to them (Martin, 2002). The resulting compressional sonic, shear sonic and density logs were digitised (from figures in that publication) for oil, gas and water fluid-substituted pseudo-logs for the pay reservoir zones including 20-30 meters of overburden and deeper shale layers.

These data were used to calculate ln(AI) vs ln(GI) at each depth point using (Eq. 1.4), where GI is EEI at 90° and AI is EEI at 0°. The "scatter" in the data (Figure 9) represents the varying lithologies present in the reservoir. I found the angle of the line segment that connects each depth point's oil-saturated and brine-saturated points, and that which connects each depth-point's gas-saturated and brine-saturated points. The average of these angles was found to be χ=+42°, interpreted as the optimal rotation angle for the identification of fluid changes. Instead of using k=0.25 value from (Eq 1.4) as a typical value (Whitcombe et al., 2002), I calculated it as an average of V_s/V_p for the pay zones and for each fluid substitution scenario.

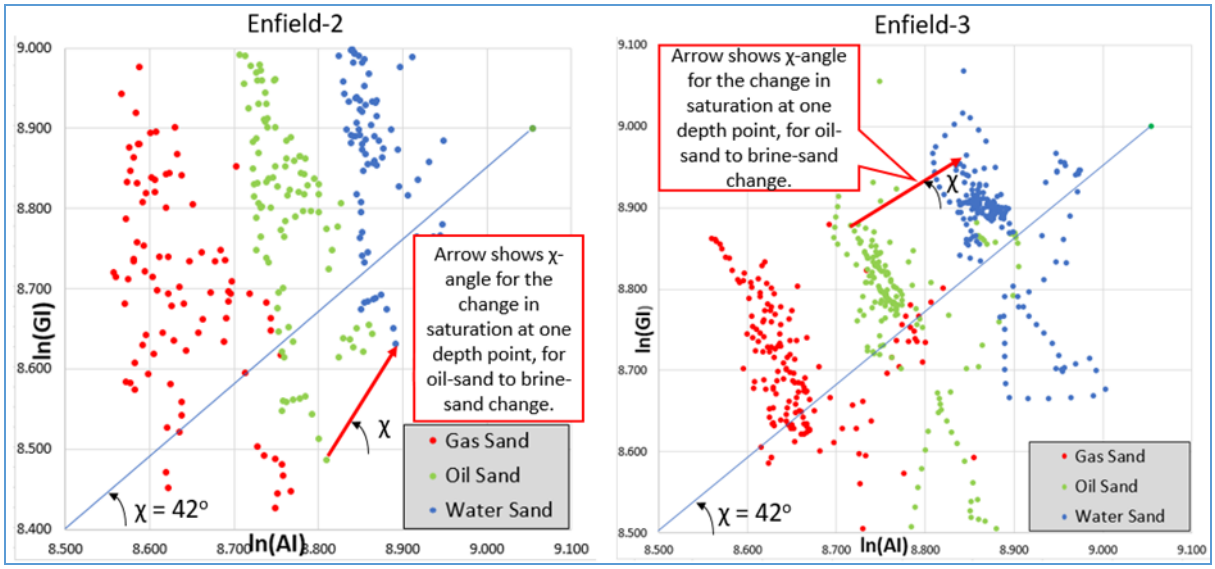

Figure 9. The ln(AI) vs ln(GI) crossplot calculated from Enfield-2 and Enfield-3 fluid-substitution results and the average angle $\chi = +42^{o}$ angle is shown as a vector from the origin. A single example of the change experienced by one specific data point is shown for each well for oil sand to water sand; the average of all such changes yields the +42° angle.

As +42° is predicted to be optimal for fluid changes, the angle orthogonal to it, -48°, should be the angle that is completely unaffected by fluid changes, and therefore affected only by pressure changes. However, due to the caveats mentioned earlier, that angle may or may not be the one that is most sensitive to pressure changes.

5.2. Pressure optimal EEI angle determination

To determine the EEI angle most sensitive to pressure changes, I used Enfield rock physics model of Wulff, et al. (2008). The model is based on taking laboratory velocity-pressure data measured on well core plugs and fitting them to MacBeth's (2004) model for dry and brine-saturated sandstones (Appendix A, A.3, Figure 26). As the publicly available data in Wulff, et al. (2008) were limited to normalised velocities and pressures; we assumed that they could be applied to in-situ Enfield-2 well pressure and log data, and solved for useful velocity-pressure pairs (Figure 10a). The following describes the procedure for solving the normalised velocity-pressure data.

In the Enfield-2 well, the reservoir formation is at a depth that corresponds to the effective pressure of 3220 psi (total stress minus pore pressure) at the discovery conditions (Appendix A, A.4, Figure 27). Compressional velocity V_p, shear velocity V_s and density values for this interval are from the well logs. We assumed that this in-situ pressure corresponds to normalised pressure 1.0, and the velocity values obtained from logs in that well were used to calibrate the normalized values to presumed in situ values. The rest of the normalised data, digitised from the published rock-physics model, was used to find the pressure-sensitivity of velocities for conditions corresponding to the reservoir in Enfield-2. The density value used to compute impedances from velocities was an average for the reservoir.

Then I used these data to calculate ln(AI) and ln(GI) to determine the angle of maximum sensitivity to changes in pressure. The ΔEEI values at each point were calculated using the equation (Eq. 1.4) (Appendix A, A.4, Figure 28) and plotted, along with values for ΔP (in psi) on the crossplot (Figure 10c).

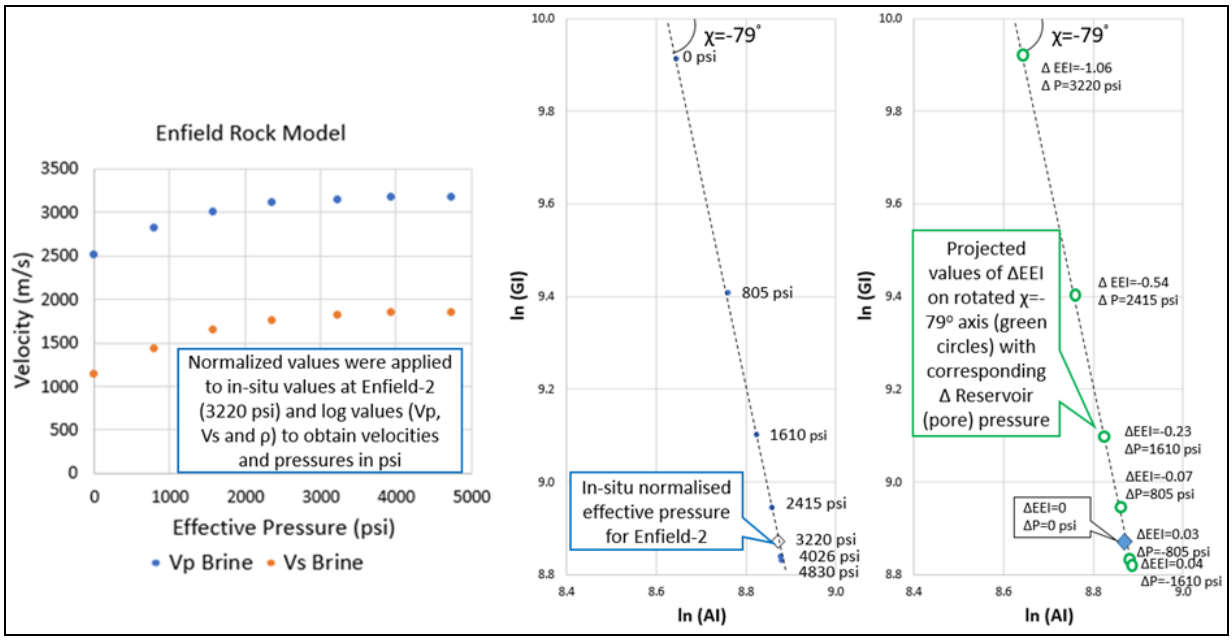

a) b) c)

Figure 10. Pressure-change calibration. a) The model was fitted to (psi) pressure units using Enfield-2 in-situ pressure condition (3220 psi). b) Calculation of optimal χ angle for pressure changes using the

velocities in (a) and appropriate densities to find ln(AI) and ln(GI), and, in turn, the best-fit line through those points. c) ΔEEI and ΔP (pressure) values projected on the χ=-79° axis.

The EEI angle for shear modulus or rigidity (μ), which is anticipated to be sensitive only to pressure changes, was calculated using commercial Hampson-Russell software for Enfield-2, -3 and -4 wells, and taken as the average. It uses compression, shear velocity and density logs for moduli calculation. For completeness and comparison with other studies, the χ angles for the K and λ moduli were also calculated as suggested by Whitcombe et al. (2002) using Gardner's relationship. The χ angle is found at the maximum correlation coefficient between the target rock-physics (λ, μ and K) parameter and EEI curves (Appendix A, A.4, Figure 29). Computation of the EI impedance log is based on Connolly (1999) equation (Eq. 1.3) and uses compressional velocity, shear velocity and density logs. These angles, as well as the results of the modelling for optimal fluid angle and optimal pressure angle are summarized in Table 1 below. I note that the angle (-48°) that is orthogonal to that which I obtained for fluid sensitivity (+42°) is close to those predicted for changes in the shear modulus (-51.3° or -60°), as one would expect.

Method of calculating EEI χ angle	Optimal χ angle (degree) for parameters:				
	K	Mu	Lambda	Fluid	Pressure
Commercial software for Enfield wells	+13	-60	+21		
Whitcombe et al., (2002), for Gardner's parameters	+12	-51.3	+19.8		
Smith et al., (2008), using Enfield wells data				+60	-50
Gassmann Fluid Subsitution using logs				+42	
Rock-physics model from core samples laboratory data					-79
Scanning, IntGrad volume χ rotation from -90° to +90°				+41	-55

Table 1. EEI optimal χ angles for rock-physics parameters from different sources and methods.

Smith et al., (2008) presented a time-lapse AVO model as the intercept and gradient difference crossplot calculated for four Enfield wells as the difference of saturation and pressure from initial oil conditions for each depth point. The plot represents the best fit angles

χ=+60° and χ=-50° for water saturation and pressure changes respectively (Table 1, Appendix A, A.4, Figure 31).

Another method I tested to find χ optimal angles for pressure and saturation, after having calculated reflectivity differences, is presented in detail in section 6.1.1, but is mentioned here in order to allow comparison in Table 1. I scanned the average seismic reflectivity amplitude differences M1P – Base1P for the three (A, B and C) polygons, over the range χ=-90° to χ=+90°. The average values were calculated for χ every 10°, with 5° near the minima (Figure 14). I found that the maximum amplitude difference (negative values) for polygon C (with no saturation change and only pressure change) was χ=-55°, and entered that in Table 1 for the angle most sensitive to the pressure change. The value for the angle most sensitive to fluid changes, obtained from polygon B (with maximum saturation change) was entered into Table 1 as χ=+41°. These results are discussed in section 6.1.1.

5.3 Pressure and saturation maps calculation and calibration

Seismic volumes rotated to various EEI angles can be interpreted qualitatively or quantitatively. In order to provide a qualitative interpretation, one can use difference volumes based either on inverted results (which provide actual units of impedance, albeit of an "elastic" version) or on simple rotations from A (or R_0, the zero-offset reflection amplitude) and B (or G, the AVO "gradient"). While the latter approach is straightforward, and its results are discussed in the following section, the former approach (using inverted volumes) requires additional explanation.

A quantitative interpretation requires a relationship between the values obtained at the rotated angles and the parameters of interest, such as the change in water saturation or the change in pressure in psi.

5.3.1 Pressure Change Prediction

To calculate the pressure change in psi units, I used the relationship between the pressure and velocities derived from Wulff et al. (2008) rock-physics model (Figure 10a). I used V_p, V_s and density values for each corresponding pressure value by applying Whitcombe et al. (2002) (Eq 1.4) to calculate EEI for χ=-79° at each of the measured values (Appendix A, A.4, Figure 32); these values are printed on the graph in Figure 10c, with the corresponding change in pressure. These pairs of values (ΔPressure, ΔEEI at χ=-79°) are plotted against each other in Figure 11, using the black vertical-axis scale.

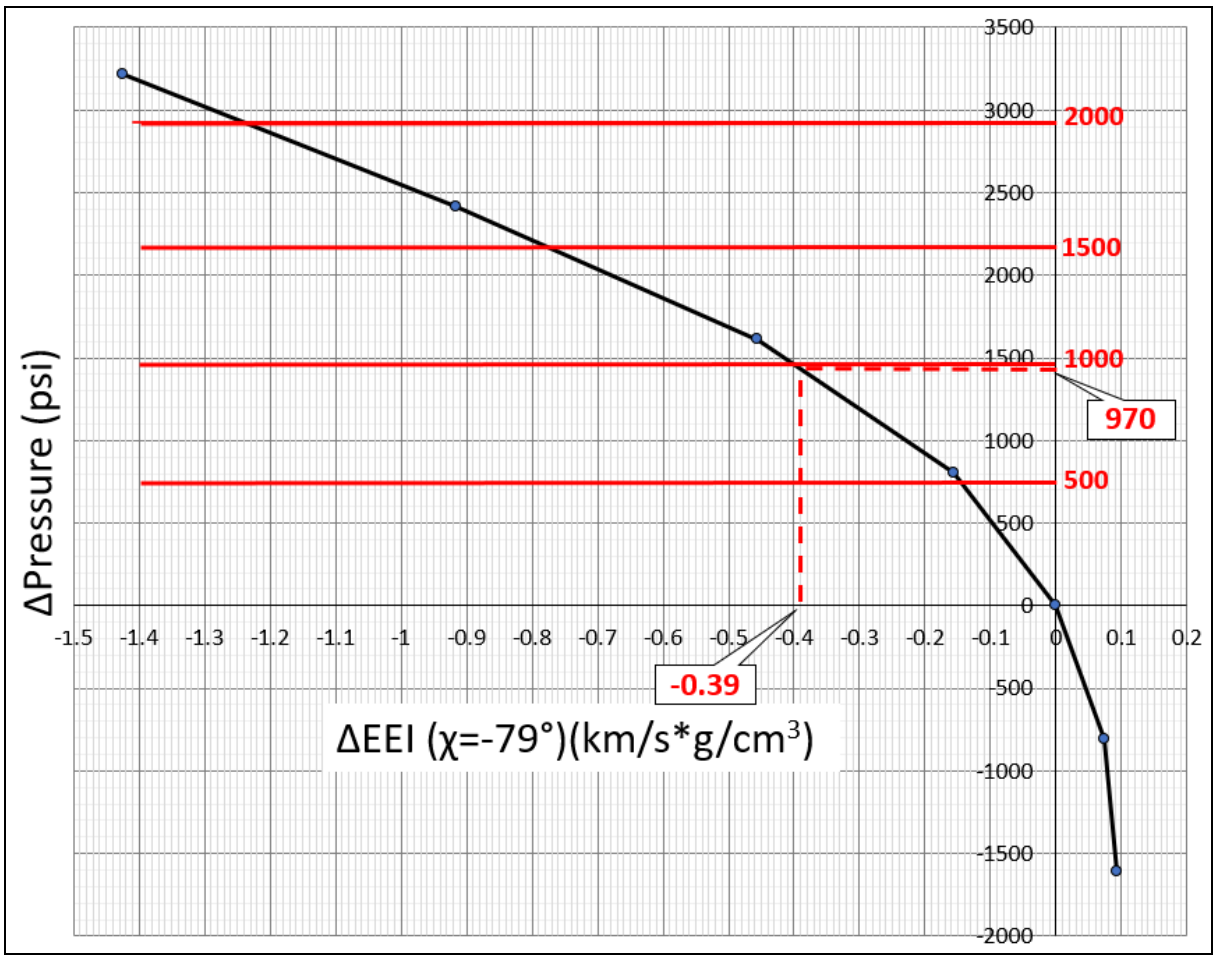

Figure 11. Macedon sand reservoir (pore) pressure change ΔP (psi) between BaseP and M1P surveys vs ΔEEI(χ=-79°) calculated from Wulff et al. (2008) rock-physics model relative to in-situ reservoir pressure. Red values on the vertical scale are "scaled" pressure to polygon C of 970 psi and to ΔEEI

=-0.39 (vertical dashed red line) as the average value within the polygon C. The scaled graph is presented in Appendix A, A.5, Figure 33.

There is only one (non-thin-bed) place in the reservoir where we have confidence in a known pressure change without fluid-saturation change, and that is the location of Polygon C. The average ΔEEI in Polygon C is -0.39; reading from the graph in Figure 11, we see that a pressure change of just under 1500psi is predicted there from the time-lapse seismic data using our ΔEEI approach. The operator has published (Appendix A, A.5, Figure 43) a map showing anticipated reservoir pressure changes across the field at the approximate time of the M1P survey, based on history-matching at wells and reservoir modelling; the predicted change read from that map is 970psi. On the other hand, Saul and Lumley (2015) cite a pressure increase in this area of 10MPa (1450psi); Ali et. al (2008) imply a pressure change of about 1500psi at that location; and Smith et al. (2010) used a pressure change of 1700 psi for their modelling. All of those authors had access to information that is not available to us, and it is quite possible that my prediction of ΔPressure ~1500psi in Polygon C, based on ΔEEI, is reasonably accurate.

5.3.2 Pressure Change if Additional Calibration is Needed

For the sake of demonstration, however, let us assume that the map provided in a report from the operator is correct, and the pressure change in Polygon C is 970 psi; this implies that we need to further calibrate our (ΔPressure, ΔEEI) relationship. The calibration of the inversion results for the difference volume ΔEEI at χ=-79° to the change in reservoir pressure from the well data was done in two steps. Firstly, I scaled Δ Pressure of ΔEEI(χ=-79°) model (Figure 11) to ΔEEI(χ=-79°) inverted map units (Figure 18j) for polygon C (where fluid changes are not expected) with the "known" change in pressure (+970 psi) (Figure 11). The (Appendix A, A.4, Figure 27) pressure change of +970 psi was calculated using initial reservoir pressure from the wells and modelled pressure by the operator at the time of the

Monitor survey (Smith, 2008) at the location close to polygon C. The results of this first step, the "scaled model" for pressure change, are shown in Figure 33 (Appendix A, A.4).

Secondly, I calculated the ΔP (psi) map from ΔEEI(χ=-79°) by applying that scaled model (Appendix A, A.4, Figure 33) to the ΔP (psi) map (Figure 19). The conversion was applied only to the maximum limits (negative and positive) of the pressure model. The values outside of the model were assigned as "null". More details and discussions on ΔEEI(χ=-79°) conversion to ΔP (psi) are in Chapter 6.2.

5.3.3 Saturation Change Prediction

In order to relate the change in saturation to our seismic difference observations, I made some simple assumptions, applicable to either the reflectivity or inverted volumes. Because these assumptions, were required due to our limited knowledge of the formation properties, I named it "pseudo-saturation" change, or ΔS_{WM}, equivalent to the change in saturation of mobile oil. First, we assumed that the area immediately surrounding well ENB02 underwent a change from irreducible water saturation (probably around Sw=20%) to residual oil saturation (probably around Sw=80%) and consider that to be 100% of the possible change in fluids from movable oil to water. I assigned the value observed at this location in the change in reflectivity and in the change in EEI to be ΔS_{WM} =1 or 100% (of movable oil, fully swept) and note that a difference value of ΔS_{WM} =0 corresponds to no fluid change (unswept). The Biot-Gassmann curves are roughly linear for the substitution of water for oil (both liquids) over this saturation change. Landro M. (1999) also used linear approximation between saturation and seismic parameters as Vp in his saturation and pressure changes calculations. So, I assumed a linear relationship between seismic reflectivity or EEI changes and saturation (Figure 20 and Figure 12); note that the entire range of ΔS_{WM} values from 0 to 1 likely covers only a fractional change in Sw from 0.2 to 0.8, but in fact covers the entire range of movable oil. However, we must realize that because the EEI angle of +42° is not exactly orthogonal to

the angle of maximum sensitivity to pressure changes (-79°), there is some non-zero effect due to pressure changes at this angle.

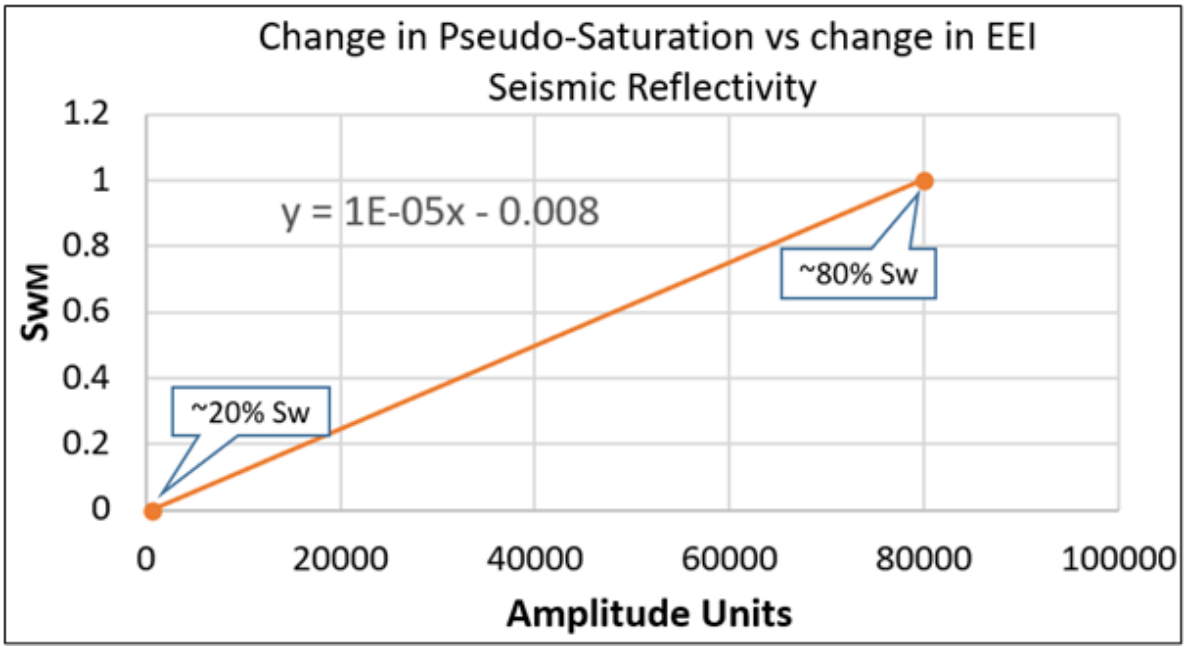

Figure 12. Graph used to calculate the changes in ΔSwM (movable-oil saturation change) from ΔEEI units, calibrated at the two end points as described in the text.

Chapter 6

6. Results and analysis

6.1 Qualitative results using polygon averages

6.1.1 Pressure and saturation change analysis from crossplots

The average values of time-lapse seismic amplitude differences (M1P – Base1P) for polygons A, B, and C are displayed as the crossplot of ΔRo (Intercept Amplitude Difference) vs ΔG (Gradient Difference) in Figure 13, and the projections of all three polygons on any angle from -90° to +90° is shown in Figure 14. The polygons were chosen for specific conditions as explained in section 4.4.1: A (where only small changes in fluid pressure or saturation are expected); B (where significant changes in both saturation and pressure are expected); and C (where 100% water saturation is expected to remain constant while the fluid pressure increases significantly).

We specifically examine rotation angles predicted to be most sensitive for changes in the fluid saturation (χ=+42°) and for changes in fluid pressure (χ=−79°). Rotated projections on the crossplot for χ=+42° and χ=−79° are shown as the best discriminants for fluid saturation and pressure, respectively, with projected polygon values on rotated projections. We look at the predicted changes in fluid and pressure for the three selected polygons, using Figure 13.

First, we qualitatively examine average values for fluid saturation changes. The black dot on Figure 13, representing polygon C, projects onto the χ=+42° rotated axis (the pink dashed line) at nearly zero amplitude change, corresponding to nearly zero change in saturation; no change in saturation was anticipated at polygon C. The blue dot, for polygon A, also projects onto the χ=+42° axis at close to zero amplitude, corresponding to nearly zero change in saturation within polygon A; this polygon is located in the oil leg away from the injectors, where we do not expect any significant change in saturation at the time of the monitor survey.

The red dot, representing polygon B, displays a large positive value when projected onto the χ=+42° axis suggesting a large increase in water saturation; this polygon is located in the oil leg and close to the OWC and the water injector ENB01, where we expect a significant increase in water saturation during initial production. All three amplitude values for polygons fit well, qualitatively, with our expectations for saturation change based on reflectivity (ΔRo, ΔG).

Next, we qualitatively examine pressure changes. Based on proximity to injection and production wells (and the operator's predictions from reservoir simulation), we expect to observe the largest increase in polygon B, closest to the injector ENB01 (Figure 16), a smaller increase in polygon C and the smallest increase for polygon A (furthest from the injectors). Projecting the points for the three polygons onto the χ=-79° (green dashed line) axis shows that polygon B has the largest average amplitude value, polygon A the smallest, and polygon C lies in between; all are as expected. All three polygons indicate a reservoir pressure increase, as expected based on the operator's reports and simulation (more liquid was injected than produced). The plot demonstrates a good correlation with data available from operator reports and anticipations of general reservoir behaviour during production for the polygons A, B and C.

The results of the scanning method as the time-lapse seismic amplitudes differences as the average values for polygons A, B, and C are presented in Figure 14. First, we examine average values for fluid saturation changes. We expected maximum difference amplitudes (positive values) for polygon B (with maximum saturation change) to be close to the angle χ=+42° we found for saturation change only from the fluid-substitution method. However, there is no extremum on the graph for polygon B related to positive values as we expected. But we see that the angle χ=+41° on the graph is the only angle where the saturation change for polygon C (here, we do not expect saturation change) is 0. The change in saturation is

also close to 0 for polygon A, and there is large positive difference for polygon B. The result is nearly identical to the optimal angle χ=+42° for saturation change from the fluid substitution method. Interestingly, the graph for polygon B does not show a maximum, but increases towards +90° together with graphs for C and A polygons. The correct answer to optimal angle for saturation changes is in combination and using three polygon values that fit the conditions change for three polygons, which in our case is +41°. For the pressure case, the statistical graph shows the maximum amplitude values for polygon B is at χ=-79°, for polygon C is at χ=-55° and for A is at χ=-50°. According to our prediction, maximum pressure without the effect of saturation should be observed at polygon C with a maximum value that is at the angle χ=-55° on the graph. Although this angle does not coincide with our calculated angle for pressure change from the rock-physics model (χ=-79°), -55° is nearly orthogonal to +42° and close to the shear modulus angle -60°. It is not clear why it does not coincide with the angle for pressure change from the rock-physics model. It is possible that the data deviate from our rock-physics model.

6.1.2 Pressure and saturation change analysis from inversion results

Polygon-wide averages were also computed for the ΔEEI inversion results. These were computed from inversions that were conducted on the BaseP and M1P volumes separately, and then differenced over the interval Top-Bottom Macedon. The resulting difference values were averaged over each respective polygon. The results are less consistent with expectations than the (ΔRo, ΔG) crossplot shown in Figure 13, probably due to the many assumptions required for inversion of data of limited bandwidth; for example, polygon C, below the OWC, shows a response suggestive of decreased water saturation (average negative values) for the χ=+42° on the inversion results (Figure 17b), which is unreasonable.

The polygon-wide average results for both the time-lapse reflectivity differences (ΔRo, ΔG) and the inverted ΔEEI are summarized in bar graphs (Figure 17) for the optimal χ

angles for fluid changes and pressure changes as well as χ angles for Δμ, ΔK and Δλ, for comparison with other rotations commonly used for exploration purposes.

6.1.3 Qualitative results

Here I present some comparisons of reflectivity maps with inversion maps. Figure 15 shows the seismic reflectivity time-lapse difference M1P-BaseP map for fluid change optimal angle χ=+42° for A, B and C polygons. The strong positive (hard) amplitude change observed for polygon B is related to the replacement of oil by water above OWC (green line). The seismic reflectivity cross-section I-II for fluid change optimal angle χ=+42° is shown on the map through the polygons A, B and C as displayed on Appendix A, A.4, Figure 34 for Base and Monitor surveys. The "hardening" or strong increase of the amplitude from the Top Macedon sand interface is highlighted by the ellipses for polygon B but not for A and C. The average seismic reflectivity values for the polygons A, B and C are presented in Figure 17a. The window of Top Macedon Sand -5ms and Top Macedon Sand +5ms phantom horizons was used for the amplitude extraction window by applying a simple average function to compile the map difference between two horizons for M1P and BaseP (Figure 34 and Figure 18e).

The same cross-section I-II with inversion results is shown in Appendix A, A.4, Figure 35. The window of Top Macedon Sand and Base Macedon Sand horizons was used for the amplitude extraction window by applying the absolute minimum amplitude function to compute the map difference for inversion (Figure 18f). The noticeable increase in the impedance highlighted by the ellipse indicates the substitution of the oil by water only within polygon B for the cross-section and map. The average inversion values for the polygons A, B and C are presented in Figure 17b.

Figure 16 shows seismic reflectivity time-lapse difference M1P-BaseP for pressure-only change optimal angle χ=-79° for A, B and C polygons with average values in Figure 17a. The

strongest negative (softening) amplitude change is observed for polygon B, the closest to ENB01 injector well related to the pressure increase. C polygon has a strong negative smaller amplitude also close but further from the ENB01 and the still smaller increase in polygon A. The seismic reflectivity cross-section I-II for pressure-change optimal angle χ=-79° shown on the map through the polygons A, B and C is presented in Figure 36 for Base and Monitor surveys. The "softening" or strong reduction of the amplitude from the Top Macedon sand interface in B and C polygons is highlighted by the ellipses. The inversion results are shown in Figure 37. The strong negative (softening) amplitude changes are related to the pressure increase. The low impedance amplitude anomalies within Macedon sand for Base and Monitor surveys are interpreted as good quality (high porosity) sands.

Saul and Lumley (2015) also observed an increase in the pressure close to ENB01 in the area of their investigation coinciding with polygon C on Figure 38. They used the same seismic surveys (with more advanced processing, not available to this study) and calculated a 50% increase in the amplitude using mid stacks for the Monitor survey and explained it as mechanical weakening of the reservoir rock because of high-pressure water injection.

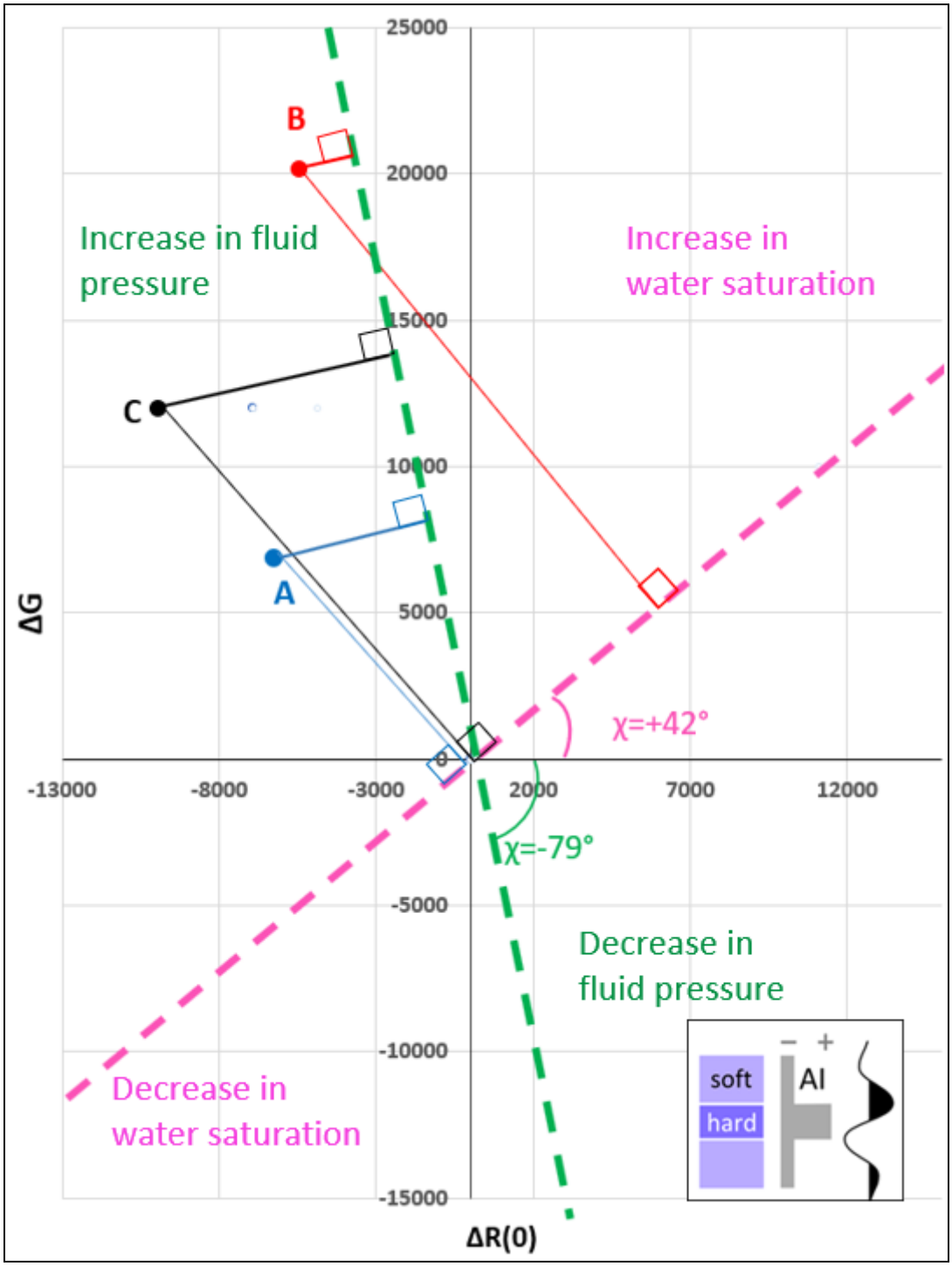

Figure 13. Time-lapse seismic amplitudes differences (M1P – BaseP) for average values in polygons A (blue), B (red), and C (black) are shown as a (ΔRo, ΔG) crossplot. Rotated projections for fluid-saturation changes at χ=+42° and for fluid-pressure changes at χ=-79° are displayed as thick pink and green dashed lines respectively. Thin solid lines show the paths of projection from each polygon's point to each rotated axis

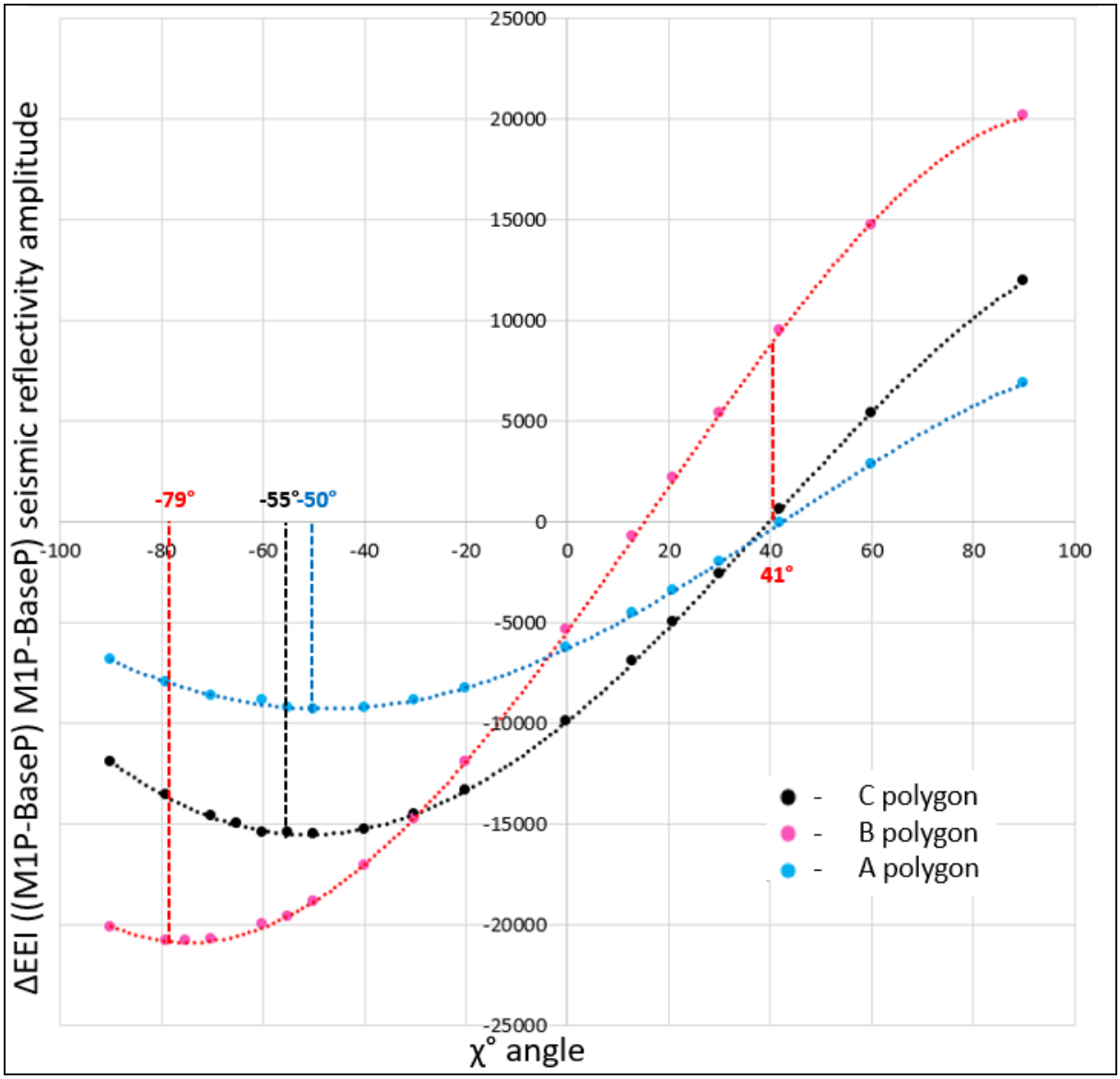

Figure 14. Intercept/Gradient AVA seismic amplitude (as average values) difference (M1P-Base1P) for Top Macedonian vs χ angles from -90° to +90° for A, B and C polygons.

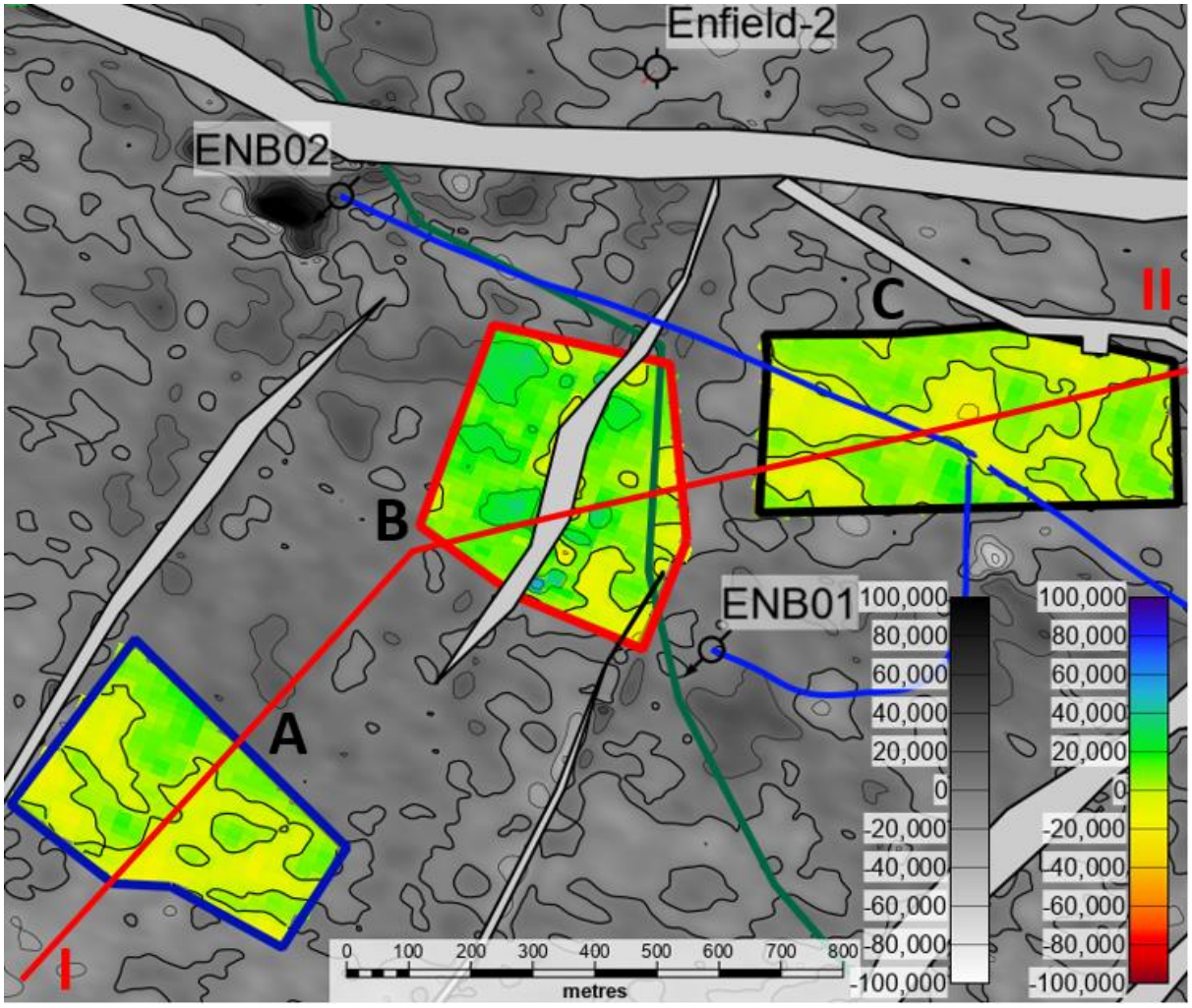

Figure 15. Seismic reflectivity time-lapse difference M1P-Base1P for fluid change optimal angle χ=+42° for A, B and C polygons. Contour interval is 20,000. The highlighted solid contour is 0 value. Note, the strong positive (hard) amplitude anomalies prevail for polygon B related to replaced oil by water above OWC (thick green line).

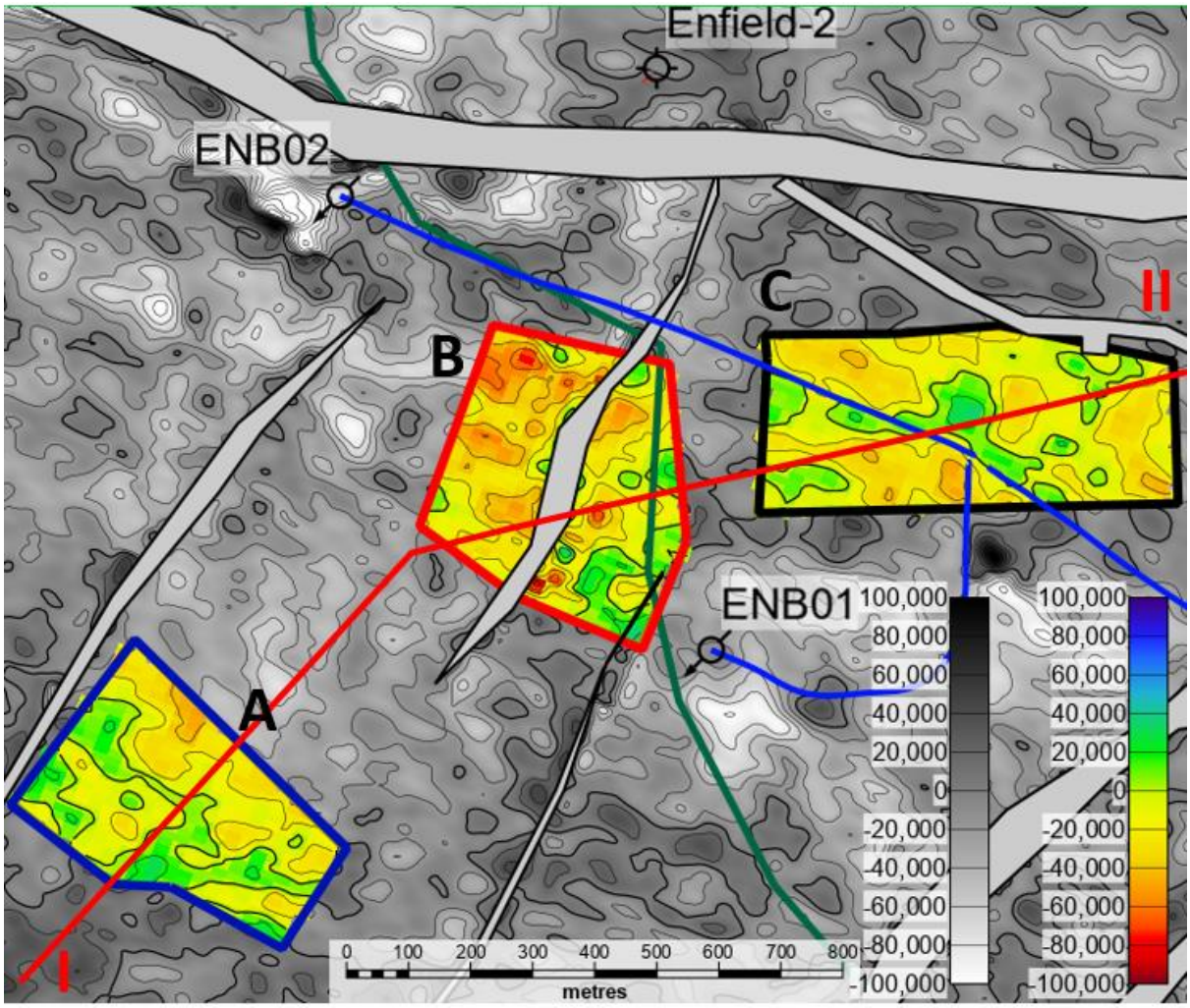

Figure 16. Seismic reflectivity time-lapse difference M1P-Base1P for pressure change optimal angle χ=-79° for A, B and C polygons. Contour interval is 20,000. The highlighted solid contour is 0 value. Note, the strong negative (soft) amplitude anomalies prevail for polygons B and C related to pressure increase close to injector well ENB01. Thick green line is the OWC.

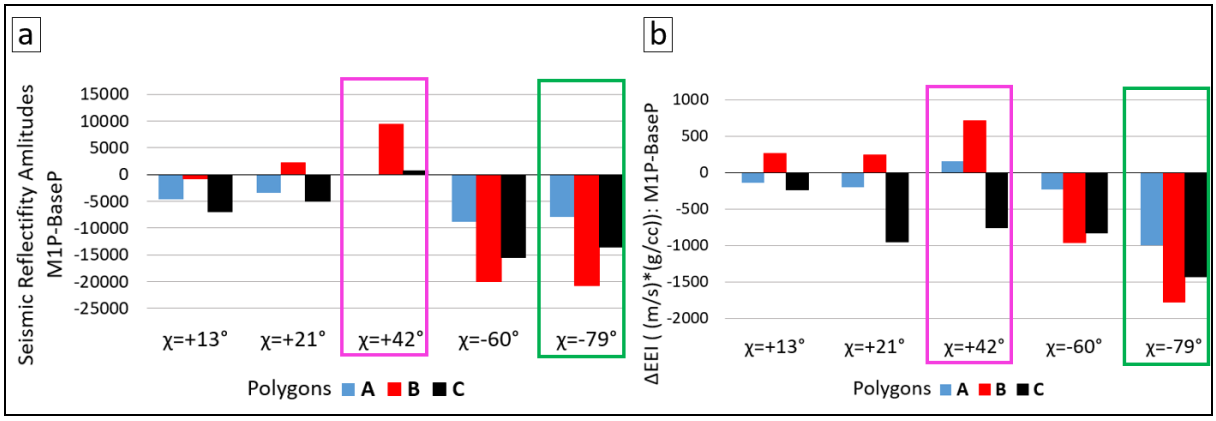

Figure 17. Time-lapse seismic reflectivity (a) and inversion amplitude differences (b) as an average values vs χ angles for polygons A, B, C. Optimal angles χ=+13°, χ=+21° and χ=−60° relate to ΔK, Δλ and Δμ respectively. The most sensitive angles for saturation and pressure changes are χ=+42° and χ=−79° respectively, emphasized by the pink and green boxes.

6.1.4 Conclusions on qualitative analysis

The conclusions can be summarised based on the qualitative results:

- The relative values from seismic reflectivity for each polygon are consistent with expectations, given a qualitative interpretation of reservoir production.
- The inversion results are mostly consistent with expectations, except for polygon C at χ=+42° (saturation change), which suggests an unreasonable time-lapse response. The many assumptions required for the inversion of older, narrow-band, seismic data are likely responsible.
- The shear modulus (Δμ, at χ=−60°) provides results similar to that for pressure (χ=−79°), as one might anticipate, particularly for reflectivity.
- The rotation angles often found to be useful for exploration and development (ΔK, at χ=+13°; Δλ, at χ=+21°) appear to be much less useful for time-lapse monitoring of fluid-saturation and fluid-pressure changes.
- The results from the scan method confirm the results for Gassmann fluid substitution method for the saturation change only in polygons A, B and C. The maximum

amplitude difference for a pressure change in the polygon C is χ=−55°, which is close to shear modulus angle χ=−60° and not χ=−79° as was anticipated. The encouraging fact is that the χ=−55° is nearly orthogonal to χ=+42° (saturation change only) from our Gassmann substitution method.

The results are also presented as difference maps for the time-lapse reflectivity and inversion rotations, first for qualitative comparisons (Figure 18) and then for quantitative pressure (Psi) (Figure 19) and pseudo-saturation (Swm) changes (Figure 20). Although our quantitative analysis will be restricted to the thick-bed areas in polygons A, B, and C, there are other areas of the field where some interesting features exist, and they will also be discussed in a qualitative manner.

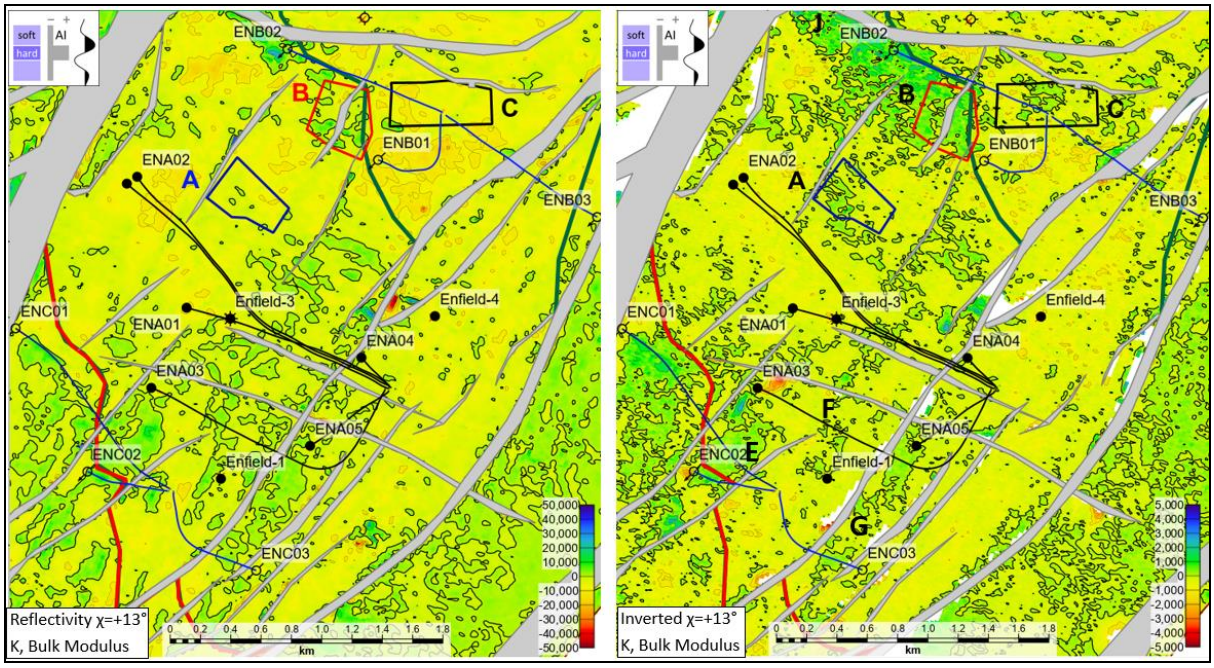

a) b)

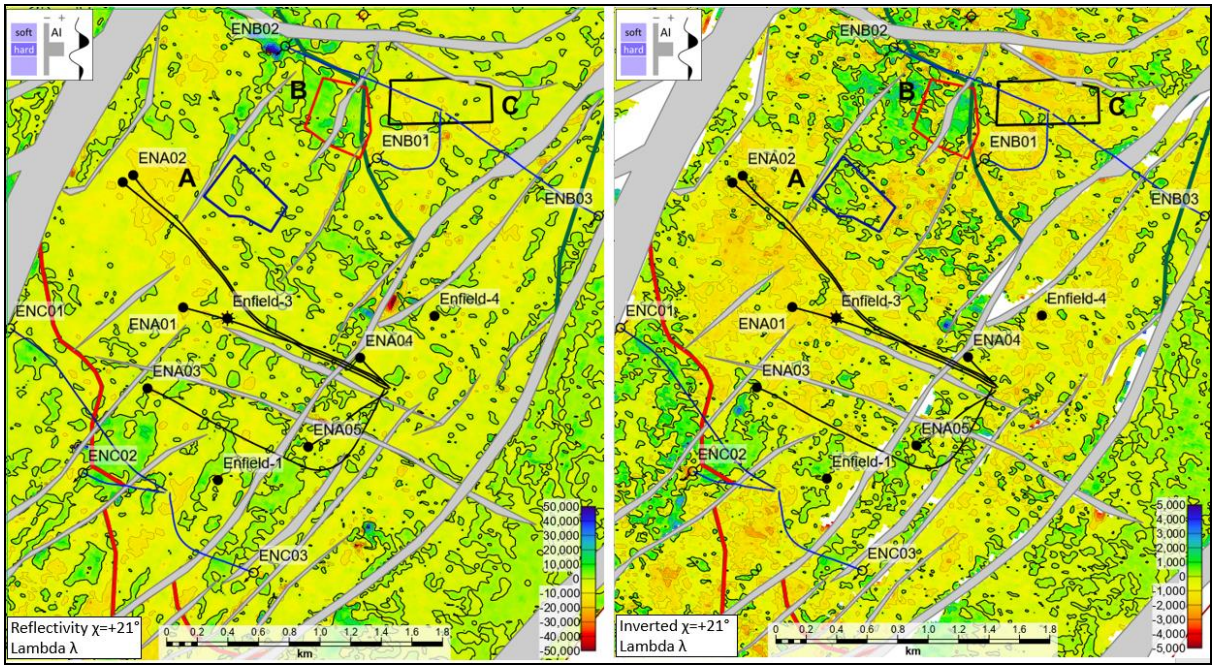
soft
hard
AI
ENB02
B
C
ENB01
ENA02
A
ENB03
ENC01
Enfield-3
Enfield-4
ENA01
ENA04
ENA03
ENA05
ENC02
Enfield-1
ENC03
Reflectivity χ=+21°
Lambda λ
Inverted χ=+21°
Lambda λ
km

c) d)

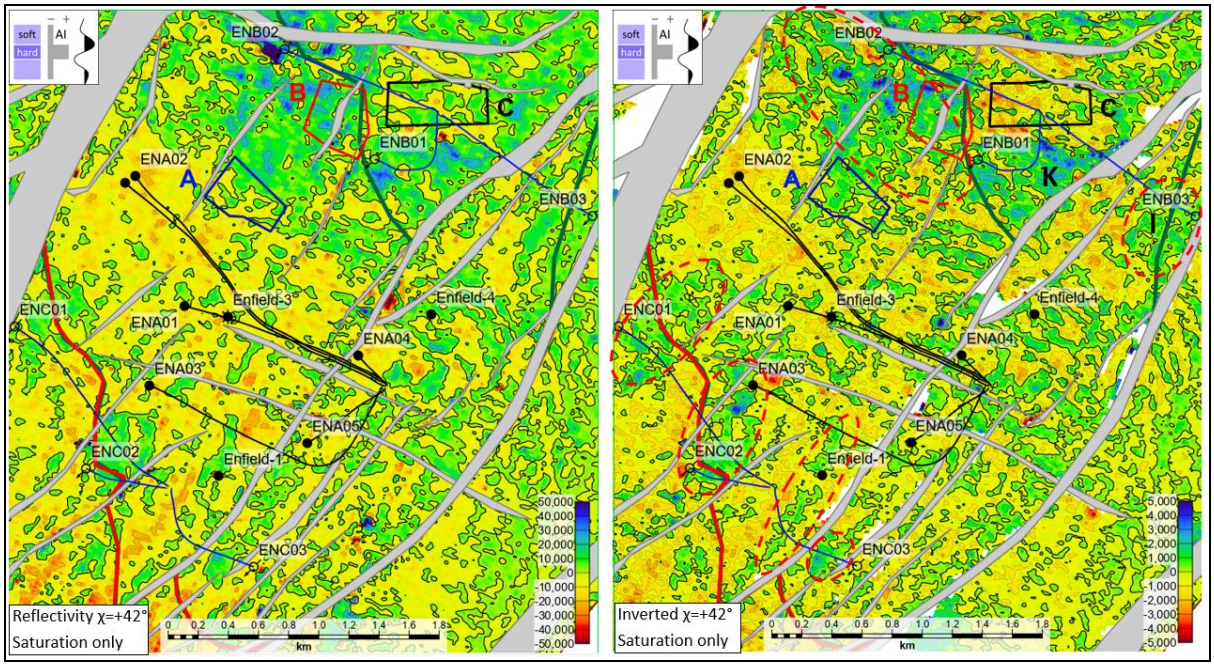
soft
hard
AI
ENB02
B
C
ENB01
ENA02
A
K
ENB03
ENC01
Enfield-3
Enfield-4
ENA01
ENA04
ENA03
ENA05
ENC02
Enfield-1
ENC03
Reflectivity χ=+42°
Saturation only
Inverted χ=+42°
Saturation only
km

e) f)

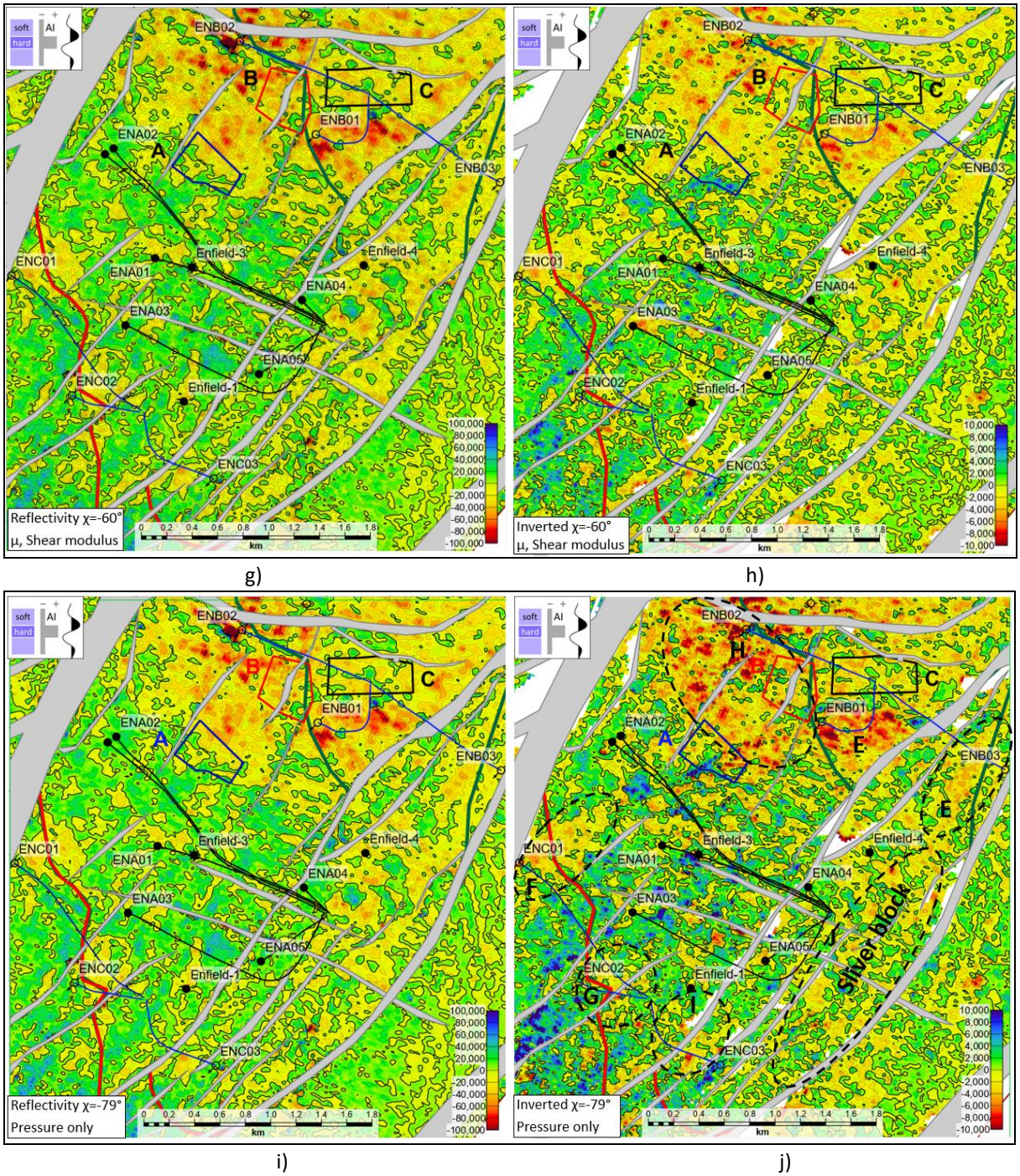

Figure 18. Reflectivity (on left) and inverted (on right) time-lapse difference maps for EEI angle χ=+13^o (a, b), χ=+21^o (c, d) χ=+42^o (e, f), χ=-60^o (g, h) and χ=-79^o (i, j). Black contour is 0. Black ellipses and letters F, G, I, H, E on (j) highlight the anomalous pressure increase. Red ellipses on (f) highlight the water saturation increase anomalies.

Several key points have been observed from the maps:

- The seismic reflectivity and inversion maps are very similar for each angle pair.

- The inversion maps are noisier than reflectivity for each pair and all angles.
- Reflectivity and inversion maps for small angles (χ=+13° and χ=+21°) are less noisy than for larger angles which is consistent with NRMS analyses.
- The maps for discriminant angles χ=-79^o as pressure only (Figure 18i and Figure 18j) and χ=-60^o for $\Delta\mu$ moduli change (Figure 18g and Figure 18h) are nearly identical.
- Maps for angle χ=-79^o as pressure only (Figure 18i and Figure 18j), show a good correlation of negative anomalies around all injector wells due to the pressure increase.
- Maps for angle χ=+42^o (Figure 18e and Figure 18f), show a good correlation of positive anomalies around all injector wells as the S_{WM} increases except at the east of ENB01 (marked as K), where was not expected water saturation change below OWC.
- Maps for χ=+13^o and χ=+21^o do not show distinctive saturation changes around the injectors, suggesting that these angles are not useful for most time-lapse studies.

6.2 Test of pressure prediction using scaled calibration

My final quantitative interpretation is based on the pressure change calculated from ΔEEI data (Figure 19). I do not have ground-truth for fluid-saturation changes in the reservoir (other than zero change below the OWC), but I do have independent estimates of pressure changes. As described earlier, the operator published a map suggesting that the pressure change in polygon C would have been +970psi, but other authors have suggested pressure changes of 1450psi to 1700psi. If the latter figures are correct, my quantitative estimate is accurate. But, if the +970psi figure is correct, we have to consider possible sources of error. This section assumes that the operator map is correct, and I apply my “scaled” calibration for pressure changes. I also compare our prediction in another polygon with that predicted based on the same map by the operator that yielded the +970psi figure for polygon C, but in an area that may have significant thin-bed effects.

Given the complexity of this procedure and limitations due to data deficiency (discussed below), it was not expected the results would be very accurate. Therefore, the goal was to outline the procedure that could be very effective with the better quality and additional data.

1. Issues in ΔEEI maps.
    a. Random errors as the positive spikes strongly affect the ΔEEI maps rotated to χ=-79°, which were used for pressure calculation (Figure 18i and 18j). This problem relates mainly to large-rotated-angle volumes, which amplify the noise as discussed in Chapter 4.3. Linear positive spikes are related to fault interpretational errors. The other dot-like spikes are probably caused by the auto-propagation tracing procedure of the complex Base Macedon sand horizon interpretation.
    b. Systematic errors at small to moderate positive ΔEEI anomalies which can be seen on a smoothed map (Appendix A, A5, Figure 42). These anomalies are mainly within the area of the producer wells and are generally smaller than strong positive anomalies related to the pressure increase.

       These values can be explained by decreasing pressure due to production within the area of the producer wells. The crude pressure data from the operator at the time of the Monitor survey show a decreased pressure around the producers (Appendix A, A.5, Figure 43). These data were derived from reservoir simulations to provide pressures across the field and can be used as general indications of pressures anticipated. We also do not know the accurate positions of the pressure references on this map to calculate pressure change accurately. Nevertheless, we can qualitatively assume the pressure drop around the producer wells and explain these negative ΔEEI anomalies. Another possible reason and explanation could be the sensitivity issue. The lower the pressure change – the less chance there is to determine these small changes from

seismic data. Then the logical question is: What is the accuracy of calculating the pressure change effect?

Other reasons can be cross-talk with the saturation effect and tuning effect of thin beds that have a vast area within the field (Appendix A, A.5, Figure 44).

This is an important issue but is beyond the scope of this thesis and would require further research.

2. Errors in the transform.
    a. Core damage in core samples used in building the rock-physics model. According to D. H. Johnson (2013), “Unfortunately, most predictions of velocity sensitivity to pressure have a high degree of uncertainty. In general, we tend to overpredict the velocity increases caused by pressure depletion and underpredict the velocity decreases caused by injection. There are several reasons for this. Core measurements are subject to sampling biases (e.g., the core samples might not include fractures that exist in the reservoir) and to damage (the samples might include induced fractures that are not in the reservoir)”.
    b. Representativeness (single curve for the entire reservoir). Our model is based on the data from one well for the entire field.
    c. Clay content variations in the reservoir due to turbiditic deposition while the model transform is based on a sand member.
    d. Inadequacy of the stress path of ultrasonic measurements (confining pressure in the stress cell vs vertical confining pressure in the reservoir). D. H. Johnson (2013) says, “Laboratory measurements are often made under hydrostatic conditions. However, the reservoir might not be under hydrostatic stress. Velocity change in the reservoir also depends on the stress path during depletion. The pressure dependence of velocity for variations in uniaxial stress is quite different from that for hydrostatic stress. To

complicate things further, changes in nonhydrostatic stress can induce anisotropy in initially isotropic rock. Even a change in hydrostatic stress can alter existing anisotropy. Needless to say, this is all an area of active research in industry and academia".

e. Asymmetry of the pressure response. Asymmetric velocity change resulting in decreasing pore pressure from depleting reservoir and increasing pore pressure from injection was studied by C. Sayers (2007), who concludes "Large changes in seismic reflection amplitude have been observed around injectors, and result from the decrease in elastic-wave velocity due to the increase in pore pressure in the reservoir. In contrast, the velocity change resulting from the decrease in pore pressure in depleting reservoirs is observed to be smaller in magnitude. Elastic-wave velocities in sandstones vary with stress due to the presence of stress-sensitive grain boundaries within the rock. Grain-boundary stiffness increases non-linearly with increasing compressive stress, due to increased contact between opposing faces of the boundary. This results in a change in velocity due to a decrease in pore pressure that is smaller than the change in velocity caused by an increase in pore pressure, in agreement with time-lapse seismic observations".

f. ΔEEI to ΔP calculation graph is extremely asymmetrical due to extreme non-linearity of the ΔEEI - ΔP transform based on ultrasonic measurements. The most problematic is the negative pressure change transform. This part of the graph can yield many areas of huge unrealistic decreases in pore pressure if we extend the graph trend as the logarithmic function. This is another caveat in this project that I do not cover in the thesis. I used the pressure calculation change values only inside of the model range, assigning the outside values as nulls.

As a result, our quantitative analysis will be restricted to a comparison of our pressure estimations in two polygons already introduced, B, and C, plus a new polygon, D, selected due to available pressure data from ENA03L1 well, which was drilled five months after monitor M1P survey. Figure 19 shows a map of our predictions for fluid-pressure change. The pressure values were calibrated by known pressure changes in polygon C, but polygons B and D had not been used in that calibration, and are considered "blind" tests of our predictions, summarized in Table 2. Note that polygon D has the thinnest reservoir layer of any polygon that was selected (Figure 44), and may exhibit thin-bed artefacts that will contaminate our data there.

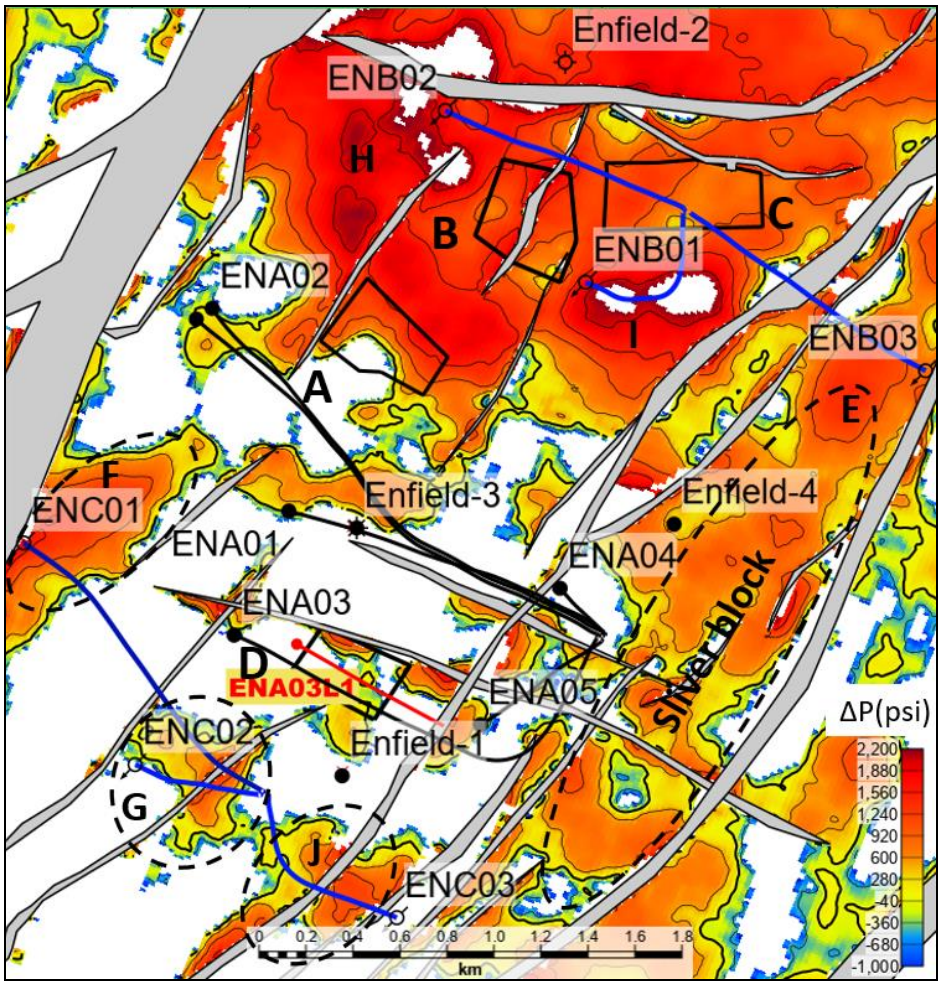

Figure 19. Reservoir fluid-pressure change ΔP (psi). Contour interval is ΔP=500 psi. Thick contour is 0. White colour are the null values.

Polygon	Polygon status	Depth (m)	ΔEEI (km/s)* (g/cm^2)	P discovery (psi)	P monitor (psi)	ΔP from operator (psi)	ΔP from ΔEEI (psi)	Discrepancy (psi)	Error %
B	"Blind" test	2130	-0.54	3142	<4200	> + 1058	+ 1224	+ 166	<16
C	Used for scaling	2190	-0.39	3230	4200	+ 970	+ 958	- 12	1
D	"Blind" test	2060	-0.05	3020	3200	+ 180	+ 63	- 117	65

Table 2. "ΔEEI (km/s)* (g/cm^2)" is the average values for each polygon from the ΔEEI for angle χ=-79° inversion map (Appendix A, A.5, Figure 42). Pressure data for polygon C was used to scale the ΔEEI inversion results for pressure map calculation. Polygons B and D are examined here for quality control. "P (discovery)" is the original pressure data at time of discovery from five wells calculated at the depth of the reservoir at the locations of the polygons B, C, D. "P (monitor)" is the pressure for B and C calculated by the operator (Smith, 2007). ENA03L1 well pressure data drilled in 2007 was used for the "blind" test of the calculated pressure change map (Figure 19).

The "ΔP from ΔEEI (psi)" in the table was calculated for each bin within polygons and then averaged. That is why a small discrepancy of 1% error exists for the polygon C. The small discrepancy of less than 16% for polygon B is a good result of pressure prediction. The discrepancy of 35% error for polygon D is larger but still satisfactory. Admittedly, the results for the polygon D are somewhat fortuitous. The polygon values were partially trimmed by null values. The polygon is also about 80% in the range of 10-12 ms, and therefore, in the marginally thin-bed area (Appendix A, A.5, Figure 44). In the absence of other pressure data, the polygon D was used as an example of the application of the technique, in spite of its certain contamination with thin-bed effects. Generally, the results are acceptable and demonstrate that our method works well.

The map shows that all water injectors including ENC01, ENC02, ENB02, ENB01 and ENB03 have anomalous pressure around the wells labelled F, G, H, I, J and E respectively

(Figure 19). It is worth drawing attention to pressure anomaly E over the Sliver block. The operator recognised (Smith, 2007) the pressure increase at this block and drilled a producer well up dip of ENB05 in 2008 to recover unswept the oil from this block (Hamson, 2012) (Appendix 5, A5, Figure 39).

It is worth highlighting that the intensity of the strongest pressure anomalies H, I and F (Figure 19) very well correlates to the magnitude of the collapsed areas around the water injector wells: ENB02, ENB01 and ENC01 respectively (Appendix A, A.2, Figure 21). This also indicates that the method works well.

The change of the pressure and saturation maps can also be compared with the operator's maps as the pressure and saturation effect (Appendix 5, A5, Figure 40). The operator used time-lapse inversion volume interpretations based on Acoustic Impedance and Poisson Ratio data to delineate areas undergone primarily Pressure, Gas and Water effects as the volume data. They reported the overwhelming pressure response in the Northern part of the field, where my study is concentrated, similar to the pressure change map from the ΔEEI (Figure 19). Some pressure anomalies on my map are stronger and more prominent than on the operator's map (Around injector wells ENC01, ENC02, ENC03 and ENB03). The operator detected only small areas of water saturation changes in this part of the oil leg. It may be concluded that my method is likely more reliable.

The movable-oil-saturation change ΔS_{WM} map generated from the reflectivity volumes also correlates well with the expected increase in saturation around water injection wells at K (well ENC01), L (well ENC02), M (well ENB02) and J (well ENB03) above OWC (Figure 20); a quantitative comparison is not possible due to the lack of ground-truth data. Anomaly L is worth emphasising as it likely caused water encroachment resulting in the shutting down of producer ENA03 and injector ENC02, consistent with the operator's interpretation (Smith

et al., 2008) (Appendix A, A-5, Figure 41). Thin beds (see Figure 6) in the vicinity of the ENB01 injector below OWC present artefacts that appear as an (unreasonable) increase in saturation within the water leg. The modelling of the thin-bed effect confirms this suggestion (Appendix B, B 2.4).

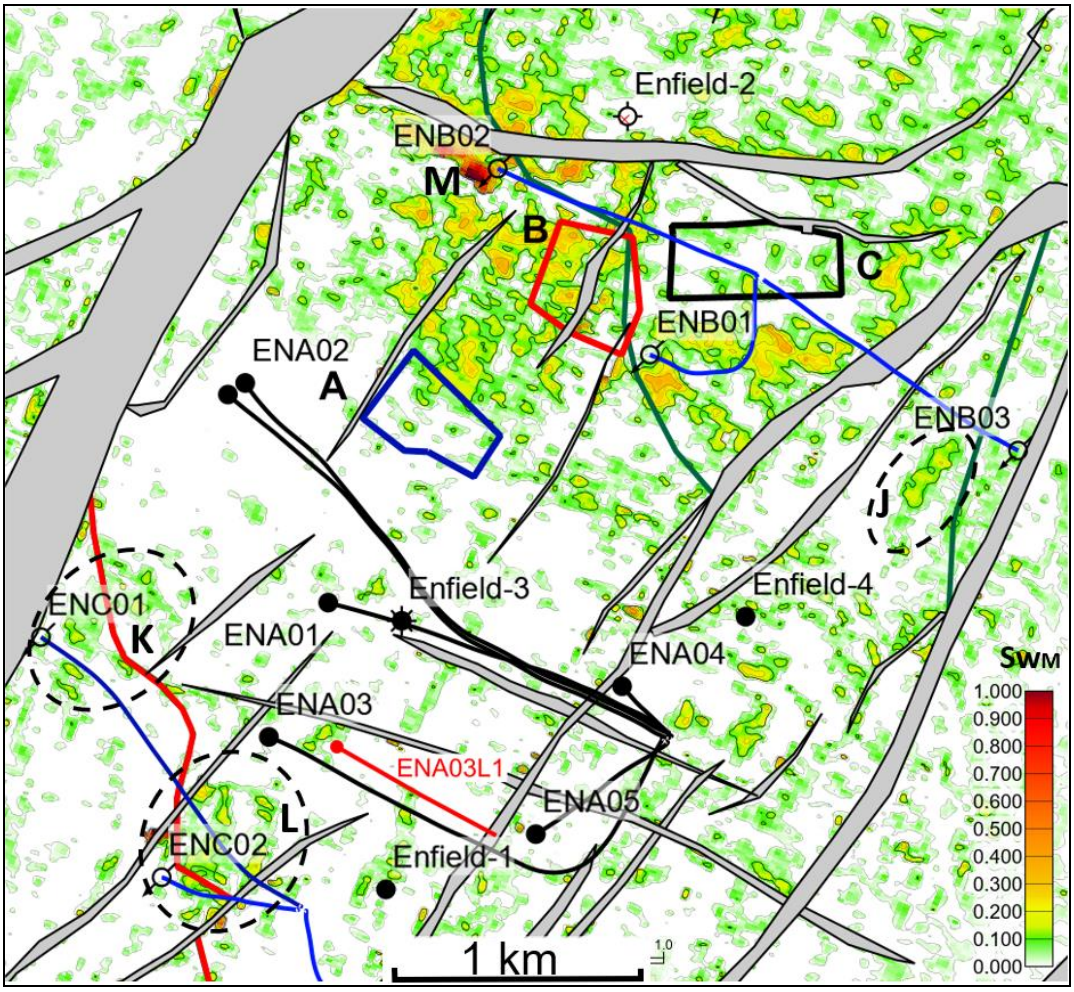

Figure 20. Movable-oil-saturation change ΔSwM. Solid highlighted contour ΔSwM =0.1.

Chapter 7

7. Conclusions and recommendations

I consider Biot-Gassman fluid substitution as the reliable method to model changes in elastic properties from log data and find the EEI angle χ=+42° that is optimal for water saturation changes. The scan method shows the EEI angle χ=+41° as the only one that fits the conditions as the saturation change for all three polygons and therefore confirms results for the fluid-substitution method.

I used the Enfield rock physics model based on fitting laboratory velocity-pressure data to determine EEI most sensitive angle to pressure changes. Calculated optimal angle χ=-79° for pressure change only is not exactly orthogonal to angle χ=+42° as saturation changes only as we would like to have. EEI most sensitive angle to pressure changes from the scan method χ=-55° is close to shear modulus χ=-60° obtained from the logs and nearly orthogonal to EEI angle optimal for water saturation.

The seismic reflectivity rotated volumes are recommended as robust and straightforward in processing for qualitative interpretation. The inversion domain is needed for quantitative results to calculate the pressure from EEI log data. It is important to have good quality data (seismic and well logs, ideally having the logs for Monitor survey) to have reliable results.

I have demonstrated that the EEI concept applied to time-lapse seismic data can be used to monitor reservoir pressure and saturation changes during production. The method successfully predicted the areas where changes in pressure and/or saturation were expected and did a good job of separating the two properties. My final calculated pressure maps were successfully tested with areas of changing pressure that had not been used in the calibration, showing that my quantitative results are credible. Additionally, the anomalies of pressure and

saturation change coincide with the results from the operator and other researchers who used different methods to map pressure and saturation changes for the field.

The ease with which rotated seismic volumes, to any arbitrary χ angle, can be created in modern workstation software, could make the reflectivity (ΔRo, ΔG) method a useful and quick technique to include in the time-lapse interpreter's toolbox. Although my results from inversion were less convincing in some aspects, the availability of better quality seismic data, with proper calibration of inversion units to field units, can allow application of results in a quantitative manner.

A proper analysis of NRMS for various acquisition angle ranges and for rotation χ angles should inform the interpreter of which results should be treated with caution.

I suggest several methods to find optimal χ angles for reservoir pressure and saturation changes. In the absence of good rock-physics studies, one could use the optimal angle for shear modulus to detect pressure changes, and an orthogonal angle to this in order to detect saturation changes; neither angle would be that which is most sensitive to each property, but they are uniquely uncontaminated by the other property. When one has the opportunity to conduct more-detailed analysis, the optimal angles for each property could be determined, and studied; the closer they are to orthogonal, the better.

These techniques may prove helpful for quick-turnaround studies and for obtaining a sense of confidence in any more-detailed analyses. The results I obtained in the case study were based on mediocre-quality data that happened to be available online years after the field surveys were conducted, and did not include higher-quality processing or later surveys that had been made available in the past, but that are no longer accessible to researchers.

I recommend manually interpreting the horizons and scrutinizing its results to avoid casual spikes that affect the difference maps.

Further research would be required to define the sensitivity and accuracy of the quantitative results in cases of low-pressure change.

Asymmetric function for negative and positive pressure and the limitation of the data range from the rock-physics model also require further studies.

Although my inversion results are less robust then seismic reflectivity, the quantitative results of the pressure change map confirmed that our method works well. I believe that modern processing techniques and high-quality data can provide better results using our methodology.

Our method is theoretically coherent and practically proved applicable despite some issues I have encountered. That confirms by the quantitative and qualitative results.

APPENDIX A

A.1

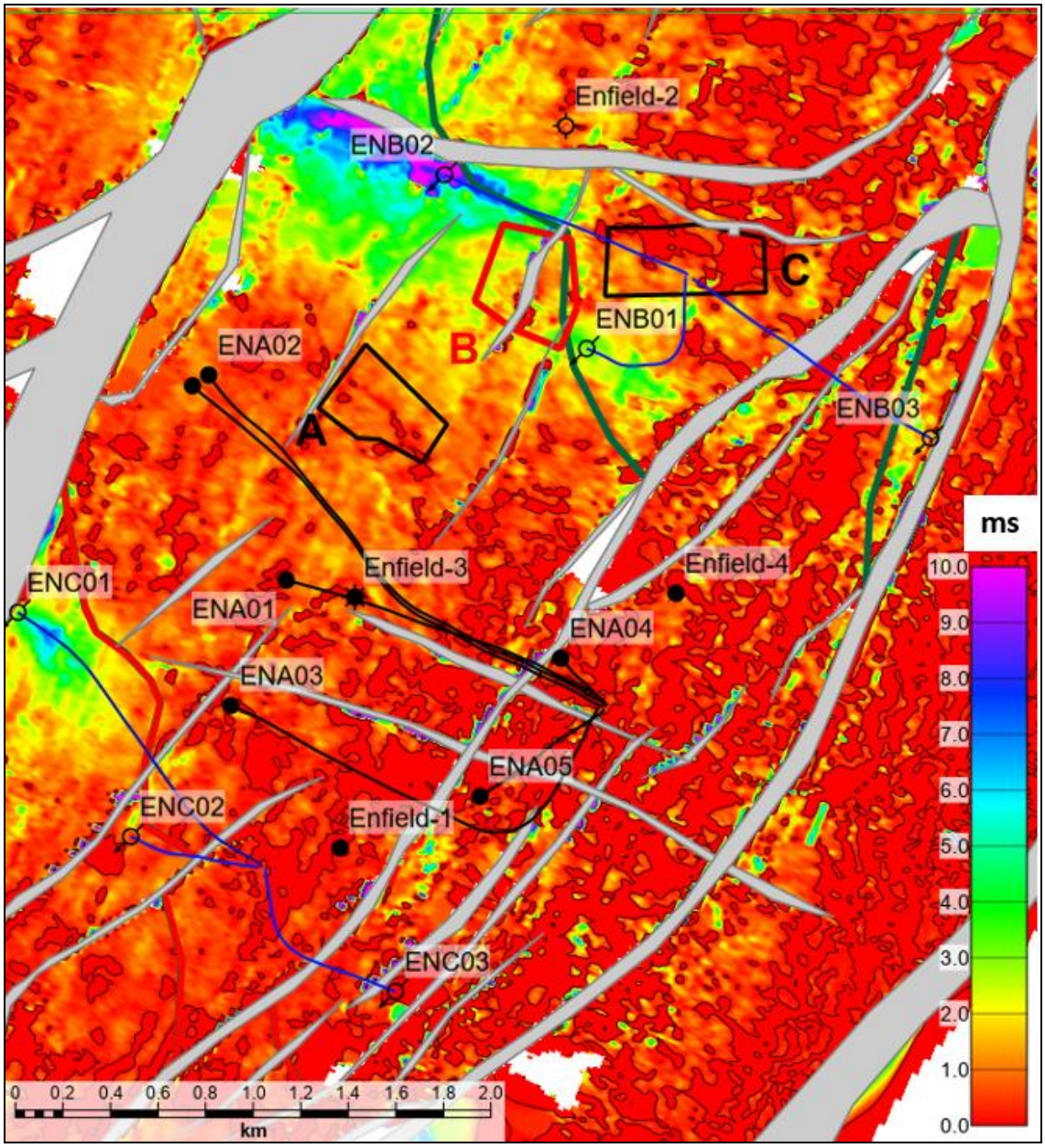

Figure 21. Top Macedon sand horizon difference M1P - BaseP1as two-way time map (ms) showing collapse of the top of the reservoir as positive values. Shown contour is 0. The strongest values around the water injector wells: ENB02, ENB01 and ENC01. Note that the largest collapsed areas correspond to the strongest pressure anomalies labelled H, I and F respectively on Figure 19.

A.2

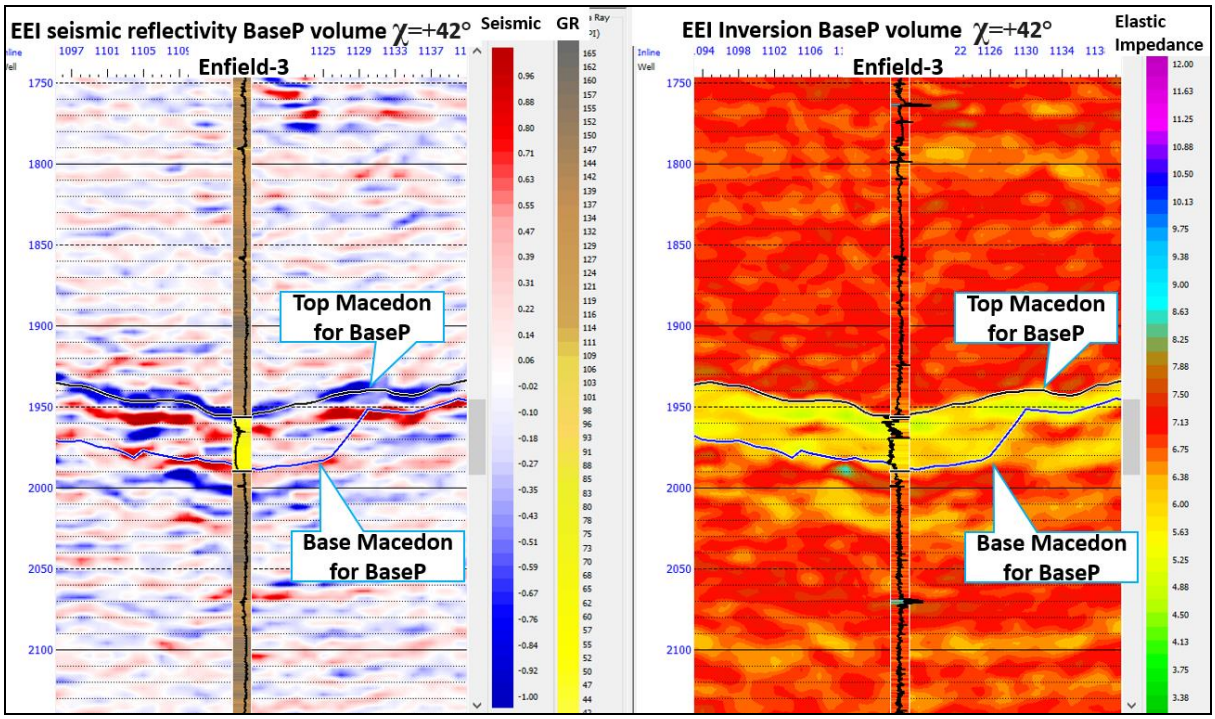

Figure 22. Left is the cross section of seismic reflectivity intercept/gradient BaseP volume rotated to χ=+42° angle. Section of crossline 2075 is going across the Enfield-3 well with gamma ray log showing the reservoir. Right cross section is Extended Elastic Impedance of inverted Extended Elastic Impedance for BaseP volume rotated to χ=+42° angle. Log is Elastic Impedance rotated to χ=+42° angle. Note, the good lithology and inversion results correlation for that rotation angle.

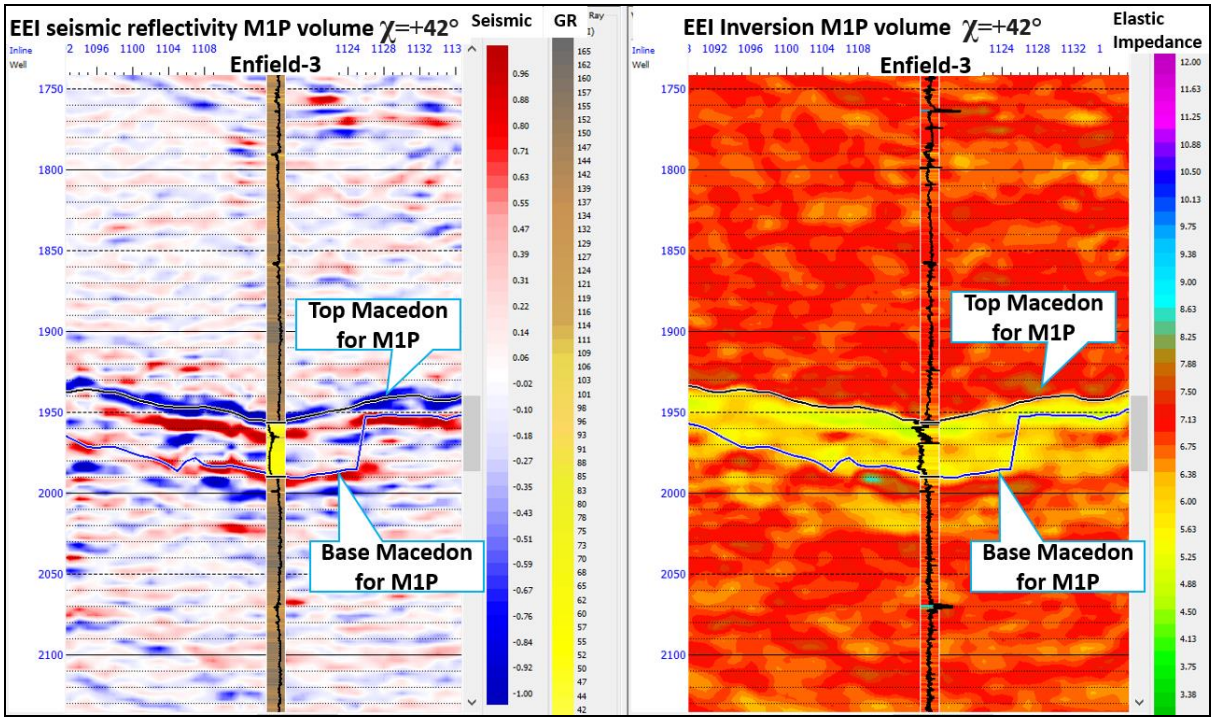

Figure 23. Left is the cross section of seismic reflectivity intercept/gradient M1P volume rotated to χ=+42° angle. Section of crossline 2075 is going across the Enfield-3 well with gamma ray log showing the reservoir. Right cross section is Extended Elastic Impedance of inverted Extended Elastic Impedance for M1P volume rotated to χ=+42° angle. Log is Elastic Impedance rotated to χ=+42° angle. Note, the good lithology and inversion results correlation for that rotation angle.

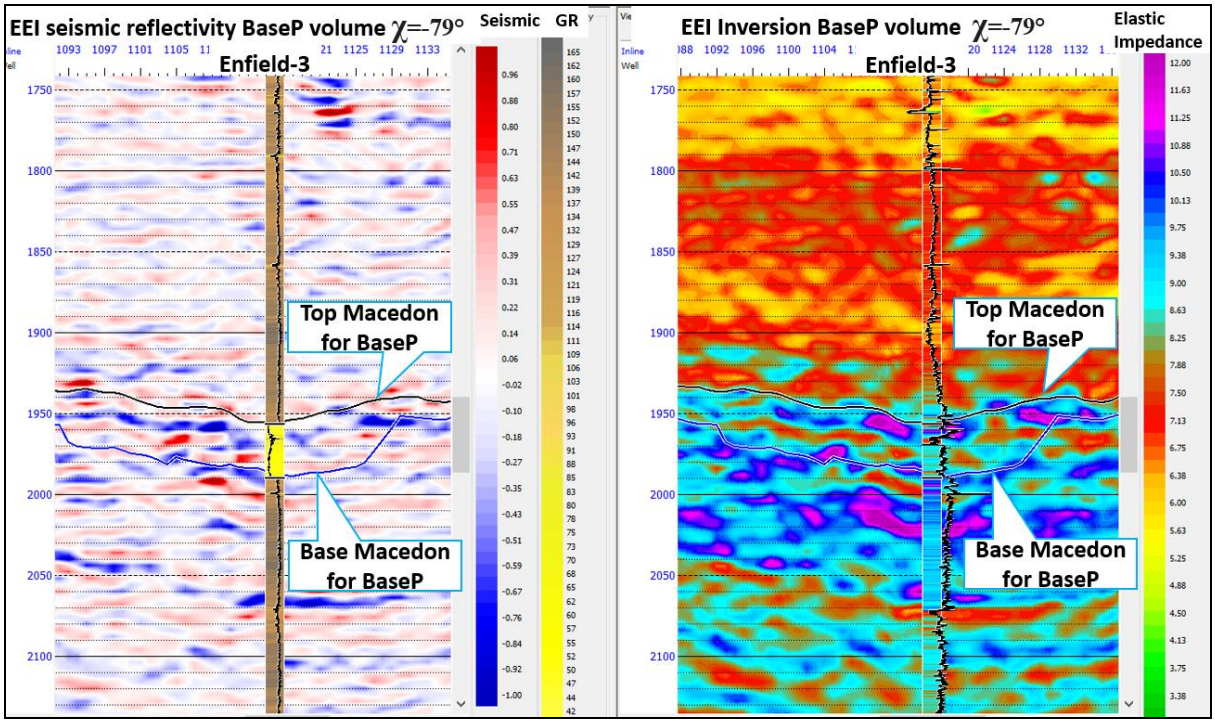

Figure 24. Left is the cross section of seismic reflectivity intercept/gradient BaseP volume rotated to χ=-79° angle. Section of crossline 2075 is going across the Enfield-3 well with gamma ray log showing the reservoir. Right cross section is Extended Elastic Impedance of inverted Extended Elastic Impedance for BaseP volume rotated to χ=-79° angle. Log is Elastic Impedance rotated to χ=-79° angle. Note the noisy character of the seismic and fair inversion results at this large angle of rotation.

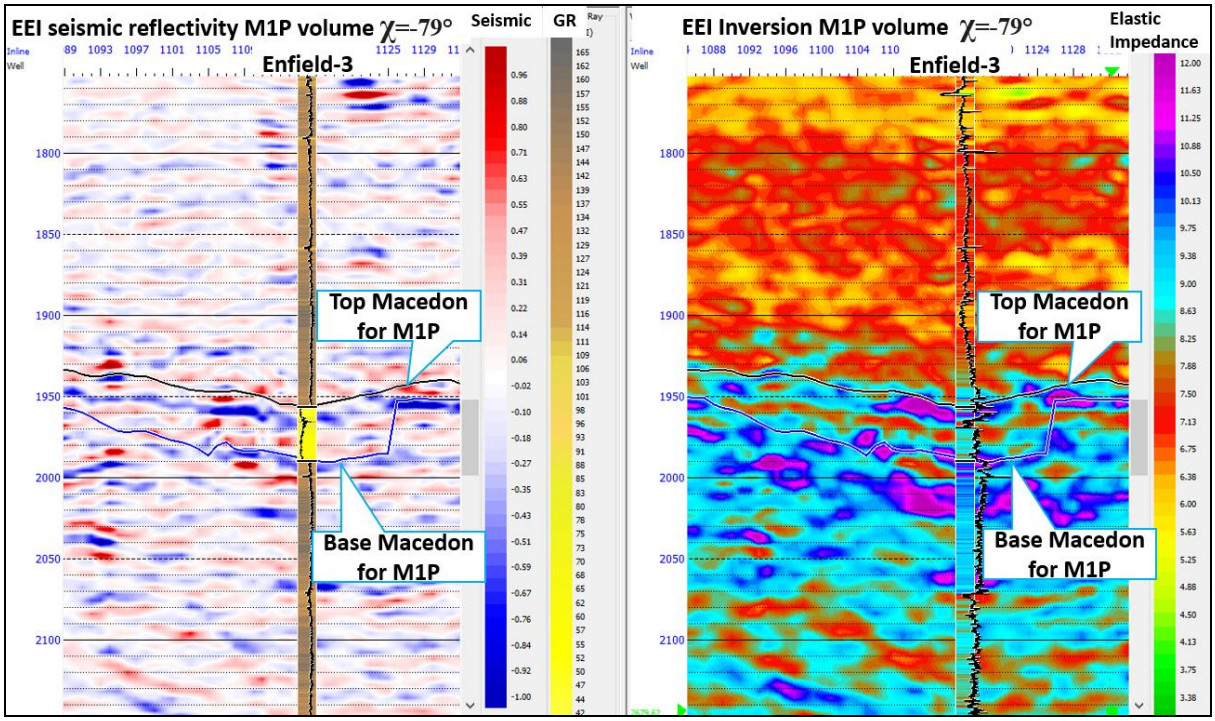

Figure 25. Left is the cross section of seismic reflectivity intercept/gradient M1P volume rotated to χ=-79° angle. Section of crossline 2075 is going across the Enfield-3 well with gamma ray log showing the reservoir. Right cross section is Extended Elastic Impedance of inverted Extended Elastic Impedance for M1P volume rotated to χ=-79° angle. Log is Elastic Impedance rotated to χ=-79° angle. Note the noisy character of the seismic and fair inversion results at this large angle of rotation.

A.3

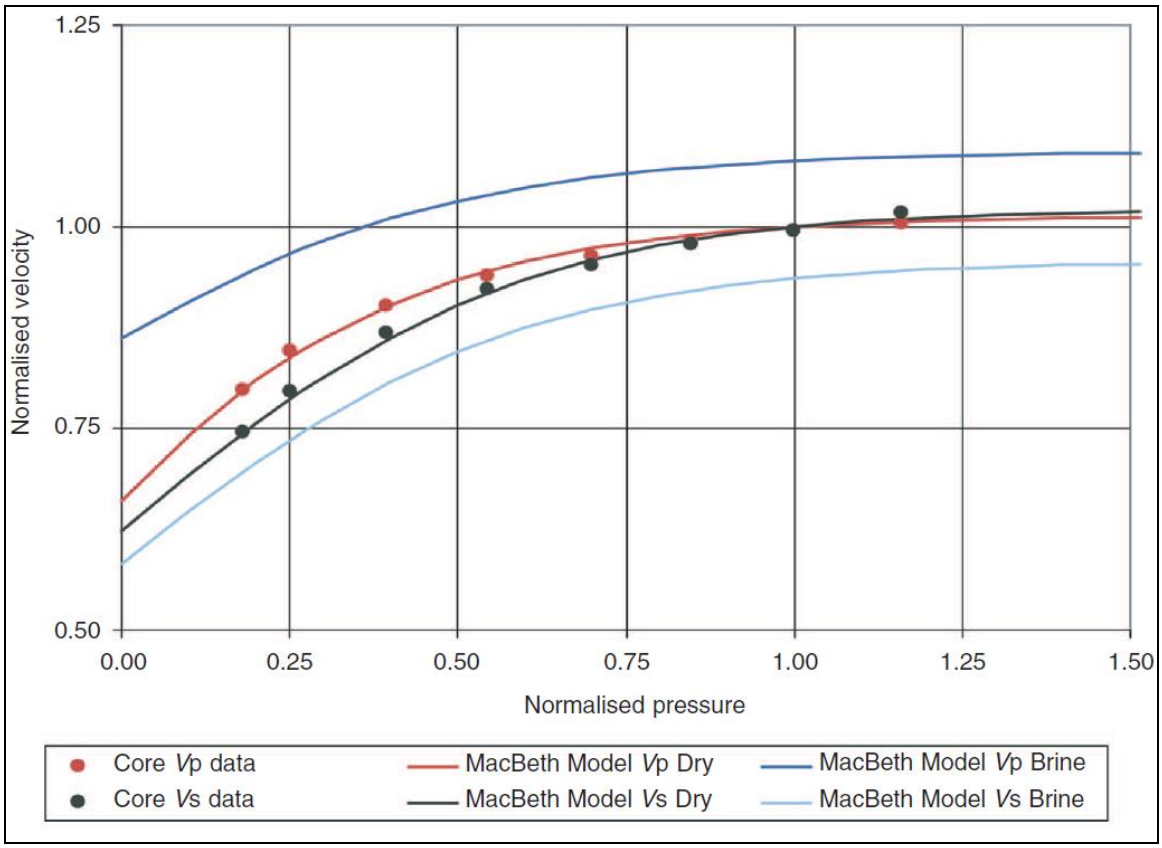

Figure 26. Enfield rock-physics pressure vs velocity model for the clean sand end-member: Normalised V_p and V_s as a function of Normalised Effective Stress (from Wulff et al., (2008). Normalised V_p, V_s = 1.0, and Normalised Effective Stress = 1.0 represent in-situ conditions. Points show ultrasonic dry core data (red: V_p, black: V_s); curves show V_p and V_s predictions using MacBeth's model for dry and brine-saturated sandstones. Normalised V_p Brine and Normalised V_s Brine are shown relative to dry rock velocities at in-situ pressure.

A.4

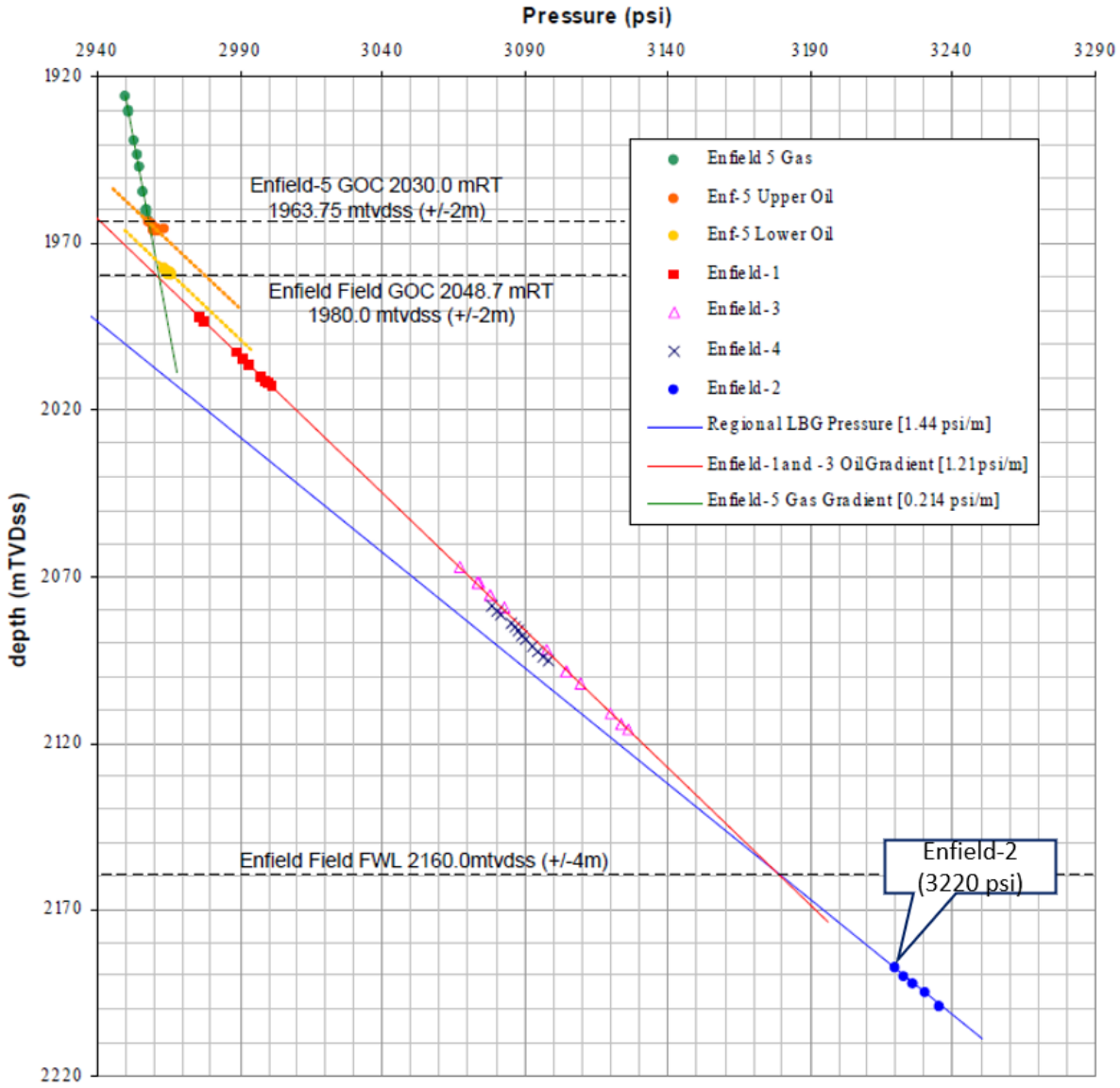

Figure 27. Normalised Macedon sand well pressure from Enfield exploration and appraisal wells. Modified from Wills (2003). Note: Macedon reservoir sand was intersected at the depth of 2188 mTVDSS at Enfield-2 (blue dots) with corresponding pressure 3220 psi.

Normalized Pressure	dry Vp (normalized)	dry Vs (normalized)	brine Vp (normalized)	brine Vs (normalized)	VP Brine Assuming EN2 values (m/s)	Vs Brine Assuming EN2 values (m/s)	Pressure assuming EN2 values (psi)	Using Density (g/cc)	AI	GI (average values are those at pressure =1)	ln (AI)	ln (GI)	Chi from 1.00 (norm)
1.50	1.011	1.018	1.090	0.9532	3177	1857	4830	2.26	7181	6836	8.879	8.830	-79.5
1.25	1.008	1.013	1.088	0.9494	3173	1849	4025	2.26	7171	6899	8.878	8.839	-79.0
1.00	0.998	0.998	1.082	0.9358	3153	1823	3220	2.26	7126	7126	8.871	8.871	
0.75	0.980	0.968	1.066	0.9056	3109	1764	2415	2.26	7026	7670	8.857	8.945	-79.2
0.50	0.934	0.902	1.032	0.8437	3010	1643	1610	2.26	6802	8973	8.825	9.102	-78.6
0.25	0.836	0.784	0.967	0.7341	2818	1430	805	2.26	6369	12183	8.759	9.408	-78.2
0.00	0.662	0.623	0.863	0.5823	2514	1134	0	2.26	5683	20185	8.645	9.913	-77.7

Figure 28. Calculation of the reservoir from normalised pressure and χ optimal angle for pressure.

Highlighted cells are data for the in-situ reservoir pressure of 3220 psi for Enfield-2.

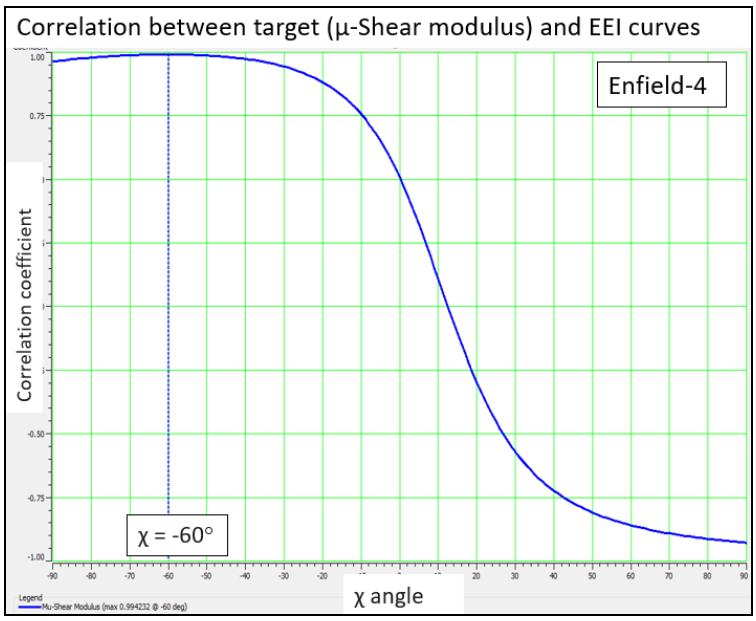

a)

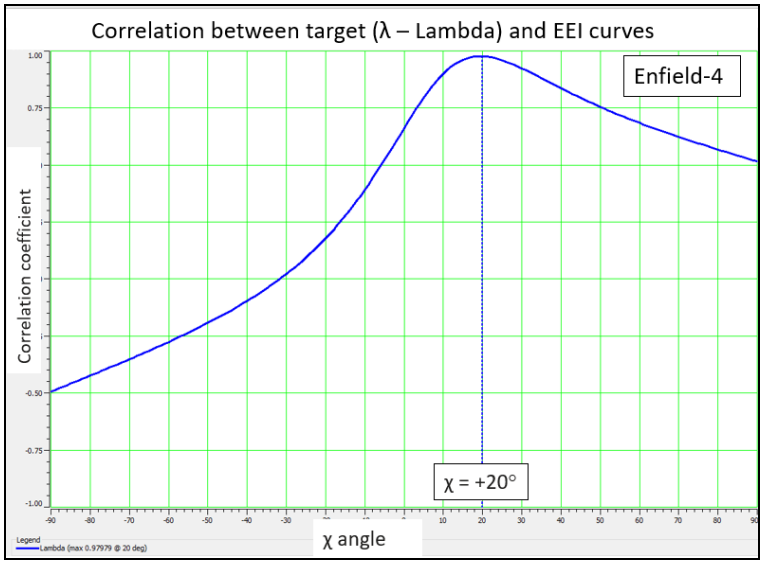

b)

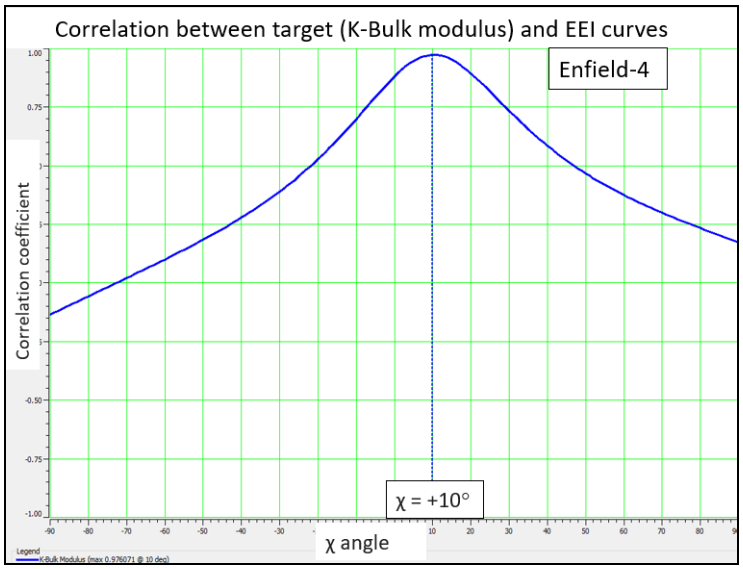

c)

Figure 29. Computation of the optimal χ angles for λ, μ and K moduli for Enfield-4 well using logs.

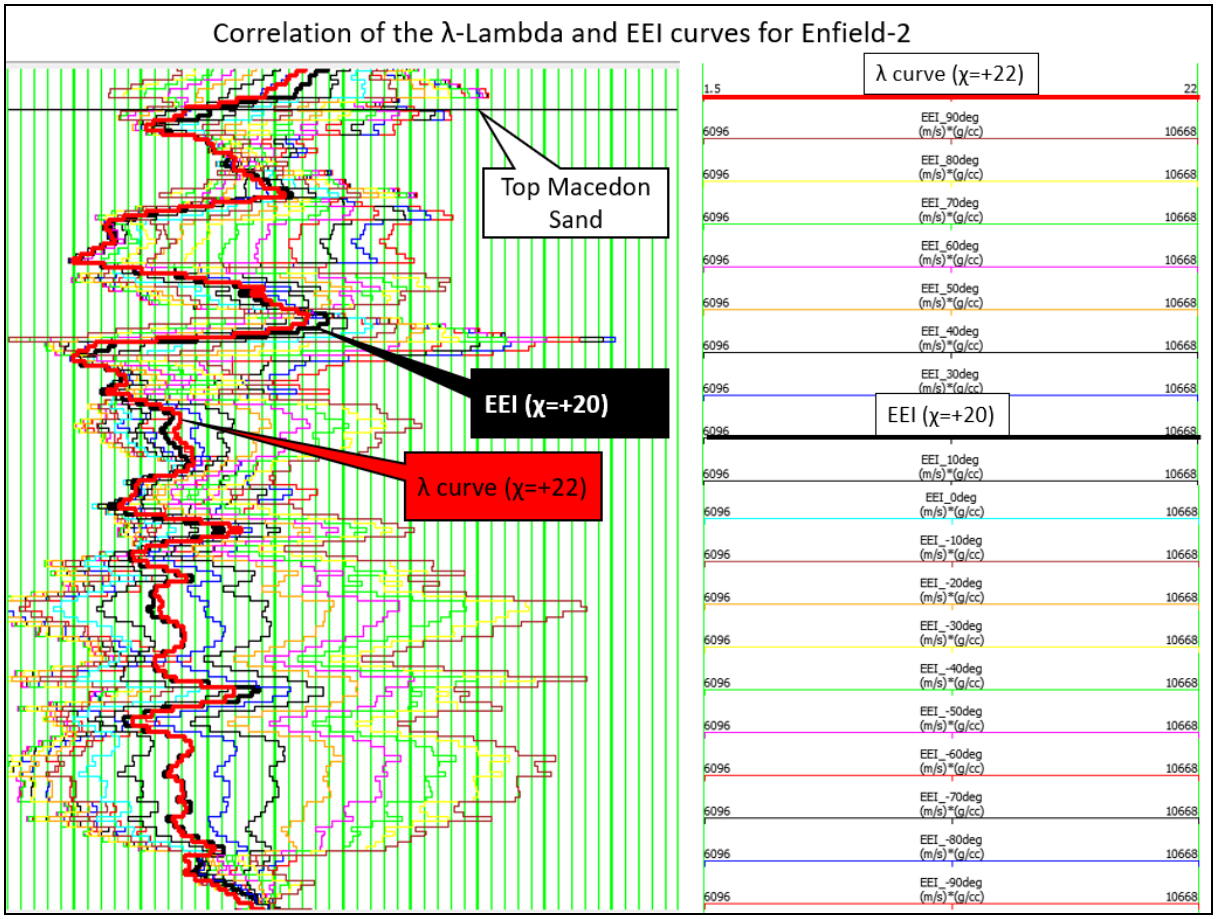

Figure 30. EEI logs computed and displayed for χ every 10°, from -90° to +90° range for Enfield-2 well. Highlighted black and red curves are EEI for χ=+20 and λ respectively.

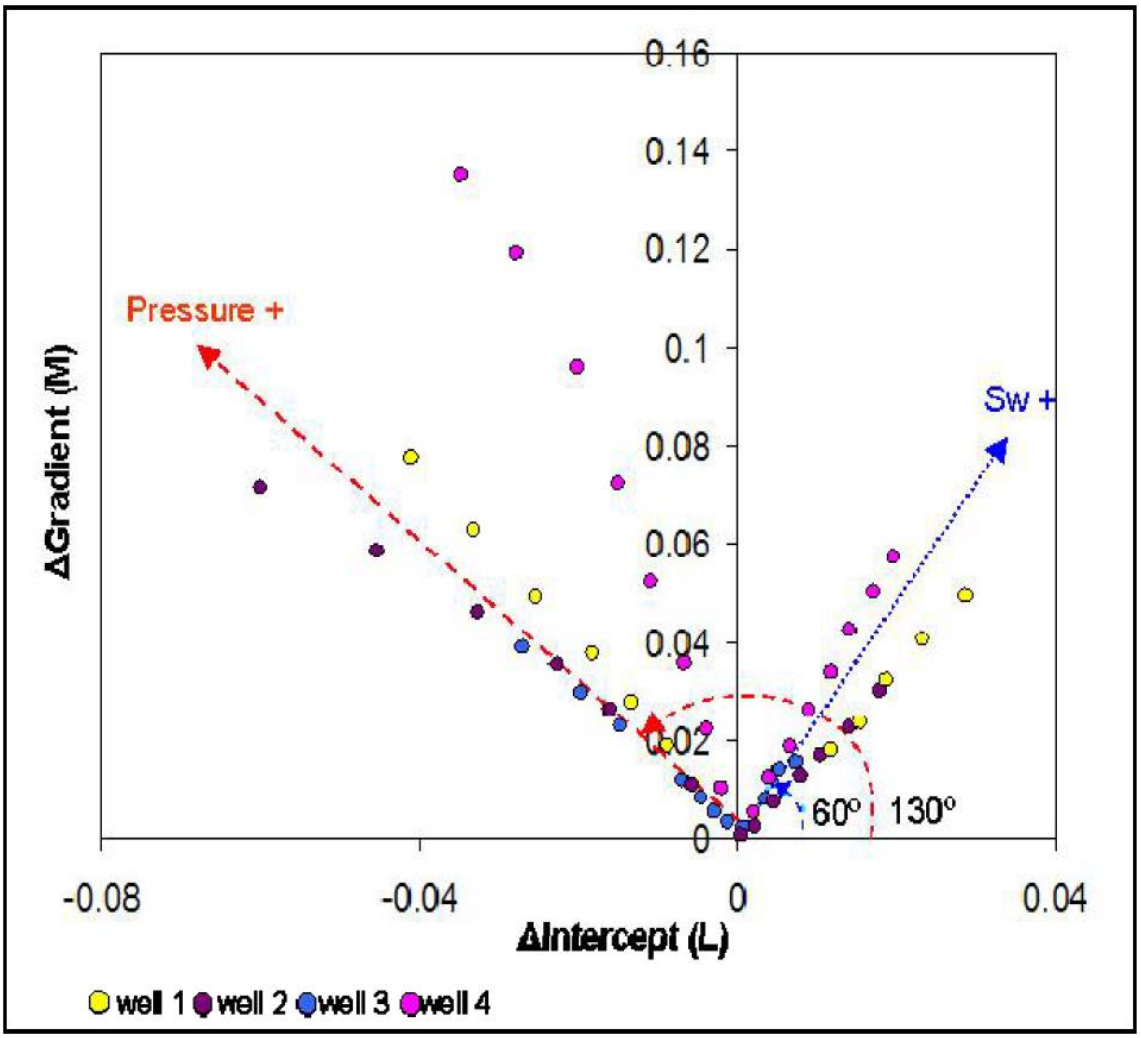

Figure 31. 4D AVO intercept and gradient difference plot for 4 appraisal Enfield-1, -2, -3 and -4 wells. Each point is an increase in water saturation and/or pressure from initial oil conditions. Gas increase (not plotted here) plots in -ΔM and -ΔL space, separate from increasing reservoir pressure (Smith et al., 2008).

Appendix A

VP Brine Assuming EN-2 values (m/s)	Vs Brine Assuming EN-2 values (m/s)	Pressure assuming EN-2 values (psi)	Using Density (g/cc)	Lithostatic ΔP (psi)	Reservoir (pore) ΔP (psi)	EEI(-79°) (ft/s)*(g/cc) using Whitcombe formula	EEI(-79°) (km/s)*(g/cc)	ΔEEI(-79°) (km/s)*(g/cc)	Reservoir (pore) ΔP (psi) scaled to polygon C
3177	1857	4730	2.26	1610	-1610	7435.510435	2.266343508	0.09362598	-1095
3173	1849	3941	2.26	805	-805	7366.571032	2.245330779	0.07261325	-547
3153	1823	3220	2.26	0	0	7128.338576	2.172717528	0	0
3109	1764	2365	2.26	-805	805	6613.546377	2.015808871	-0.15690866	547
3010	1643	1577	2.26	-1610	1610	5634.600652	1.717426224	-0.4552913	1095
2818	1430	788	2.26	-2415	2415	4121.534762	1.256243755	-0.91647377	1642
2514	1134	0	2.26	-3220	3220	2456.64627	0.748785759	-1.42393177	2190

Figure 32. Calculation the change of the reservoir (pore) pressure and scaling pressure calculated from Wulf's rock-physics model to ΔEEI for χ=-79° inversion map. Highlighted cells are data for the in-situ reservoir pressure of 3220 psi for Enfield-2.

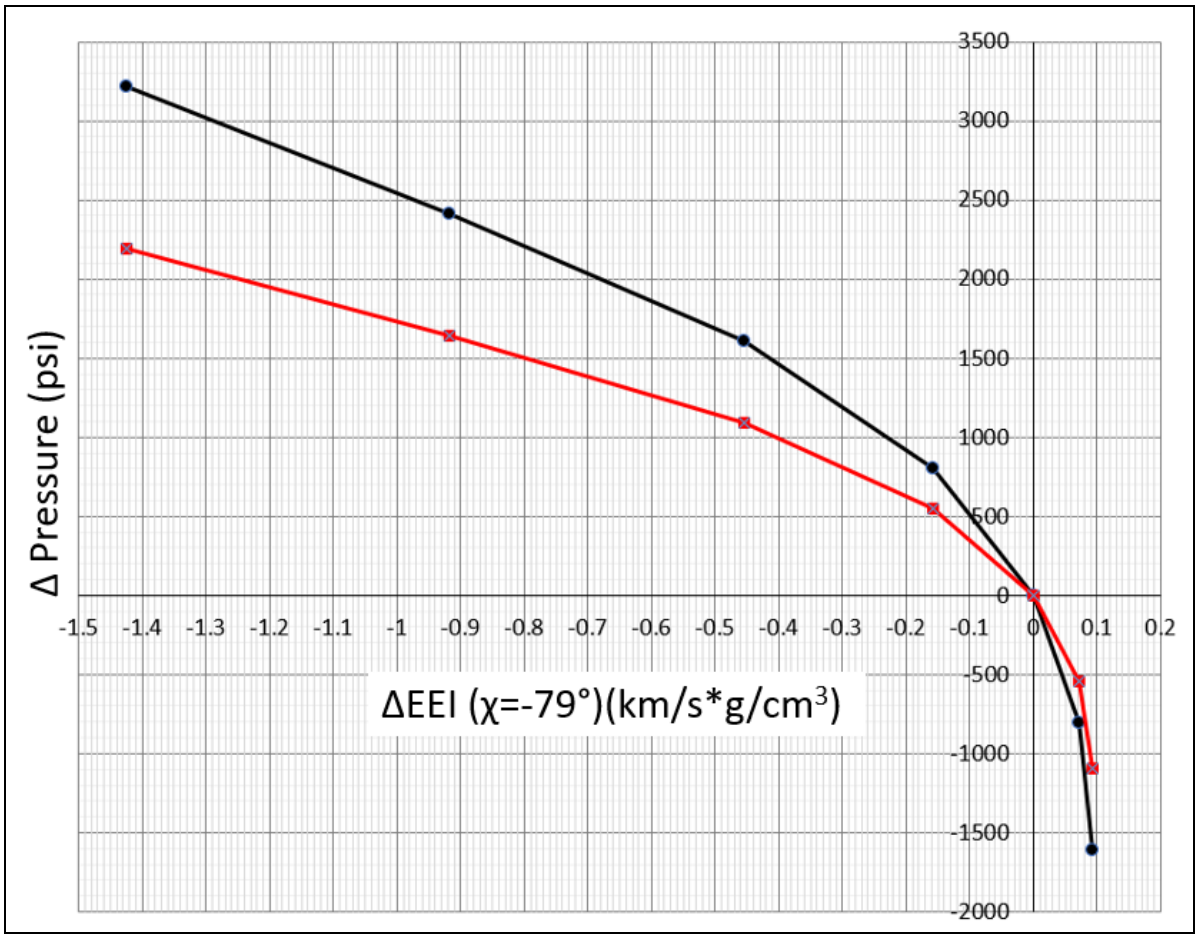

Figure 33. Red graph is the relationship between Macedon sand reservoir pressure change ΔP (psi) and ΔEEI(χ=-79°) scaled to change in reservoir (pore) pressure (psi) from the wells and ΔEEI (km/s*g/cm^3) inversion for polygon C. Black graph is the original unscaled model.

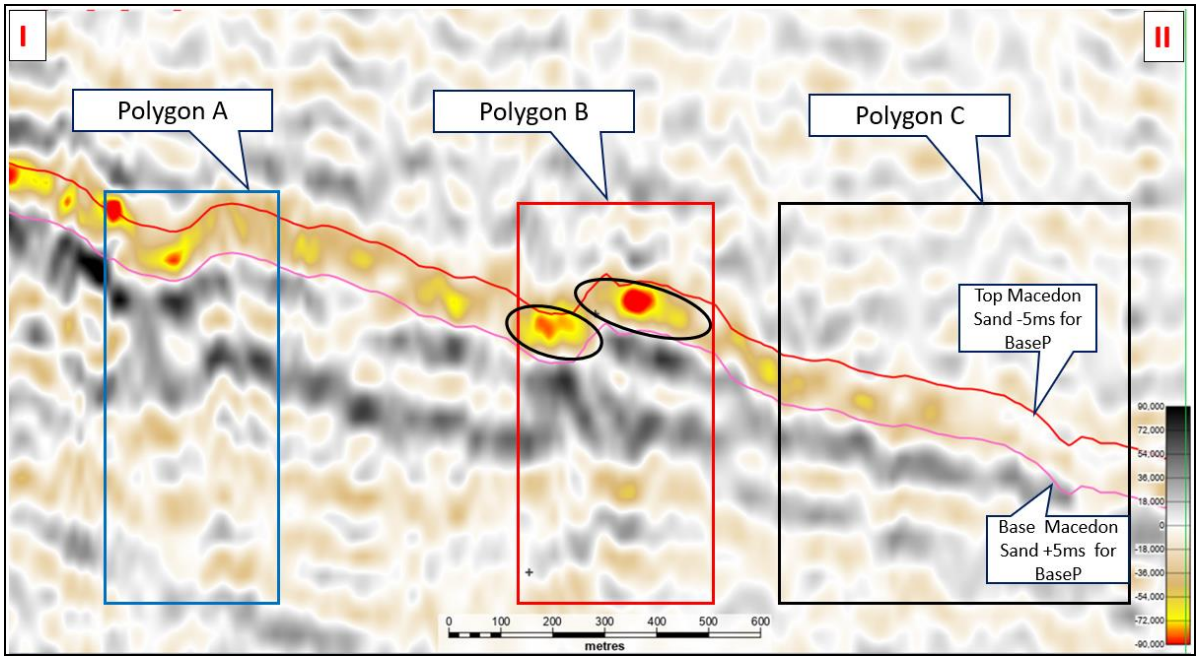

a)

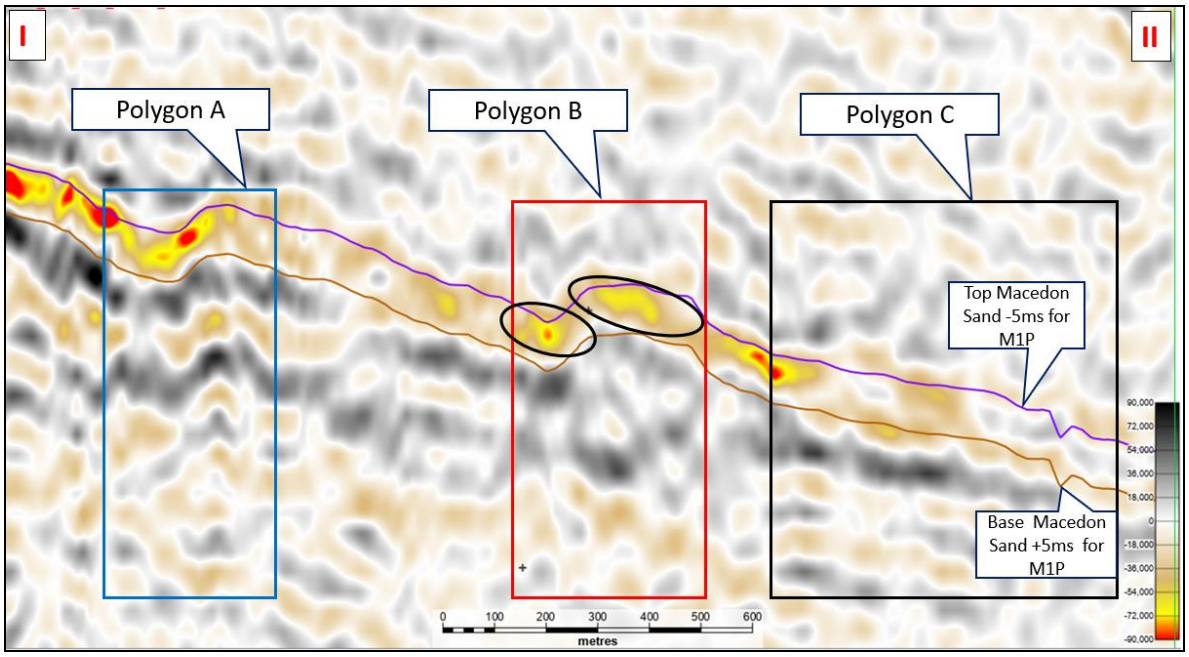

b)

Figure 34. Seismic reflectivity cross section I-II (Figure 15) for fluid change optimal angle χ=+42°. Rectangles are the projections of the polygons A, B and C from the map to the section. a) is the Base (BaseP) volume data. b) is the Monitor (M1P) volume data. Note the increase of the amplitude from

the top Macedon sand reservoir for M1P in the polygon B related to substitution of oil by water and highlighted by ellipses.

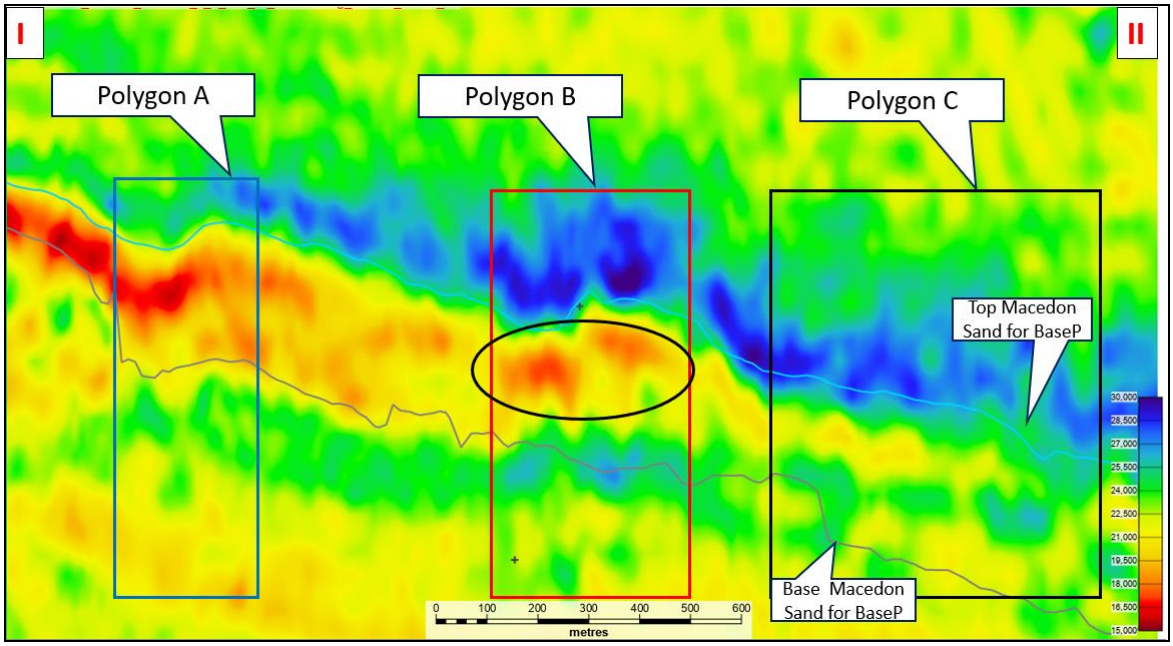

a)

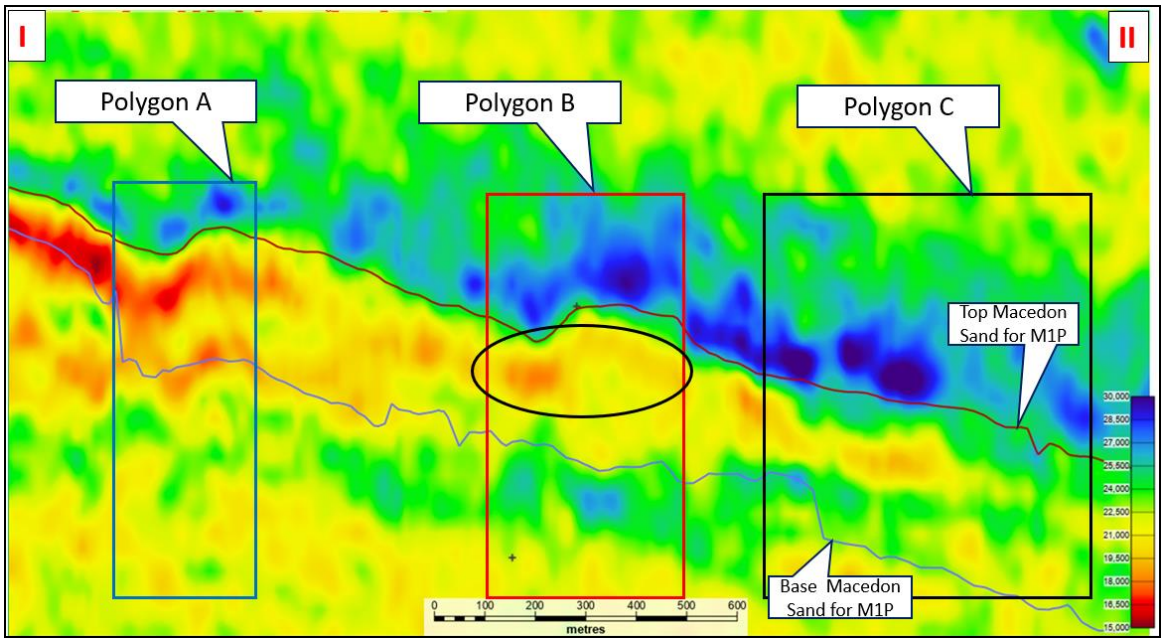

Figure 35. Seismic inversion cross section I-II (Figure 15) for fluid change optimal angle χ=+42°. Rectangles are the projections of the polygons A, B and C from the map to the section. a) is the Base (BaseP) volume data. b) is the Monitor (M1P) volume data. Note the increase of the amplitude from

the top Macedon sand reservoir for M1P in the polygon B related to substitution of oil by water and highlighted by ellipse.

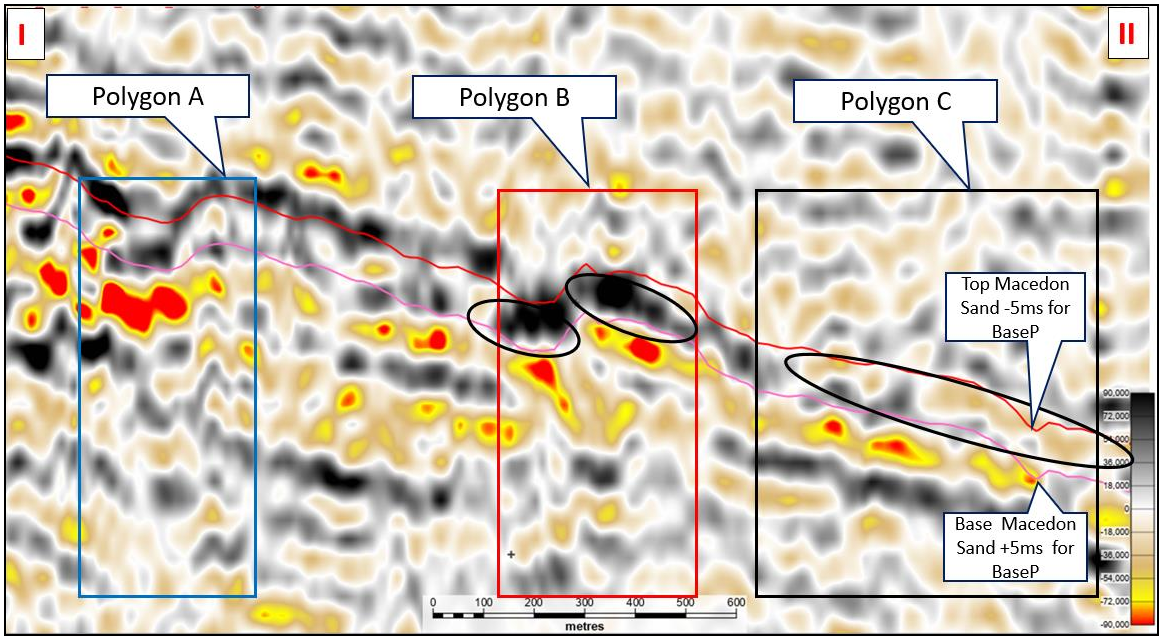

a)

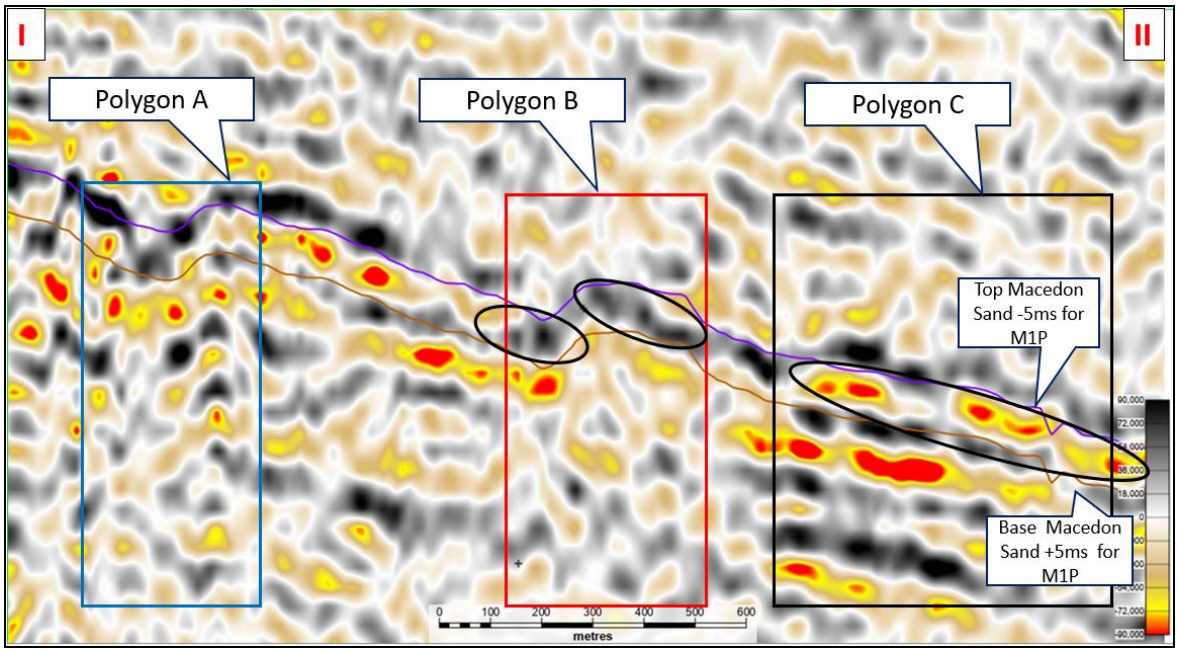

Figure 36. Seismic reflectivity cross section I-II (Figure 16) for pressure only change optimal angle χ=-79°. Rectangles are the projections of the polygons A, B and C from the map to the section. a) is the Base (BaseP) volume data. b) is the Monitor (M1P) volume data. Note the reduction of the

amplitude from the top Macedon sand reservoir for M1P in the polygon B and C related to reservoir pressure increase and highlighted by the ellipses.

b)

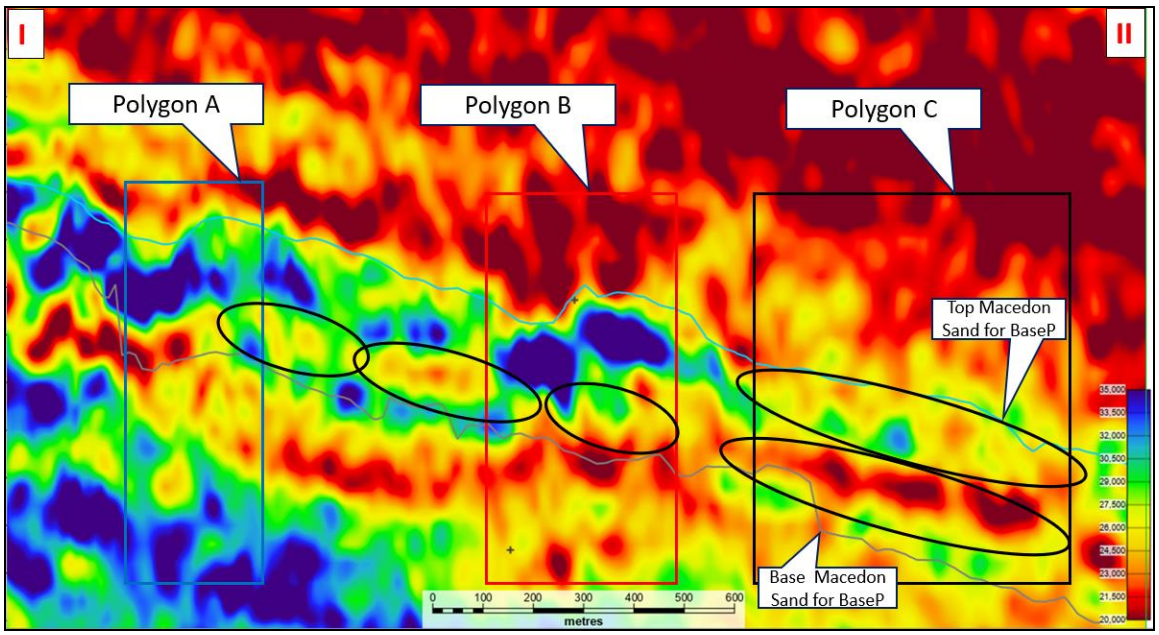

a)

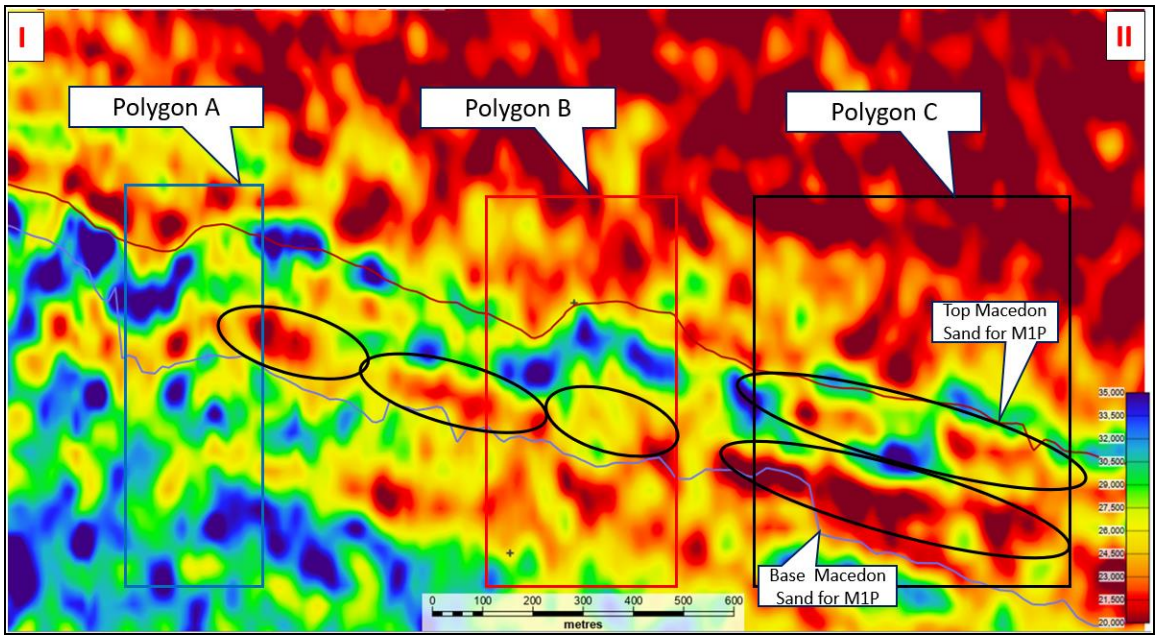

b)

Figure 37. Seismic inversion cross section I-II (Figure 16) for pressure change only optimal angle χ=-79°. Rectangles are the projections of the polygons A, B and C from the map to the section. a) is the Base (BaseP) volume data. b) is the Monitor (M1P) volume data. Note the reduction of the amplitude from the top Macedon sand reservoir for M1P in the polygons A, B and C related to related to reservoir pressure increase and highlighted by ellipses.

A.5

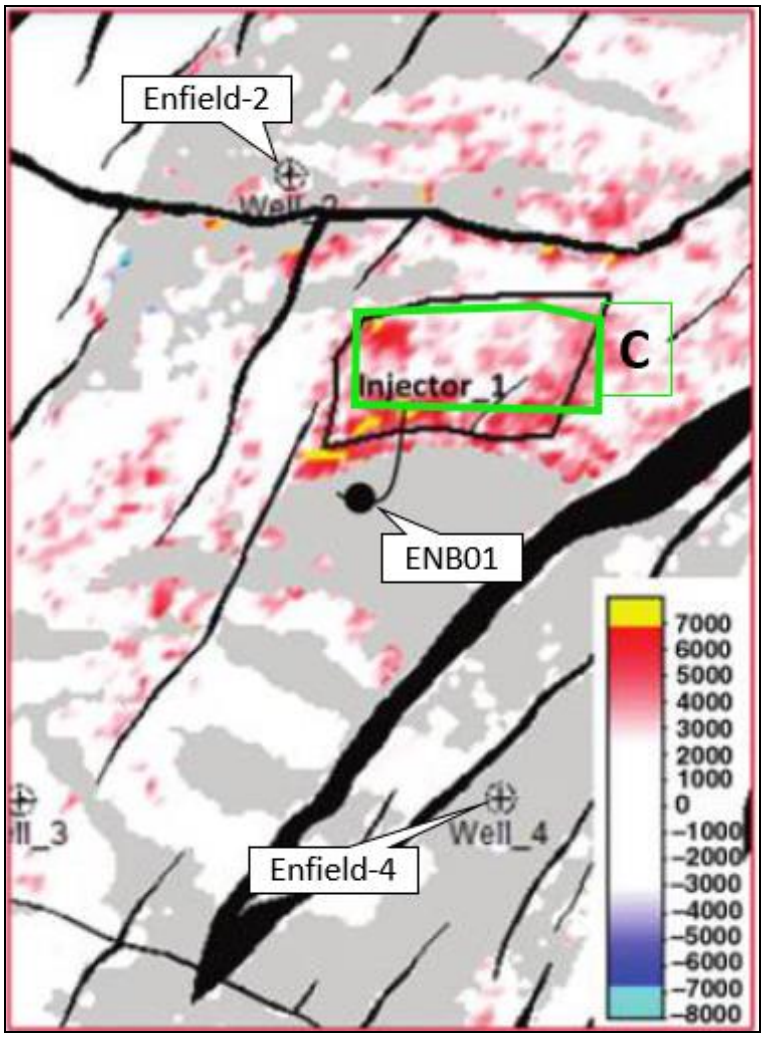

Figure 38. Image showing amplitude difference (the 50% increase for Monitor survey) using mid stacks within black polygon attributed to the pressure increase (modified from Saul and Lumley, 2015). Polygon C is shown as green polygon. Negative positive standard polarity (Sheriff and Geldard, 1995), (Author's assumption).

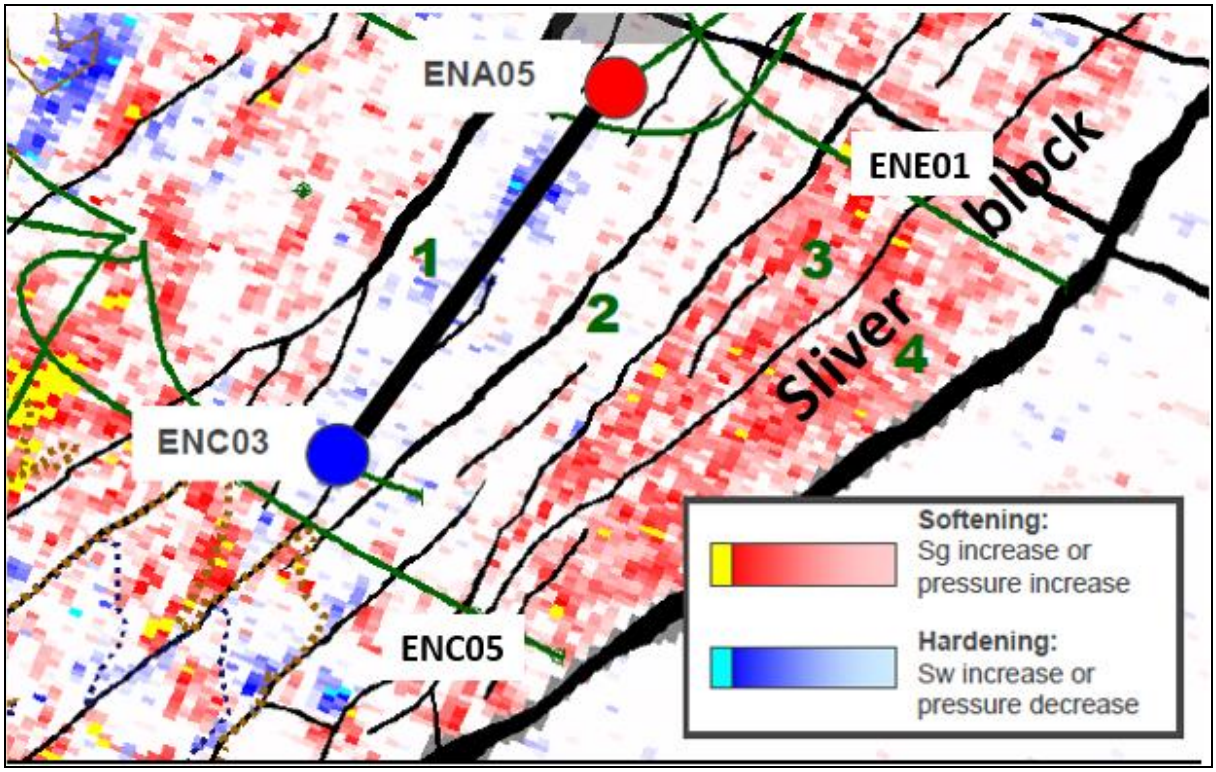

Figure 39. Image compiled by operator based on far stacks M1P-BaseP differences showing the pressure increase at the Slivers block (3 and 4 segments) modified from Hamson (2012). The anomaly corresponds with fluid-pressure increase at this block on Figure 19. The producer ENC05 well drilled to recover unswept the oil from this block.

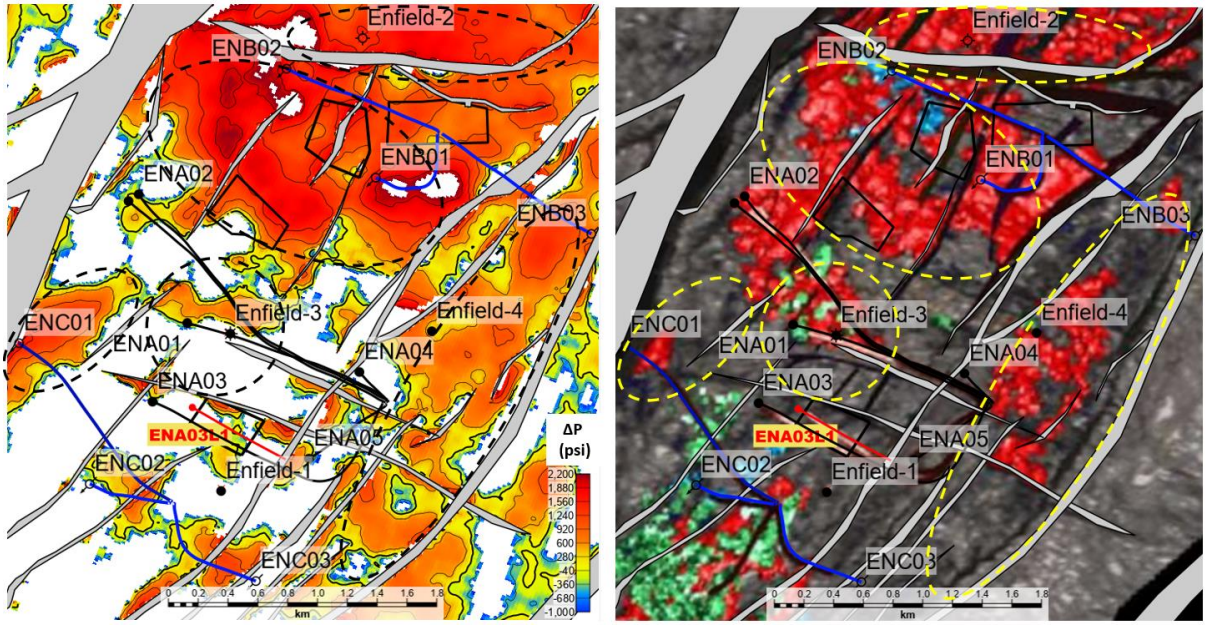

a) b)

Figure 40. a) Reservoir fluid-pressure change ΔP (psi) map, based on EEI inversion results. Highlighted contour is the pressure of 0 psi. b) Reservoir pressure change (red) and Water saturation change (blue) geographically rectified map using volume interpretation based on Acoustic Impedance and Poisson Ratio cross-plotting performed by operator (Woodside Energy) modified from Smith (2008). The corresponding anomalies from two interpretations are highlighted by black and yellow ellipses respectfully. (a) and (b) maps are geographically rectified.

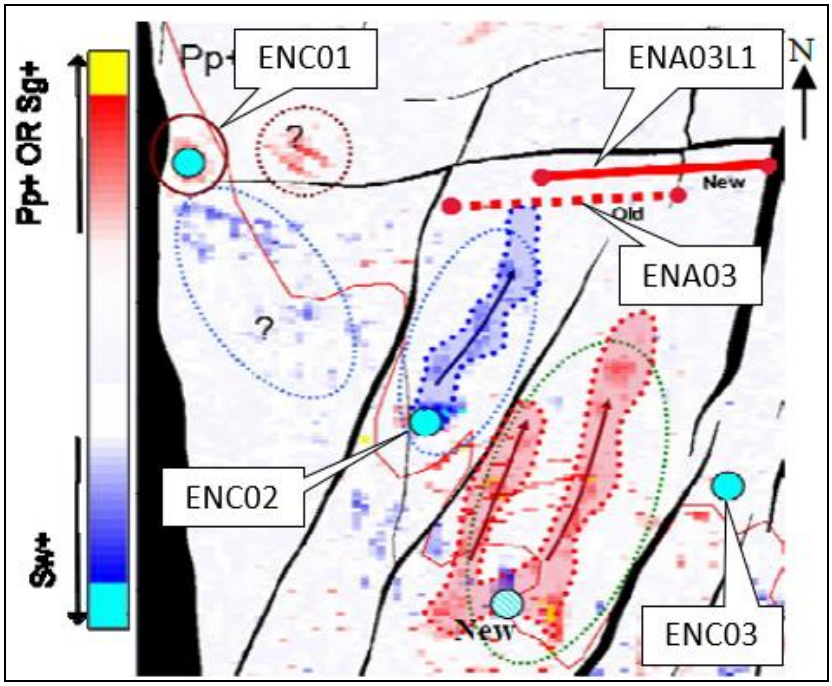

Figure 41. Image showing an elongated increased water saturation anomaly (blue) between ENC02 injector and ENA03 producer wells corresponding to anomaly L on Figure 20. The image is full stack amplitude difference of M1P-BaseP data compiled by operator (Smith et al., 2008).

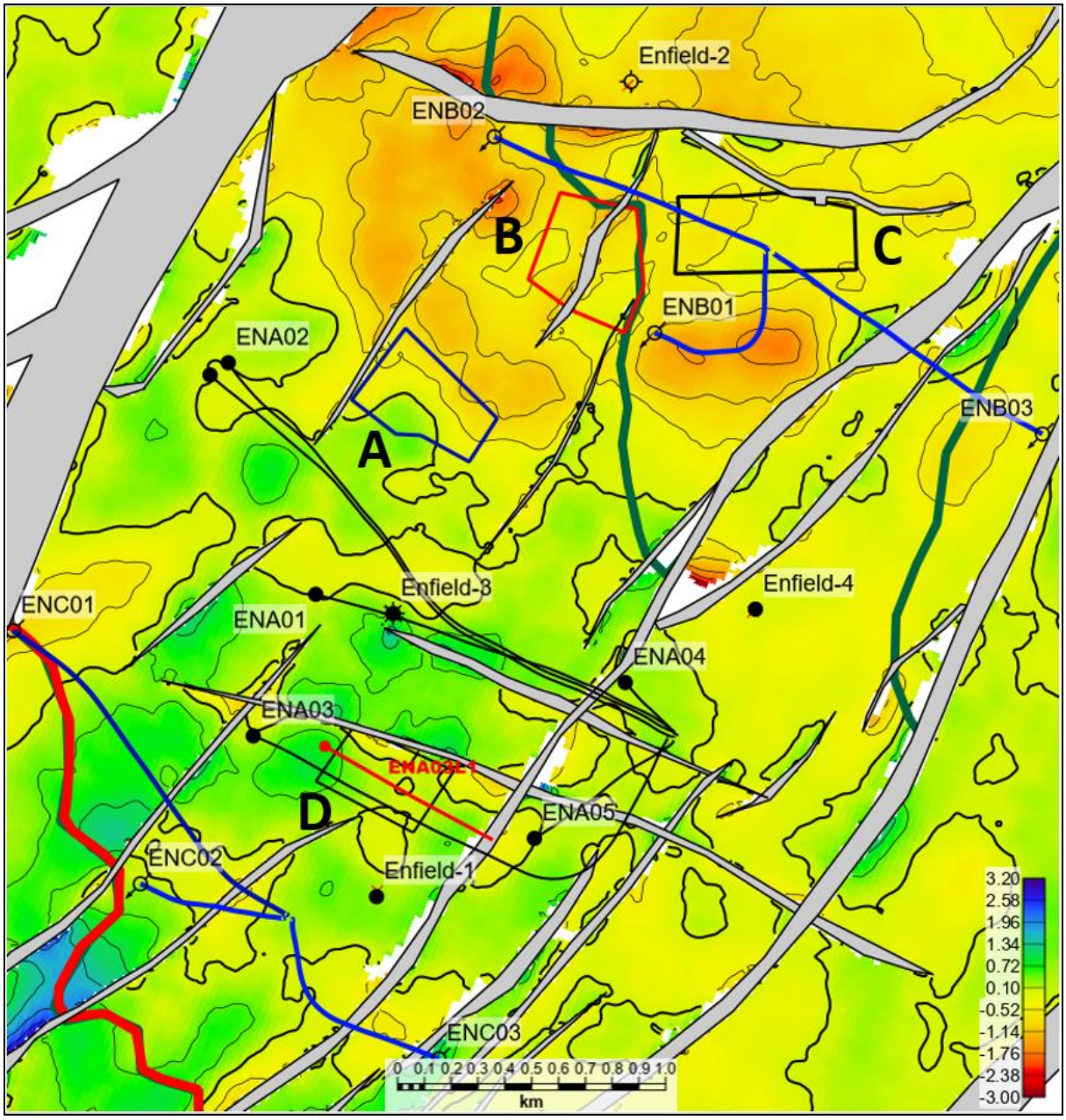

Figure 42. Inverted time-lapse difference map for EEI angle χ=-79°(km/s)*(g/cc). Smoothed with 150 m search radius. Thick contour is 0. Thin contour intervals are 0.5.

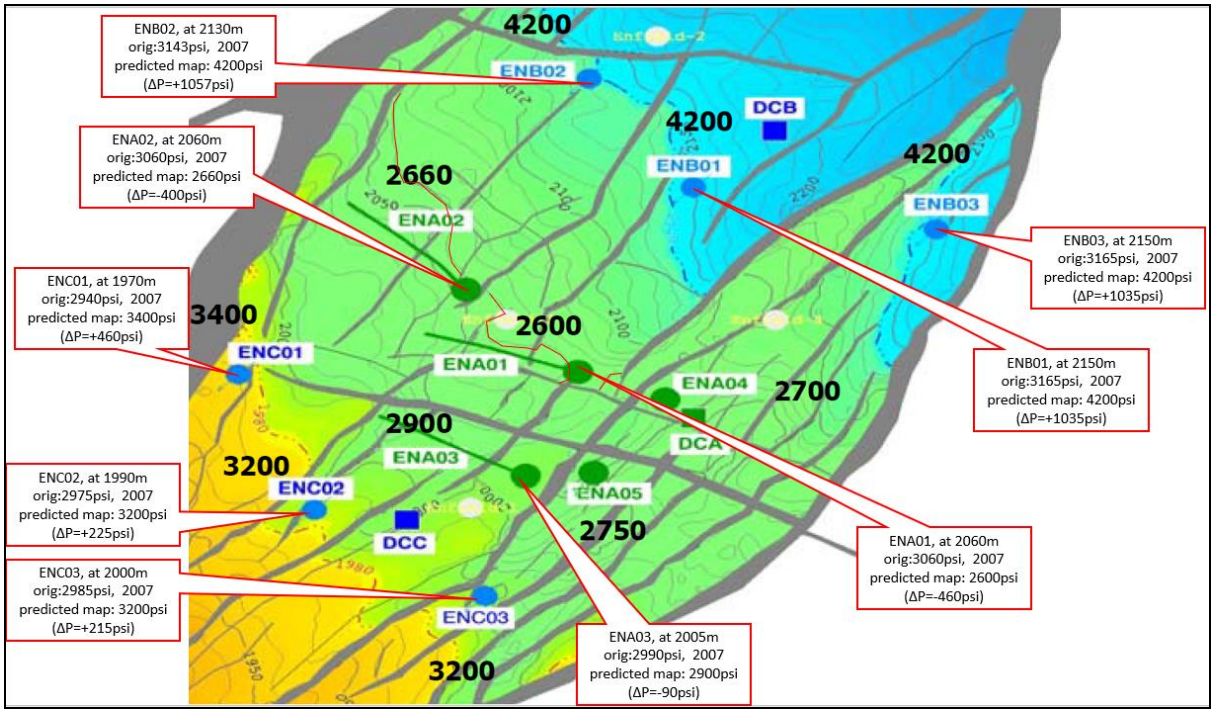

Figure 43. The depth TVDSS (m) at the top Macedon sand reservoir map modified from Smith (2008). The map also displays localised well pressures (psi) predicted by operator (black values). I calculated the change in reservoir pressure ΔP for Monitor – Base time surveys assuming the pressure prediction by the operator is referred to the well symbols.

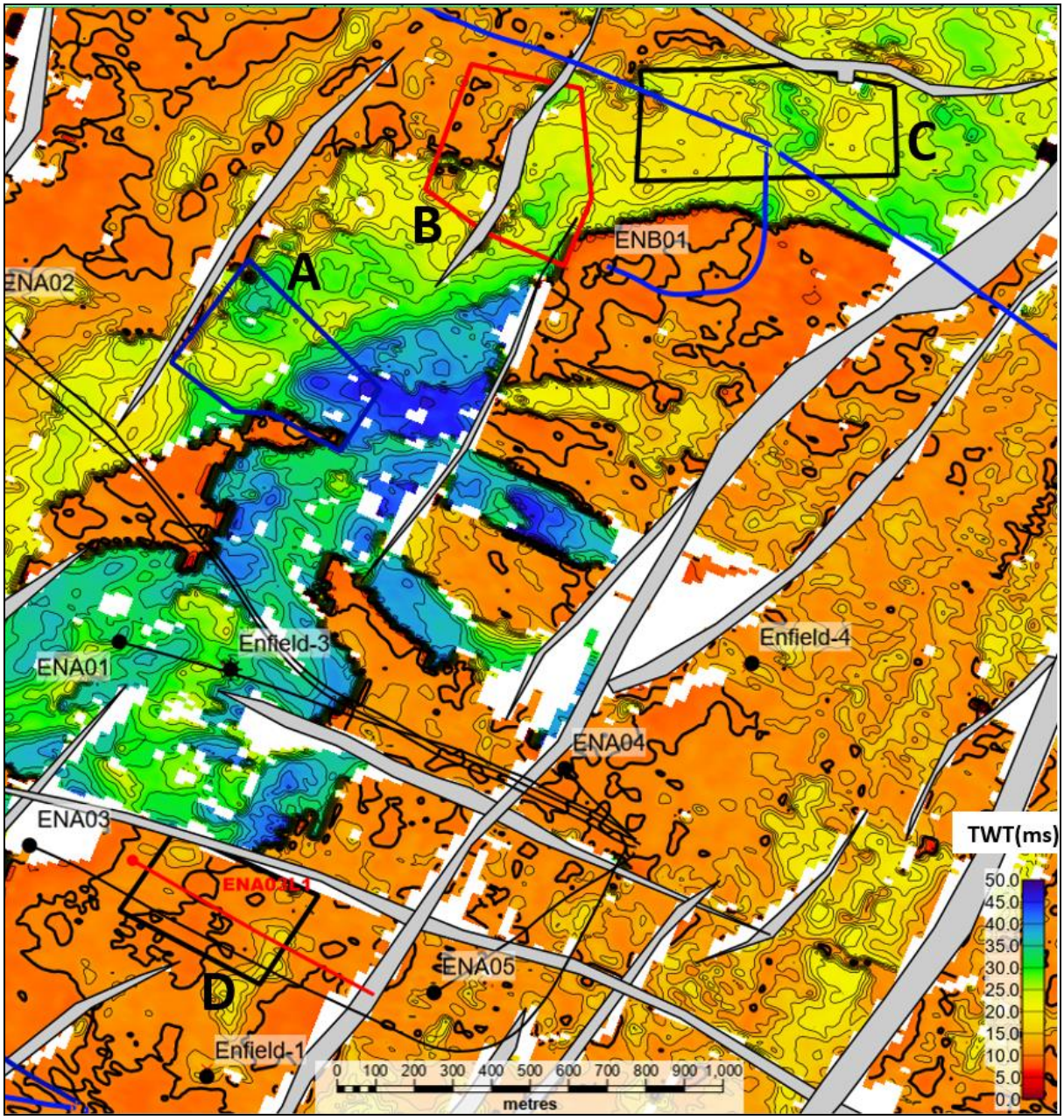

Figure 44. Isopach Macedon sand reservoir shown as two-way time. Contour interval is 2 ms. Thick contour is 10 ms as the thin-bed limits reference threshold is shown.

APPENDIX B

B.1 Quality control and seismic data conditioning

In this section, I will provide quality control results to assess the seismic data quality used in the thesis project. The relatively high of 50% for seismic data NRMS is a particular concern to affect the detectability of saturation and pressure changes. Another addressed issue is the thin bed tuning which also affects the quantitative and qualitative interpretation results. The other QC procedures and processing for data conditioning required for QI industry projects were also performed and presented in this appendix.

B 1.1 Spectral balancing

Due to anelastic attenuation, higher frequencies tend to attenuate increased distance, and thus the central frequency component decreases with increasing offsets. The effect of attenuation is ignored in AVO/EEI inversion and hence needs to be compensated for. The spectral balancing method allows us to balance the frequency spectrum for all stacked offset volumes.

The BaseP and M1P surveys of Near, Mid, Far and Ultra Far volumes originally processed by the processing contractor PGS had also been balanced during processing. The QC plot of these data shows that there was inconsistency/"noise" at 40Hz, 75Hz, and 110Hz (Figure 45a). I used DUG Insight's Spectral Shaping tool for additional spectral balancing. After applying the busting and adjustment of the frequency spectrums, the graph from the spectrally balanced volumes is plotted on Figure 45b with the results on Figure 46.

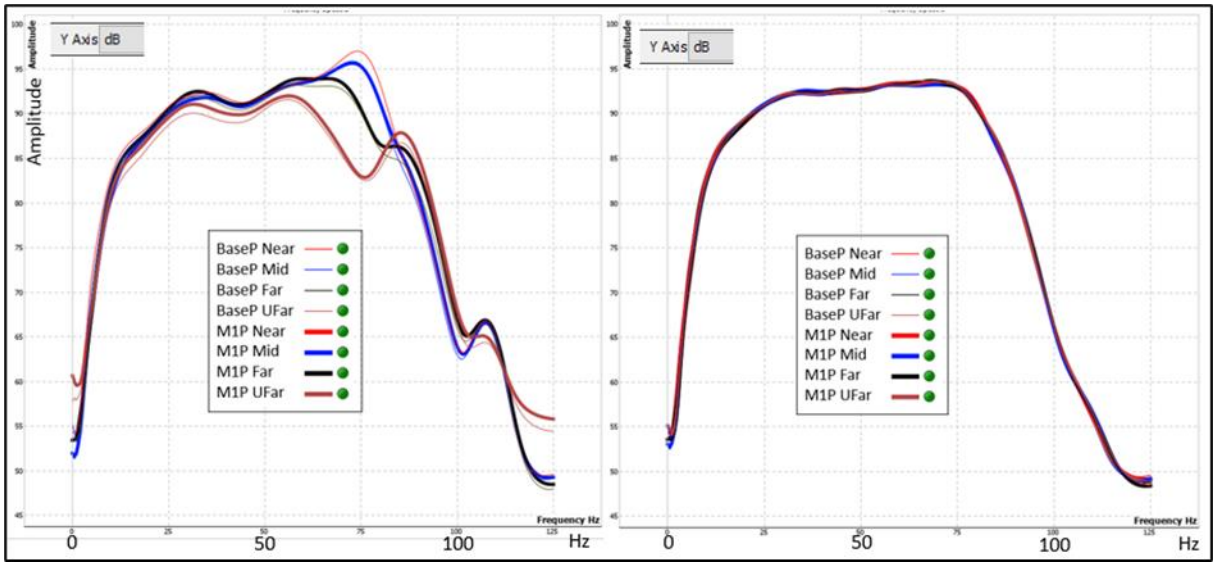

a) b)

Figure 45. The frequency spectrum of the data in frequency spectra DUG view window for BaseP and M1P seismic surveys for Near, Mid, Far and Ultra Far stack volumes: a) Before spectra balancing. b) After spectra balancing.

Appendix B

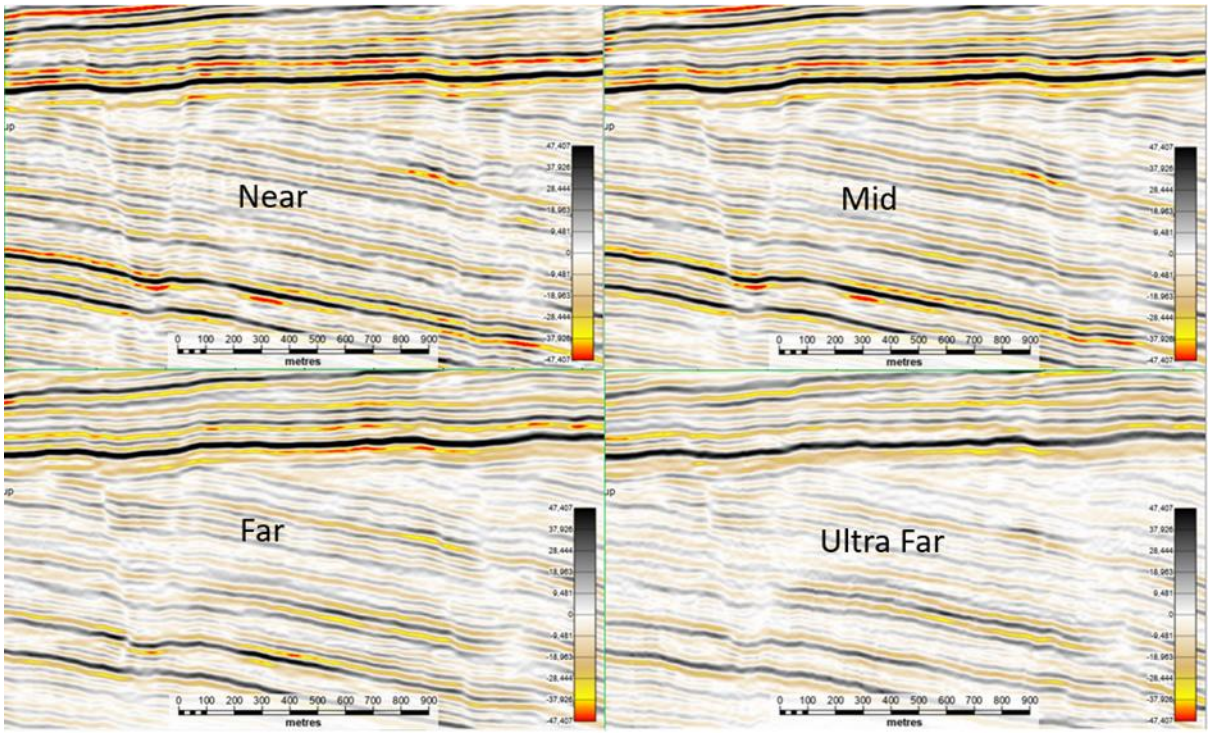

a)

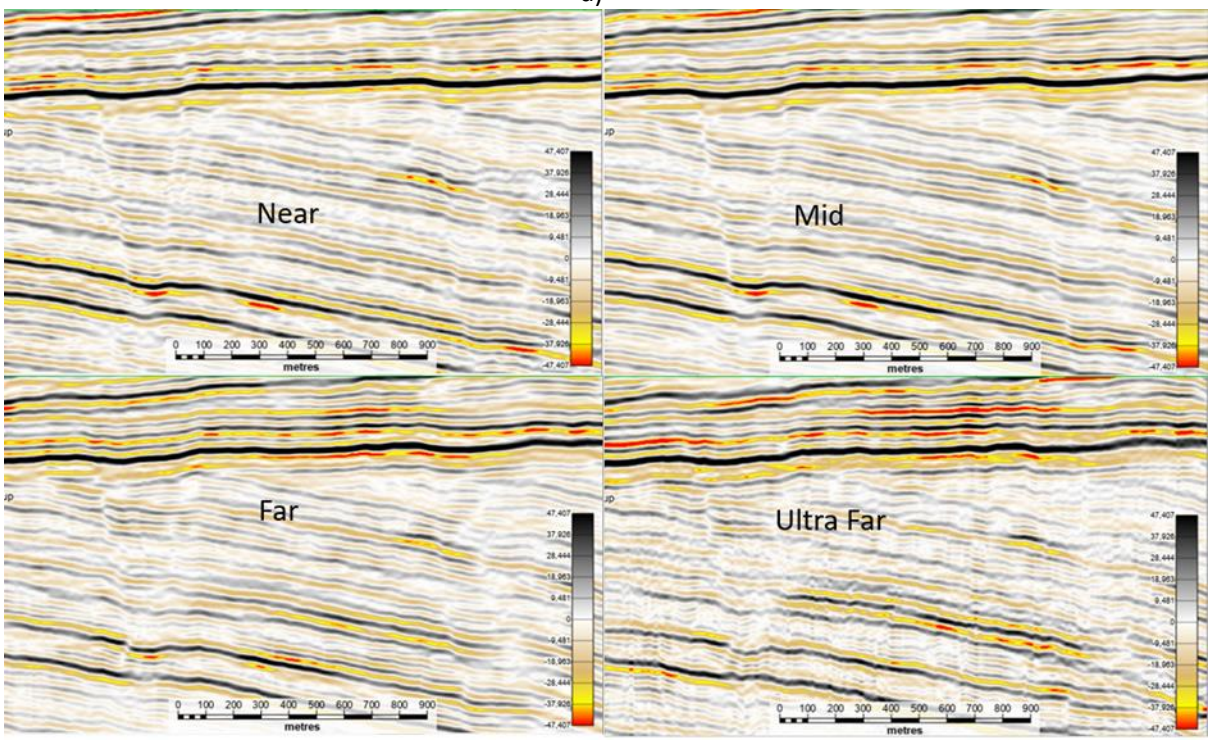

b)

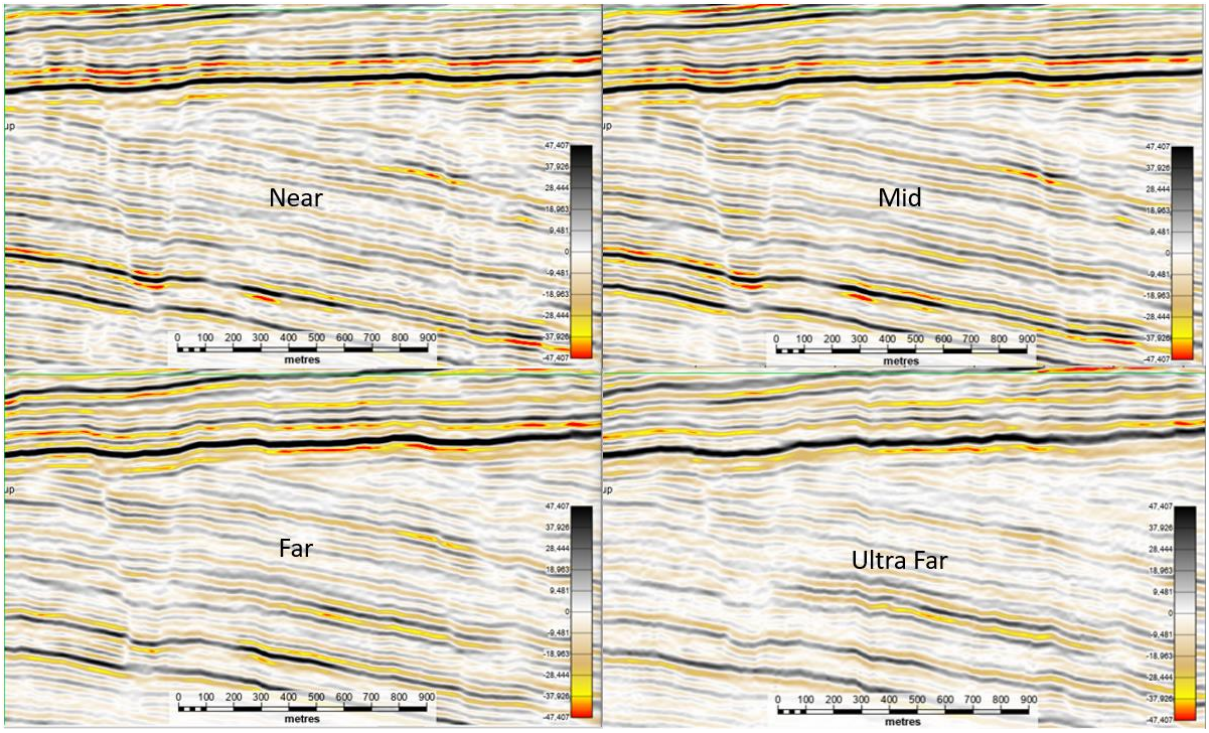

c)

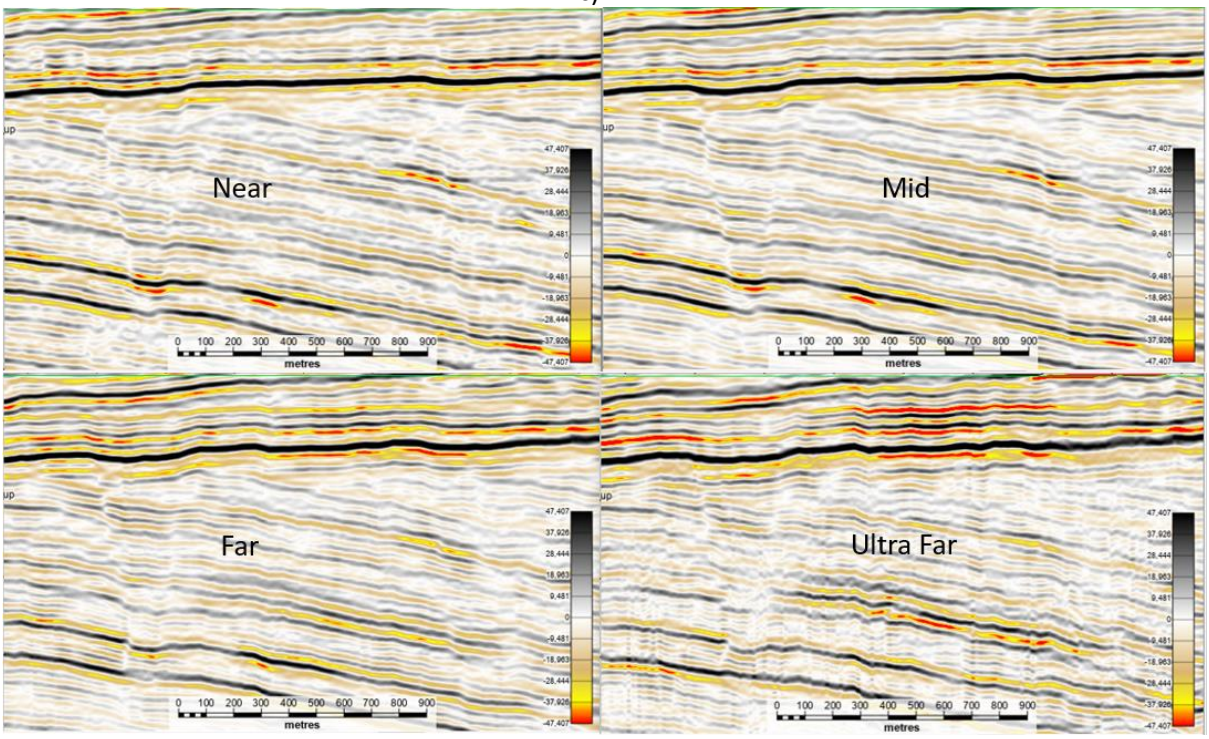

d)

Figure 46. Near, Mid, Far and Ultra Far stacks (Inline 1130, Crossline 2100-2440) above the Macedon sand reservoir: a - before spectral balancing, b – after spectral balancing for BaseP survey. c - before spectral balancing, d – after spectral balancing for M1P survey. Note the noisy Ultra Far Stack.

B 1.2 Stack volumes time alignment

Sometimes the small differences in the alignment of stacked AVO seismic data volumes can be present after processing and prevent accurate, direct (point-for-point) differencing of these data. This misalignment hinders the accurate calculation of three-dimensional volume-based seismic AVO attributes. In this case, partial stack volumes time alignment needs to be applied.

I have performed time alignment quality control for Near, Mid, Far and Ultra Far volumes. There was no significant misalignment between stack volumes (Figure 47). The time alignment of volumes originally processed by contractor BaseP and M1P surveys is good. The 4D time alignment was performed to align the base and monitor volumes – this was achieved by applying a single static solution to the trace:

- Pilot trace: Stack generated using the summed base and monitor RMO stack
- Cross-correlation windows: 4DQC (TO) horizon +/- 500ms
- Max-lag: 7ms

RMO processing additionally improved time alignment for the stacks within a crucial reservoir window described in chapter B 1.6. Thus, additional time alignment processing was not needed.

Appendix B

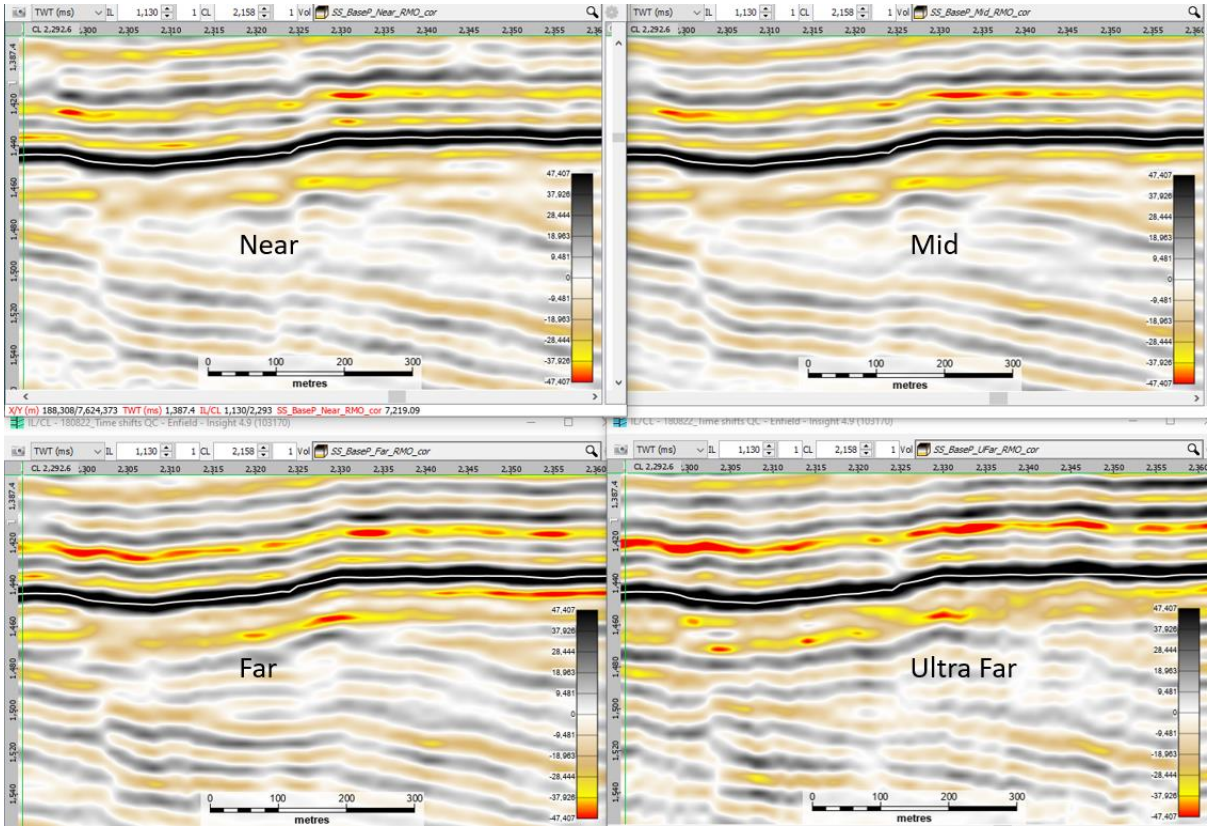

a)

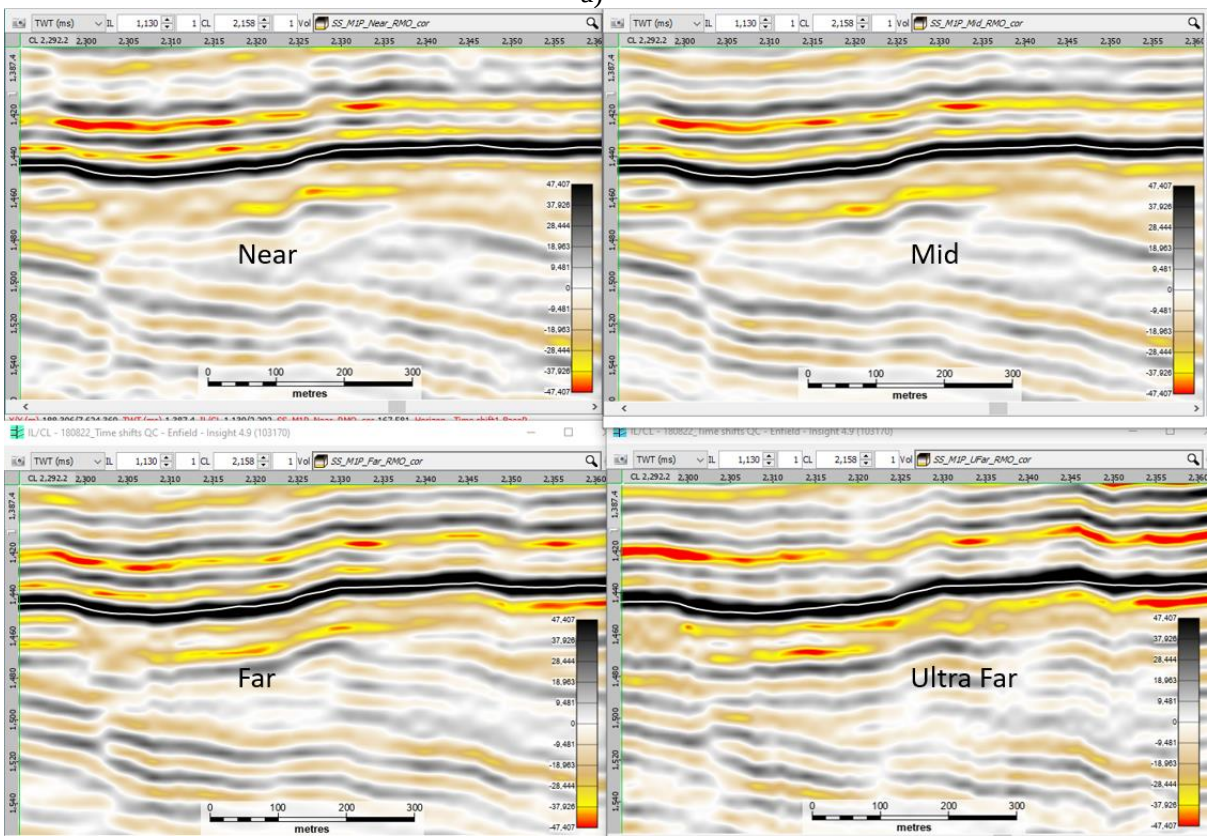

b)

Figure 47. Time alignment for quality control for Near, Mid, Far and Ultra Far stacks is shown on a) for BaseP survey and b) for M1P survey. Note, the shown white horizon has been propagated for Near stack and displayed on all stacks for comparison. Note some time misalignment on Ultra Far stack likely due to the noise.

The QC procedure shows that the Ultra Far stack is very noisy throughout all volumes for both BaseP and M1P surveys, mainly within 1800 - 2000ms time window, and strongly affected the reservoir (Figure 48). Thus, to avoid unreliable results, it was decided to use Near, Mid and Far stacks only in the AVO processing.

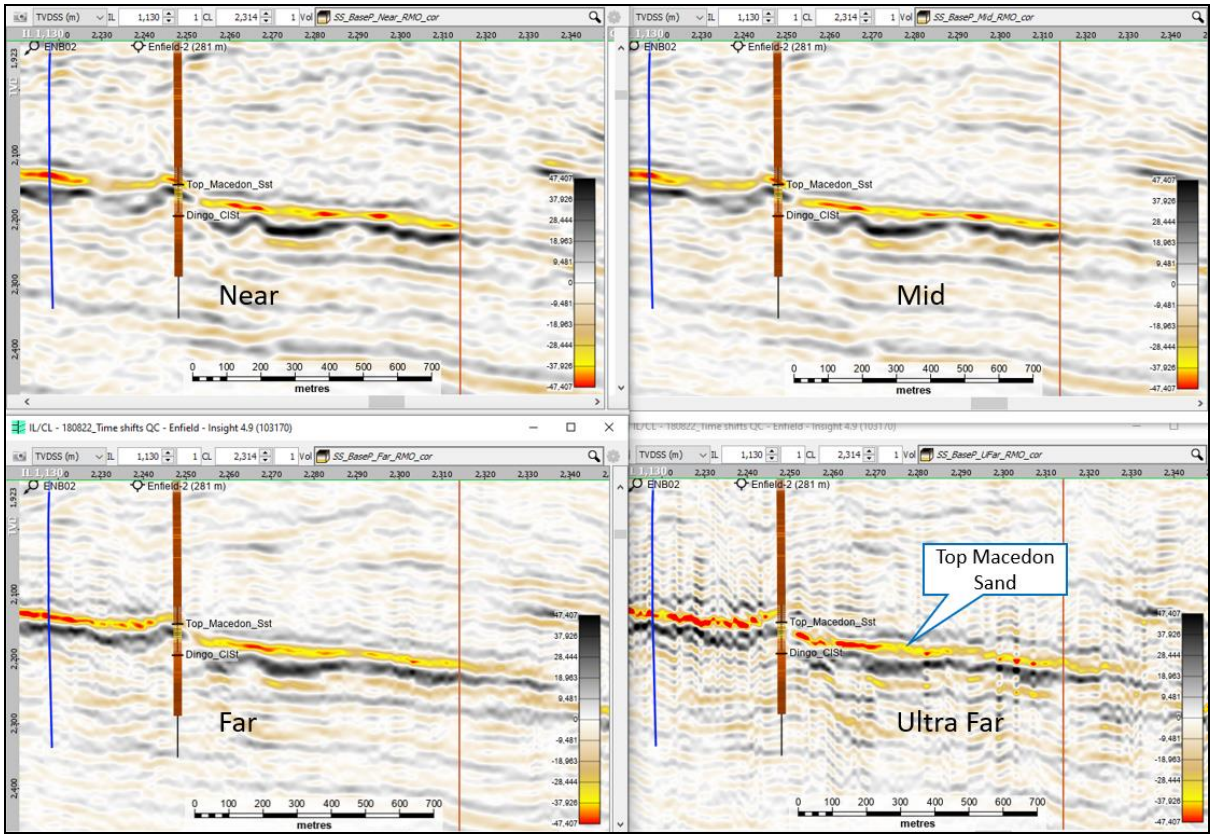

a)

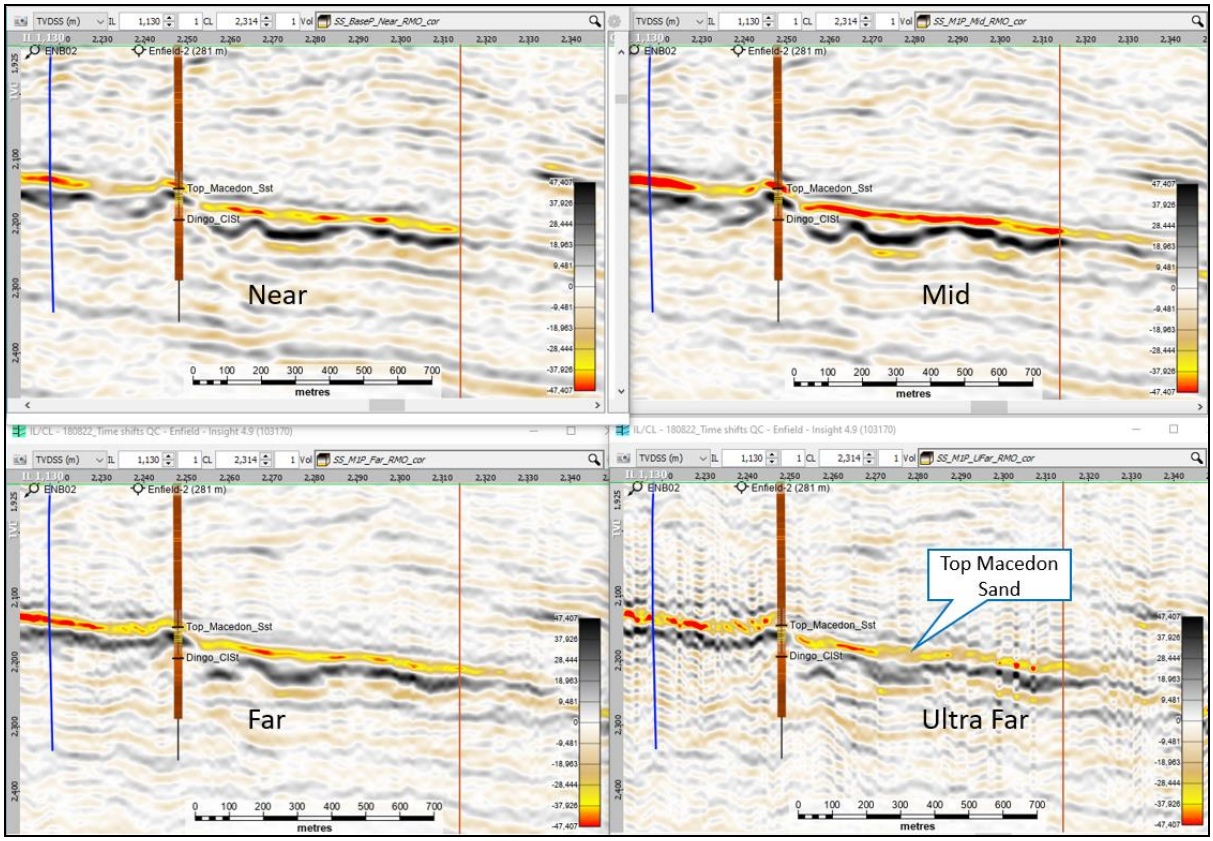

b)

Figure 48. Ultra Far stack with strong noise, affected reservoir is shown with other stacks for comparison for a) BaseP survey and b) M1P survey.

B 1.3 Wells tie

The seismic to well tie was done for the Top Macedon Sand and Base Macedon Sand as these horizons were used for structural interpretation and inversion. The VSP surveys were used for Enfield-1,2 and 4 wells and check shot survey for Enfield-3 to tie the wells (No velocity survey for Enfield-5 was available). Figure 49 presents the well tie for Enfield-3 (a, b) and Enfield-4 (c, d) for Near, Mid and Far stacks. There is some problematic tie misalignment for Near stack for Enfield-4 due to the presence of a 2 m-thick shale within the sand reservoir (which is well below seismic resolution but significant enough to distort the

seismic response) and very high-density sand intervals within the reservoir. Well tie for two-way time seismic is shown on an arbitrary line in Figure 50.

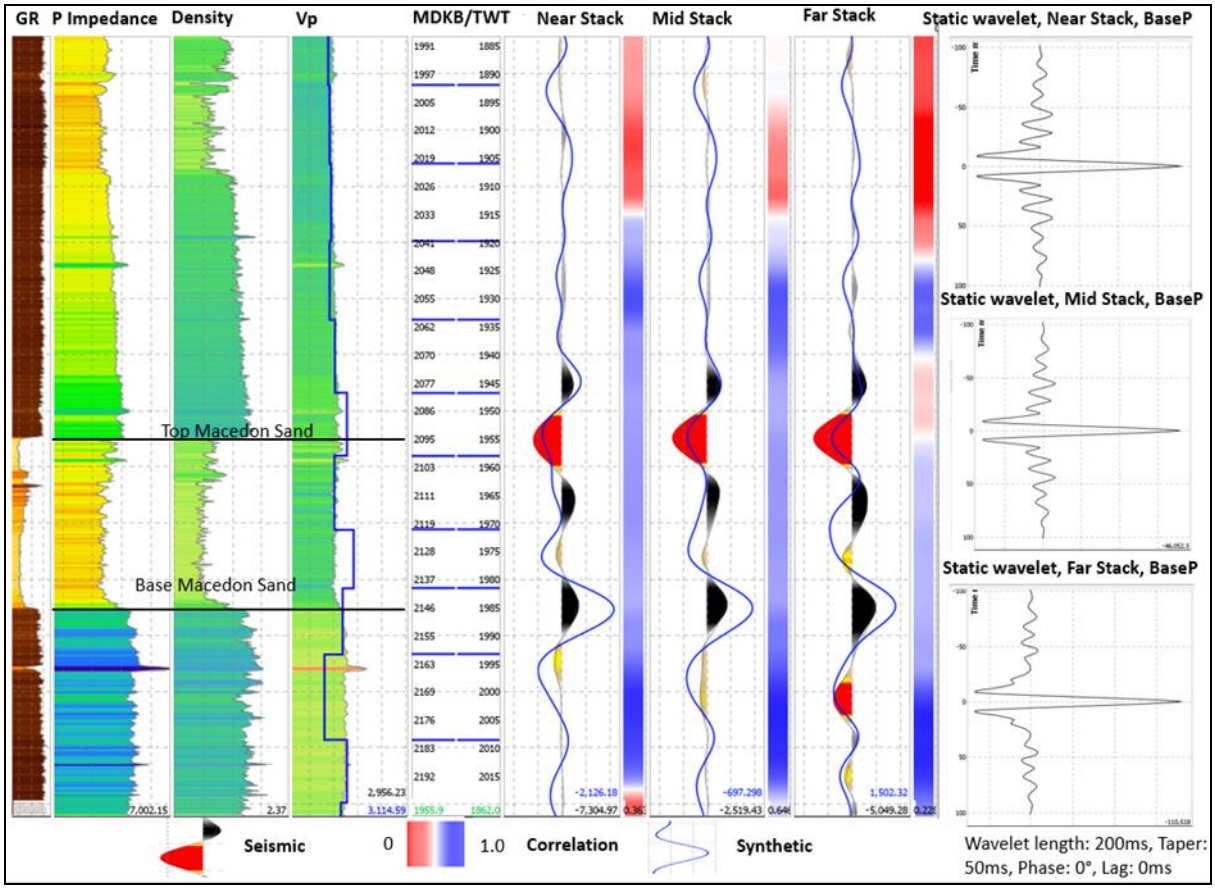

a)

Appendix B

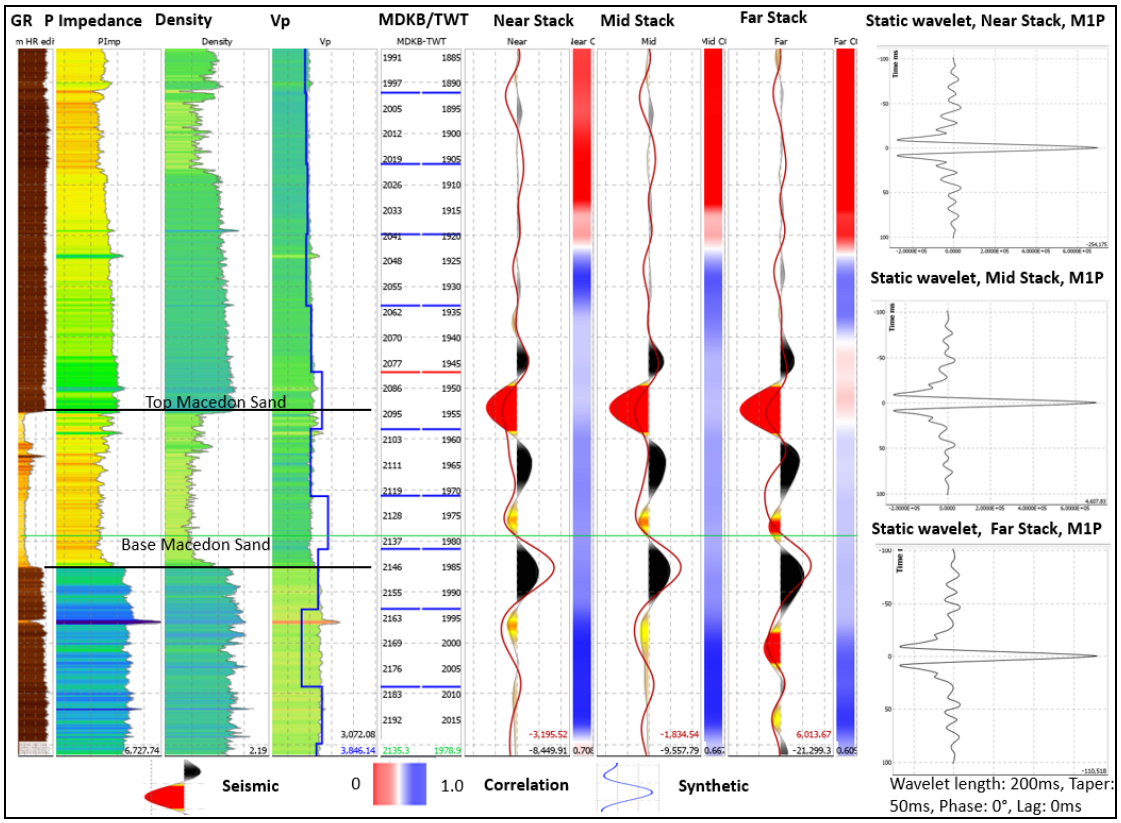
GR
P Impedance
Density
Vp
MDKB/TWT
Near Stack
Mid Stack
Far Stack
Static wavelet, Near Stack, M1P
Static wavelet, Mid Stack, M1P
Static wavelet, Far Stack, M1P
Top Macedon Sand
Base Macedon Sand
Seismic
Correlation
Synthetic
Wavelet length: 200ms, Taper: 50ms, Phase: 0°, Lag: 0ms

b)

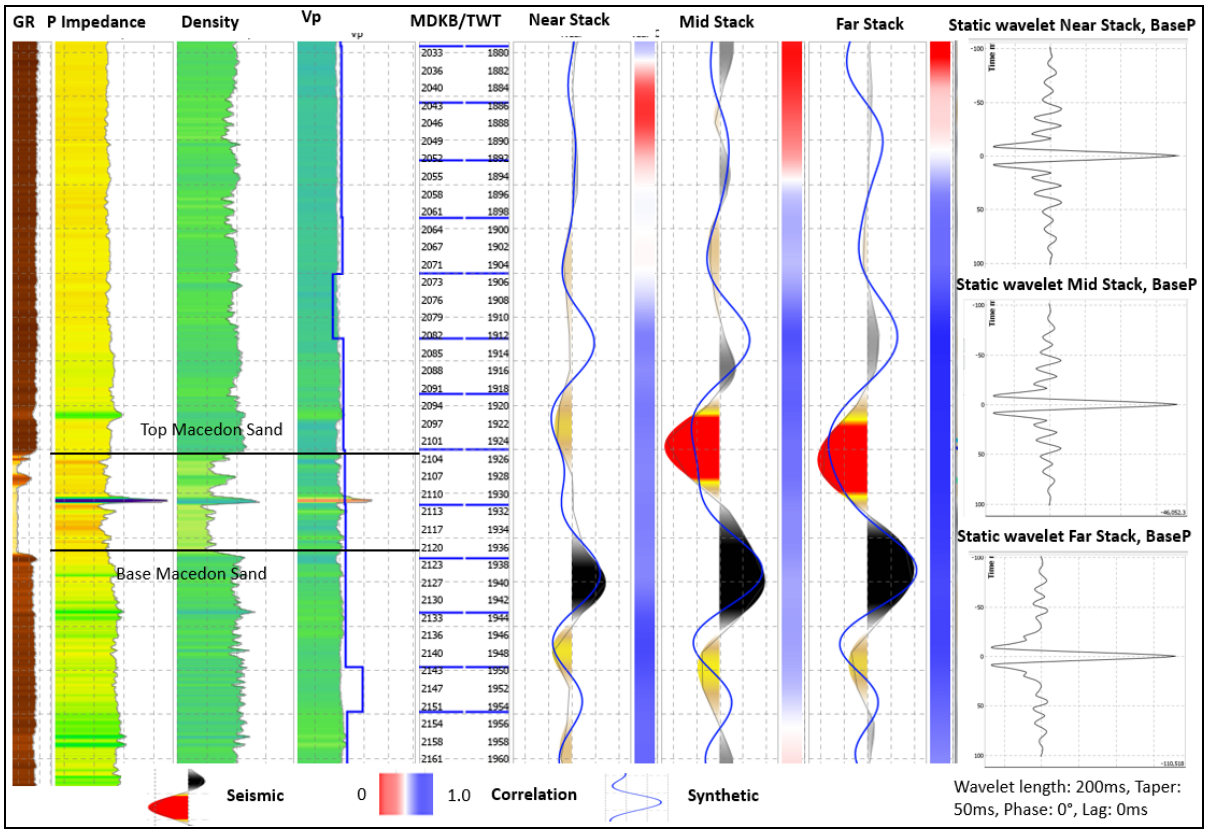
GR
P Impedance
Density
Vp
MDKB/TWT
Near Stack
Mid Stack
Far Stack
Static wavelet Near Stack, BaseP
Static wavelet Mid Stack, BaseP
Static wavelet Far Stack, BaseP
Top Macedon Sand
Base Macedon Sand
Seismic
0
1.0
Correlation
Synthetic
Wavelet length: 200ms, Taper: 50ms, Phase: 0°, Lag: 0ms

c)

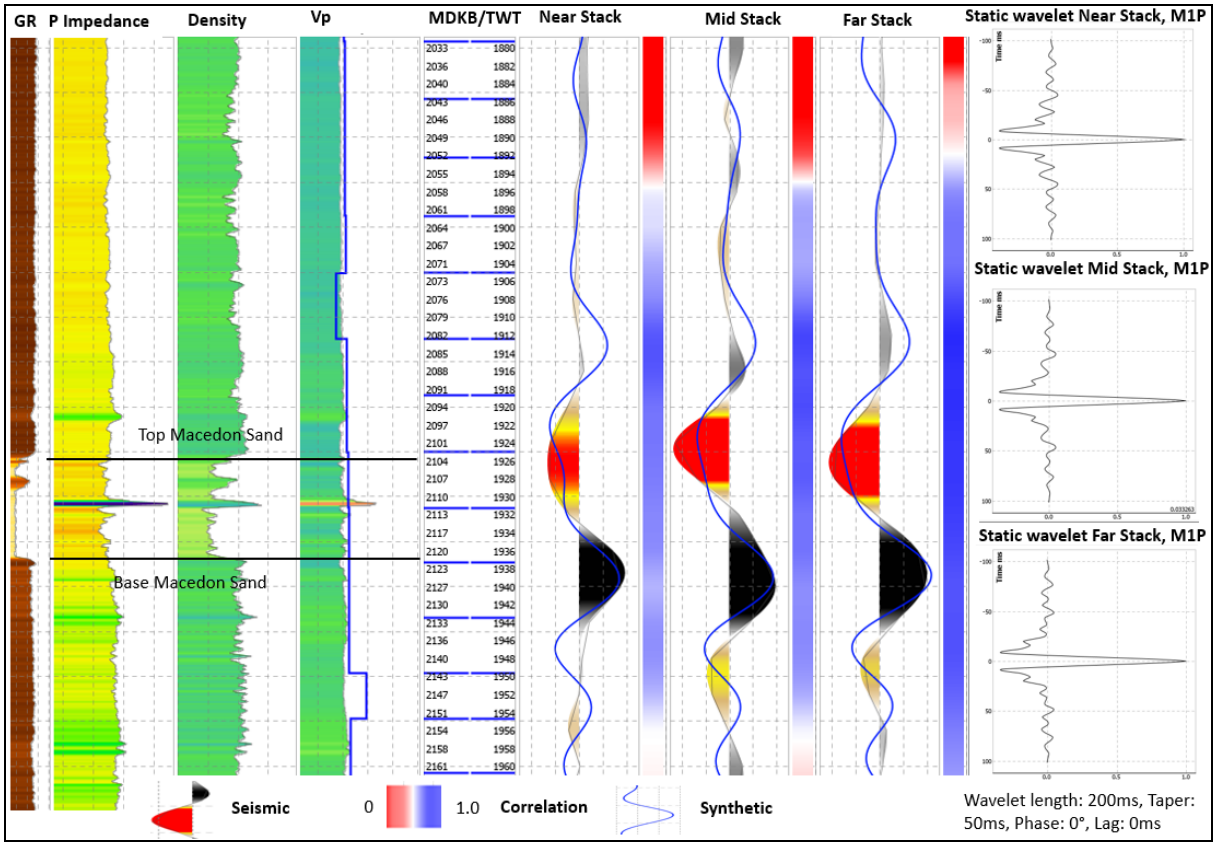

d)

Figure 49. Well tie for a) Enfield-3 BaseP survey, b) Enfield-3 M1P survey, c) Enfield-4 BaseP survey, d) Enfield-4 M1P survey.

Appendix B

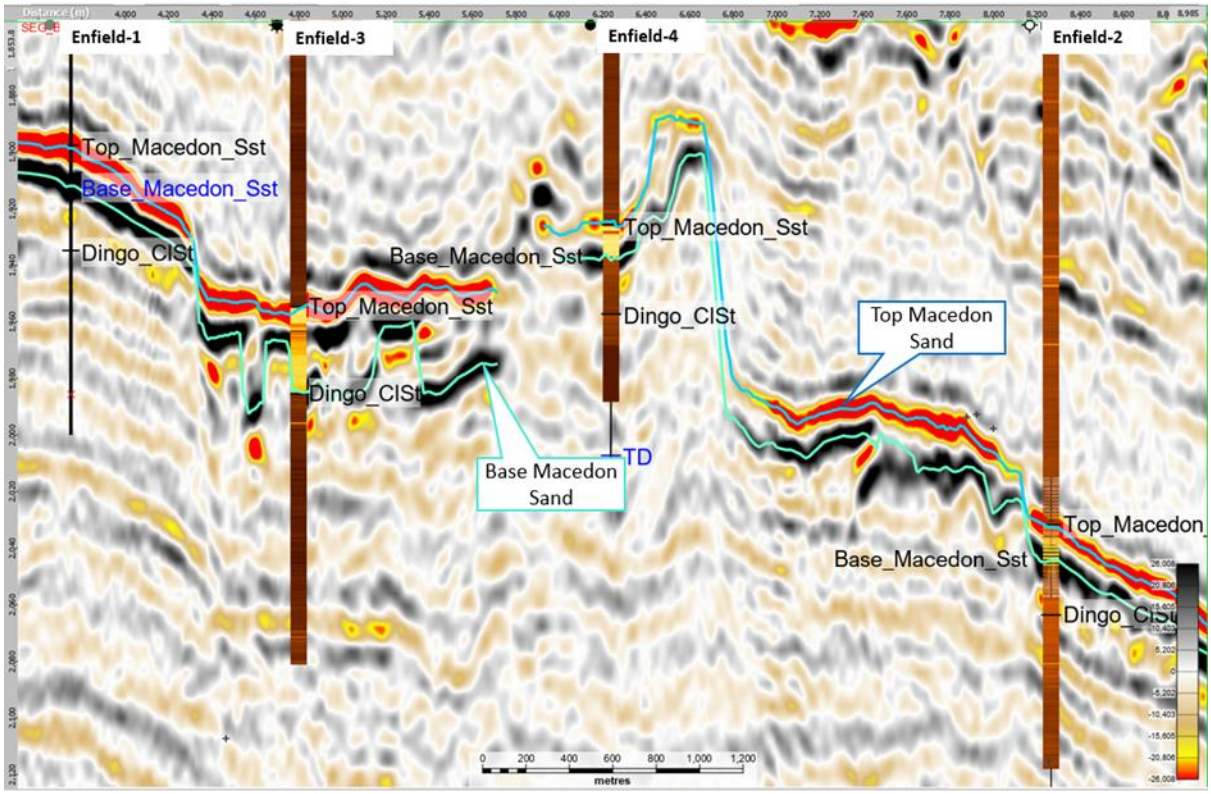

a)

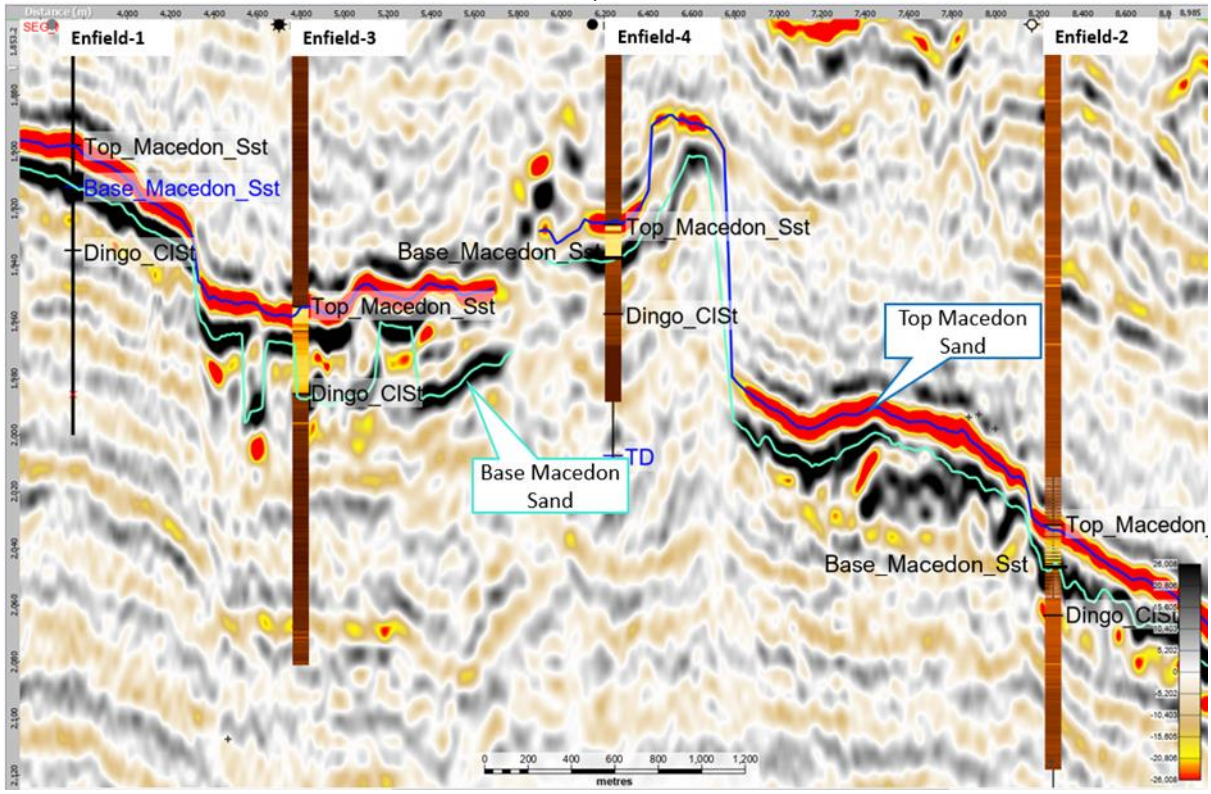

b)

Figure 50. TWT seismic Full Stack volume tie to the wells: a) BaseP survey and b) M1P survey.

Gamma Ray logs are shown as a colour.

B 1.4 Velocity quality control

Figure 51 presents the converted-to-depth volume BaseP using interval velocity originally processed by PGS and used in the thesis project. The discrepancy between the well tops and interpreted from the depth volume horizons is +1m for Enfield-1, 0m for Enfield-2 , 0m for Enfield-3 and -6m for Enfield-4. The RMS=3.0m error for the wells indicates a good-quality velocity volume.

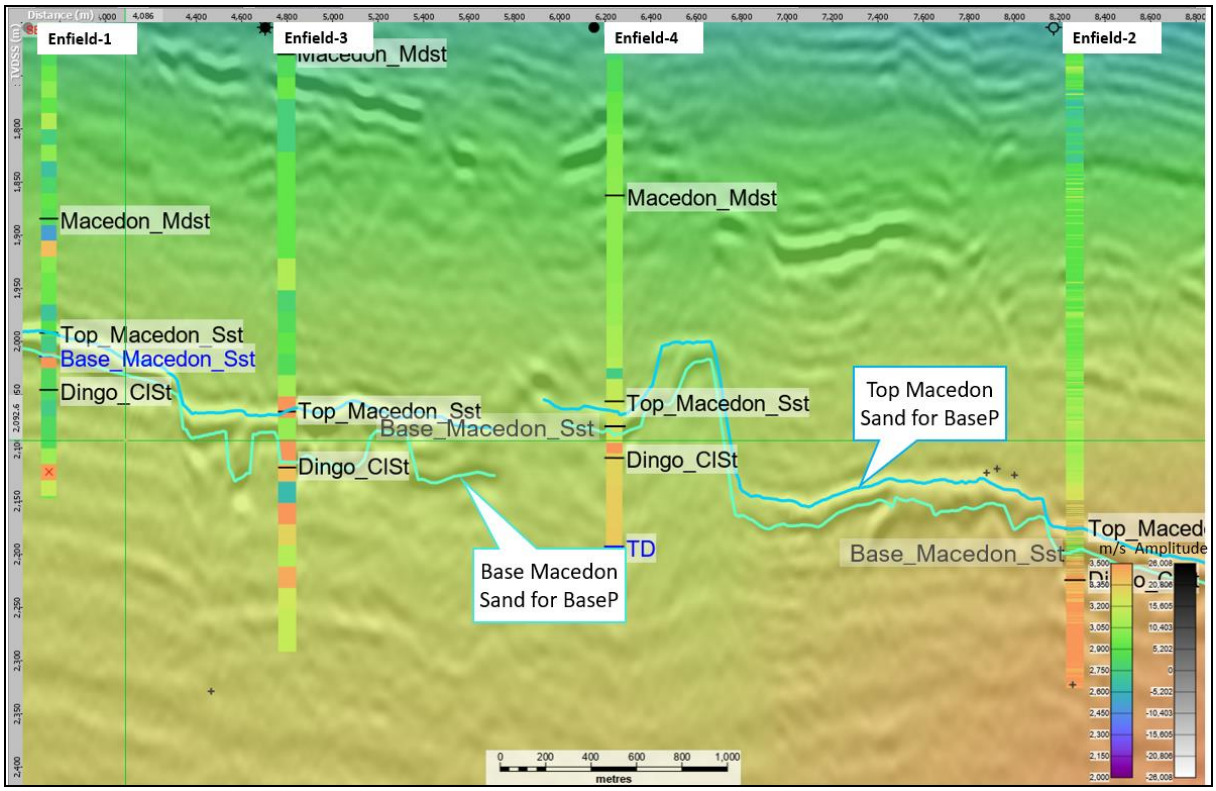

a)

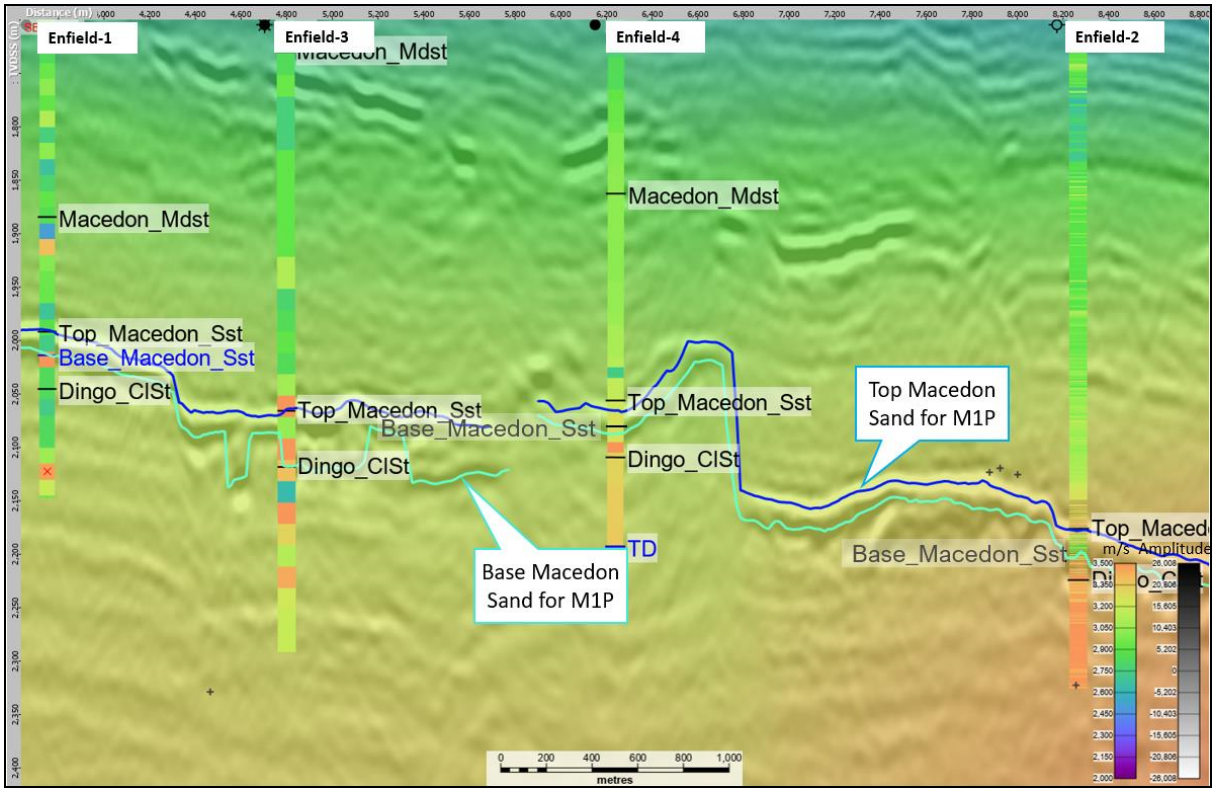

b)

Figure 51. Interval velocity volume processed by PGS contractor used in the project over-imposed on Full stack seismic volume: a) Full stack BaseP depth converted volume (TVDSS) (m). b) Full stack M1P depth converted volume (TVDSS) (m). “On the fly” option within DUG Insight was used for time-to-depth conversion. Interval velocity logs for the wells are displayed as the colour the same colour scale as the velocity volumes.

B 1.5 Seabed channels

The seabed channels are commonly present in the Exmouth Sub-basin. These channels can cause problems with seismic imaging by generating intra-bed multiples. The Enfield survey has one significant channel, positioned under the gas cap and does not affect the area of interest used in the thesis (Figure 52). PGS applied Surface Related Multiple Elimination (SRME) method for each sail line to eliminate the multiples in the data (Wickham et al., 2008).

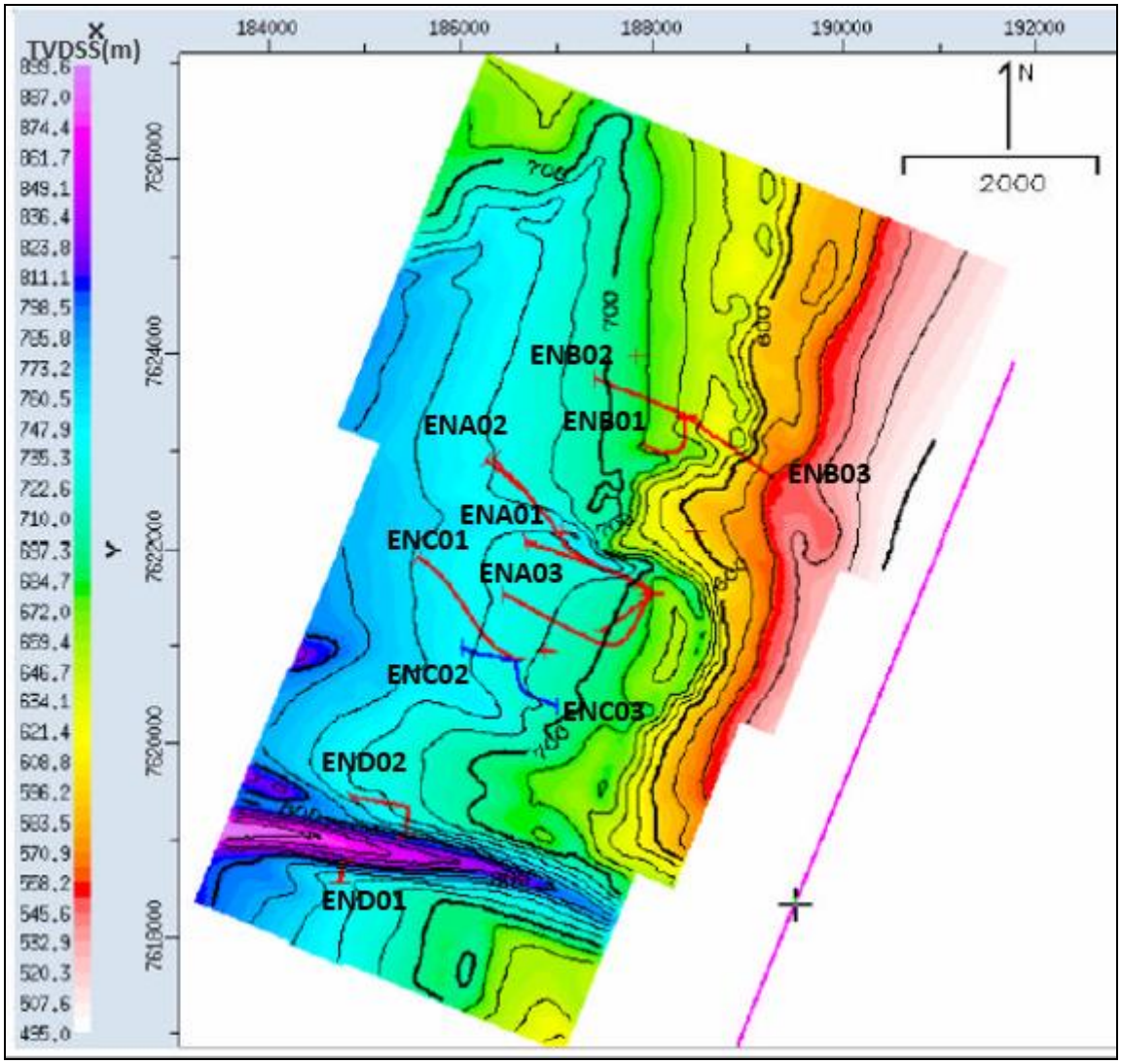

Figure 52. Seafloor (Water bottom) time structure map (modified from McFadzean, 2006).

B 1.6 Residual Move Out (RMO) processing

The inaccuracy in picking the velocities or residual anisotropic effects (Simms and Bacon, 2014) can cause the corrected gathers not being flat. In this case, the calculation of AVO gradient can be erroneous. The QC shows that finally processed gathers are not perfectly flat (Figure 53a and Figure 54a). I applied RMO correction in order to improve the gathers (Figure 53b and Figure 54b).

A non-parabolic function was used in processing RMO using DUG processing software with the following parameters: Window length – 100 ms, Range of gamma - 0.95-1.05,

Minimum pick spacing – 15 ms, Minimum semblance – 0.75, Stop threshold – 75%, Maximum shift – 6 ms, Minimum event length – 50%, Offset smoothing radios – 0 m, using pick interval as Positive and Negative Events.

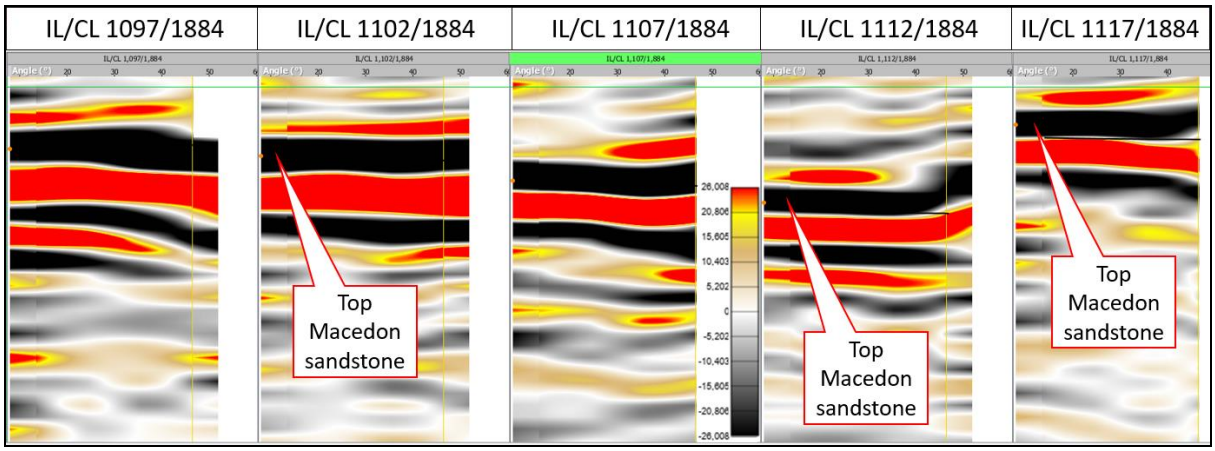

a)

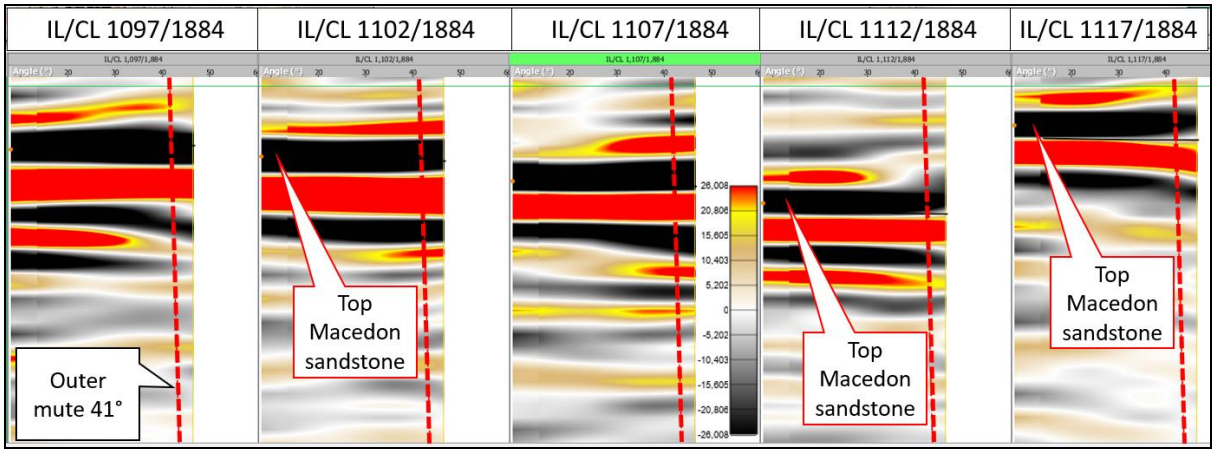

b)

Figure 53. a) BaseP angle gathers volume before RMO correction. b) BaseP angle gathers volume after RMO correction.

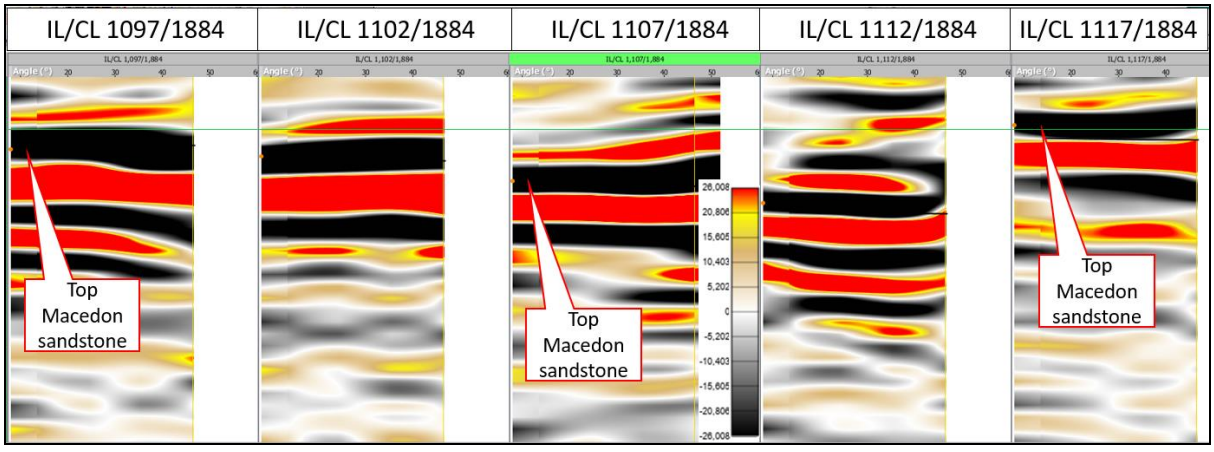

a)

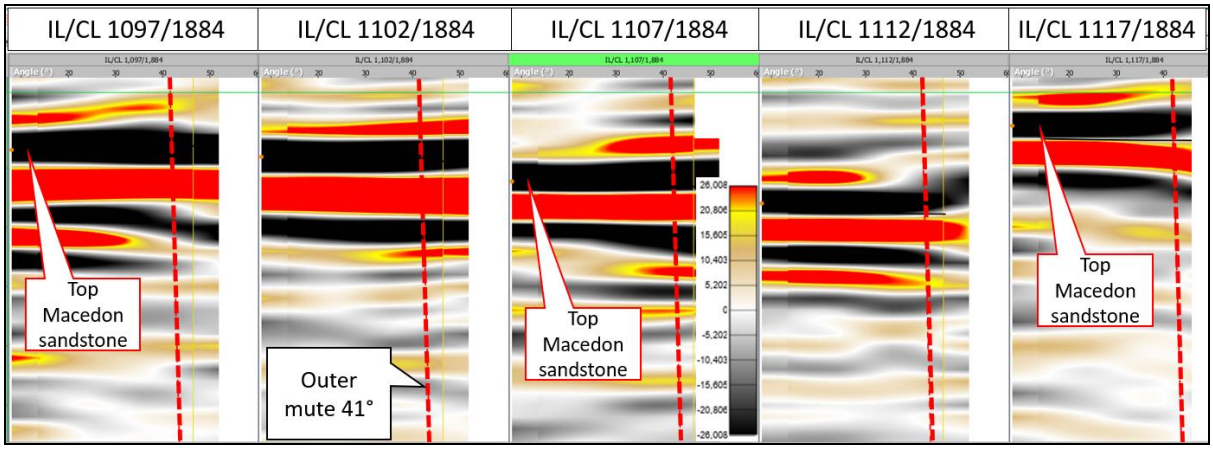

b)

Figure 54. a) M1P angle gathers volume before RMO correction. b) M1P angle gathers volume after RMO correction.

B 1.7 Normalised Root Mean Square (NRMS) analyses

The reliability of seismic volumes to be used for time-lapse studies can be assessed by measuring the repeatability as a normalised root mean square (NRMS) (Kragh and Christie, 2001, Kragh and Christie, 2002, Eiken et al., 2003).

$$NRMS = \frac{200(RMS(M1P - BaseP))}{RMS(M1P + BaseP)},$$

where $RMS(M1P - BaseP)$ is root mean square of the difference between Monitor and Base survey volumes, and $RMS(M1P + BaseP)$ is the root mean square of the sum of Monitor and Base survey volumes.

To avoid the "collapsed" reservoir effect discussed later in the text, NRMS was calculated for the interval: Ghost -700 ms from Top Macedon Sand to Top Macedon Sand within the area of the polygon A (Figure 21). The results shown in Figure 55, Figure 57 and Figure 8.

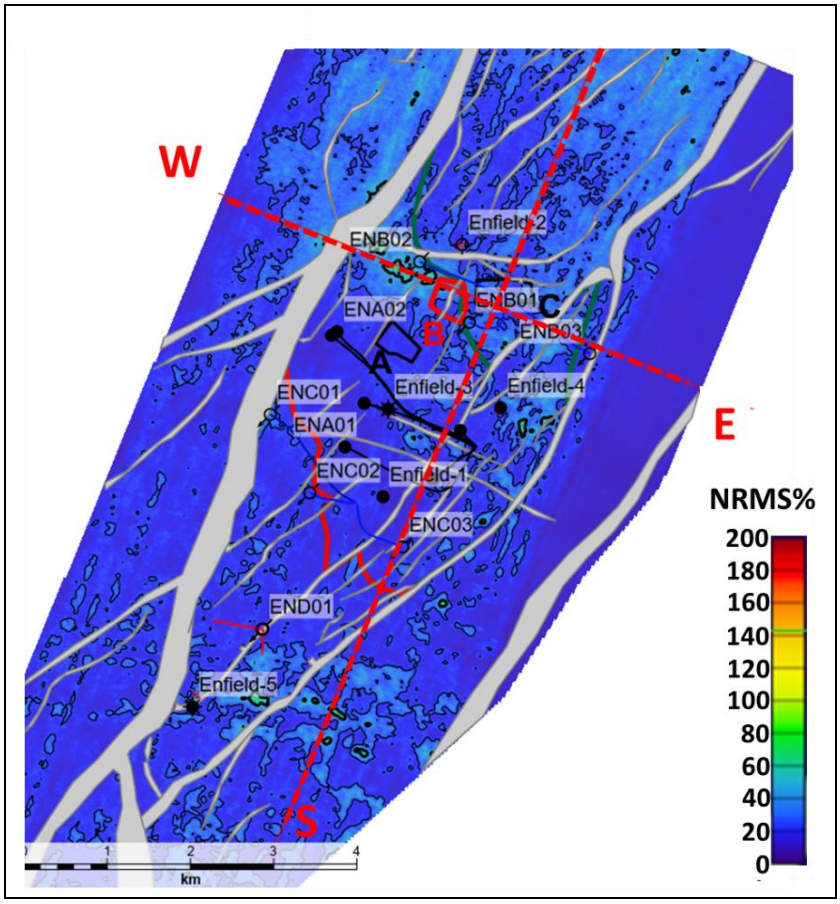

Figure 55. NRMS map for the time-lapse difference for Full stack volumes (M1P − BaseP). Contour interval is 25%, highlighted contour is 50%. Note elevated NRMS values around ENB02 and ENB01 water injector well caused by "collapsed" reservoir therefore phase shift for M1P volume (Fig. 21).

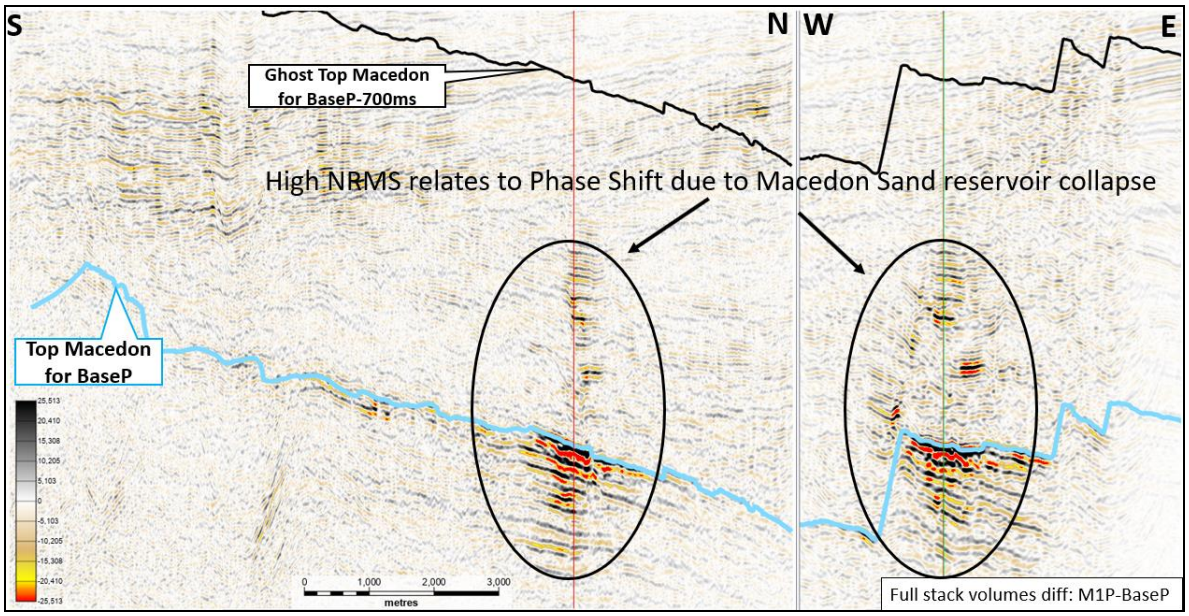

Figure 56. Seismic section of difference for Full stack volumes (M1P-BaseP). Projections of the S−N and W−E sections are shown in Figure 55.

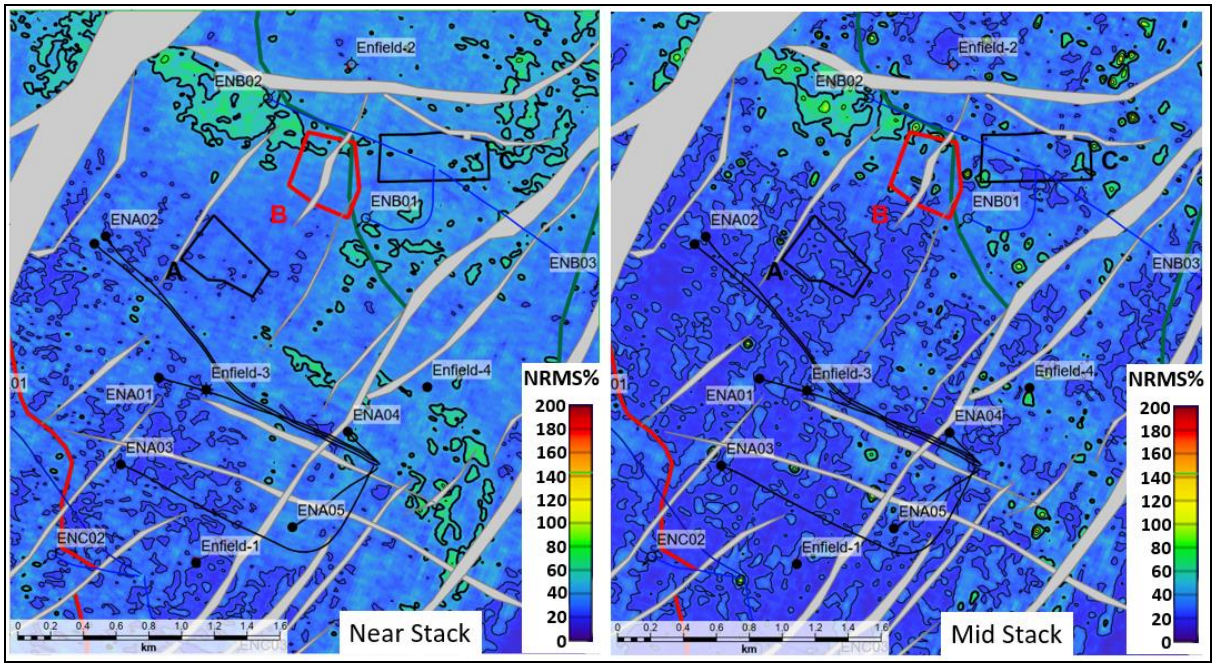
Enfield-2
ENB02
ENB01
ENB03
ENA02
ENA01
ENA03
ENA04
ENA05
ENC02
Enfield-1
Enfield-3
Enfield-4
A
B
C
NRMS%
200
180
160
140
120
100
80
60
40
20
0
Near Stack
Mid Stack
km

a) b)

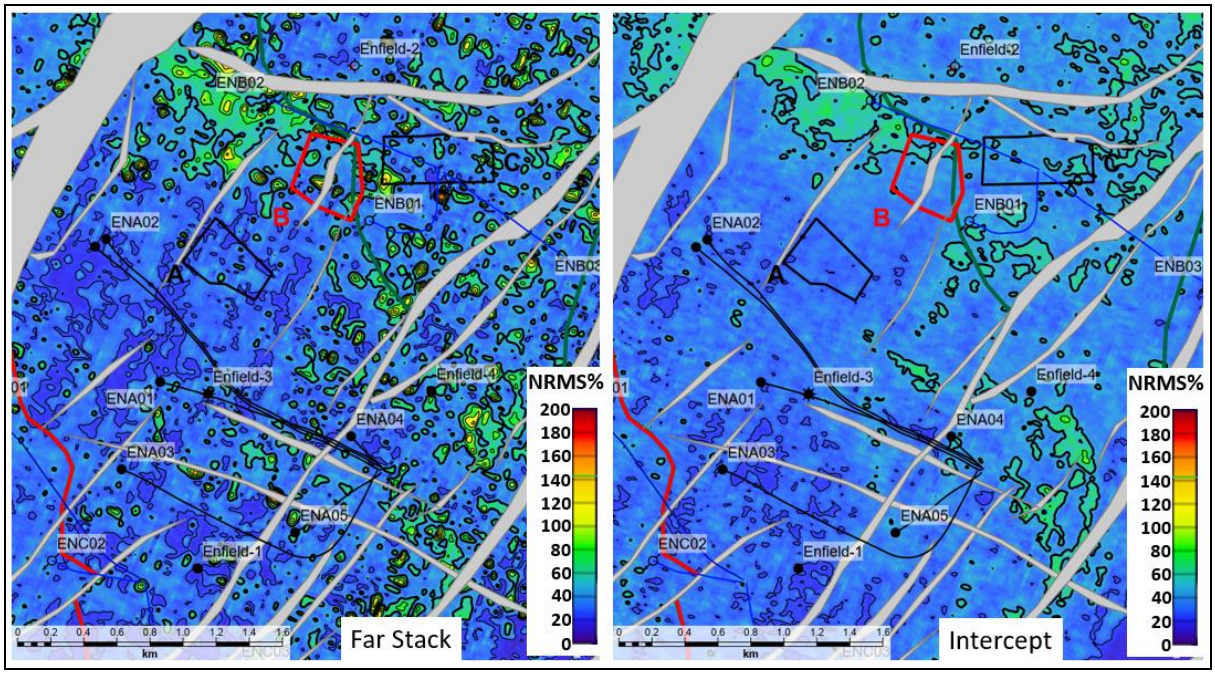
Enfield-2
ENB02
ENB01
ENB03
ENA02
ENA01
ENA03
ENA04
ENA05
ENC02
Enfield-1
Enfield-3
Enfield-4
A
B
C
NRMS%
200
180
160
140
120
100
80
60
40
20
0
Far Stack
Intercept
km

c) d)

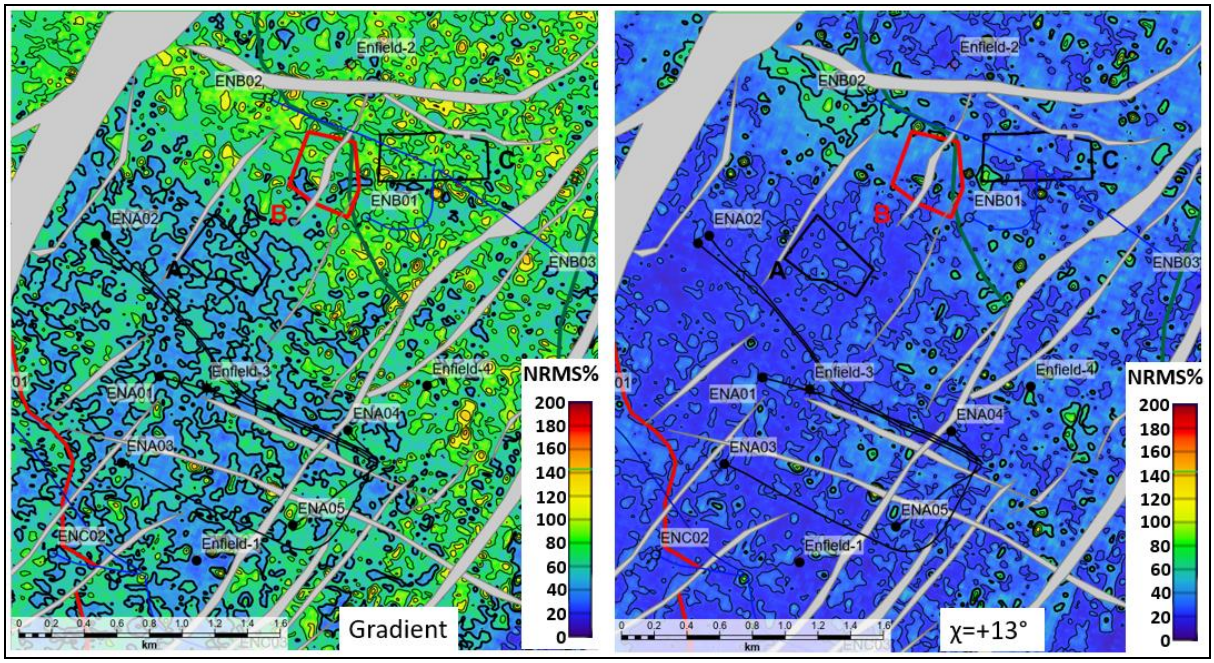
Enfield-2
ENB02
ENB01
ENB03
ENA02
A
B
C
Enfield-3
Enfield-4
ENA01
ENA04
ENA03
ENA05
ENC02
Enfield-1
NRMS%
200
180
160
140
120
100
80
60
40
20
0
Gradient
χ=+13°
km

e) f)

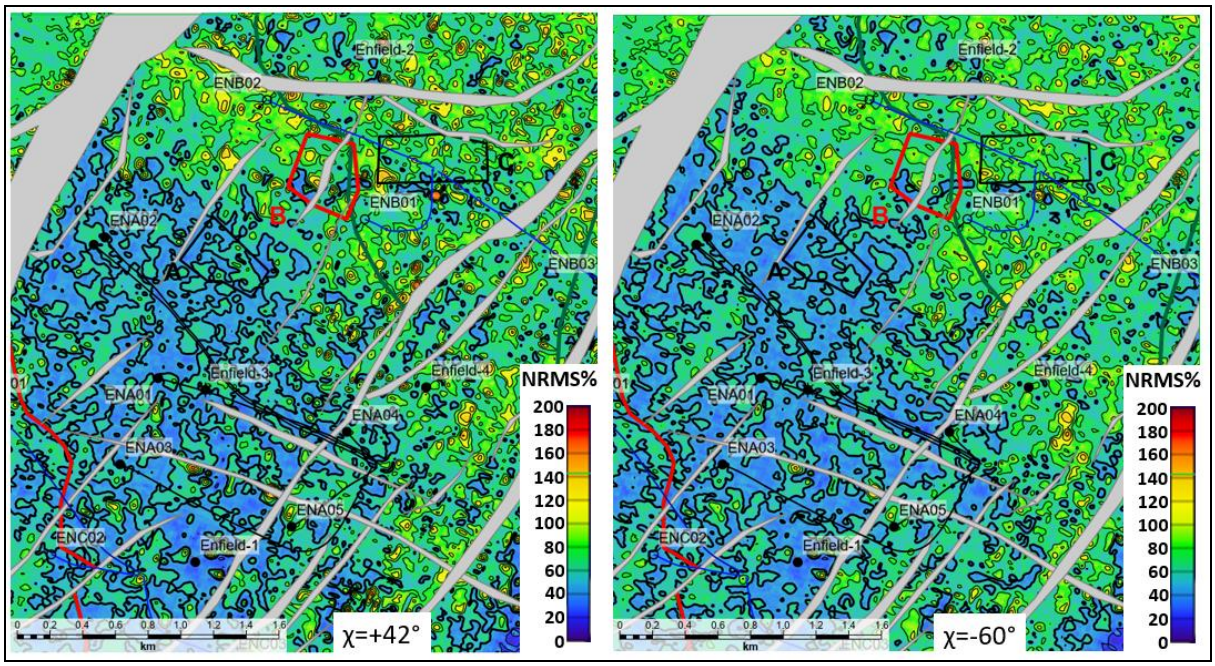
Enfield-2
ENB02
ENB01
ENB03
ENA02
A
B
C
Enfield-3
Enfield-4
ENA01
ENA04
ENA03
ENA05
ENC02
Enfield-1
NRMS%
200
180
160
140
120
100
80
60
40
20
0
χ=+42°
χ=-60°
km

g) h)

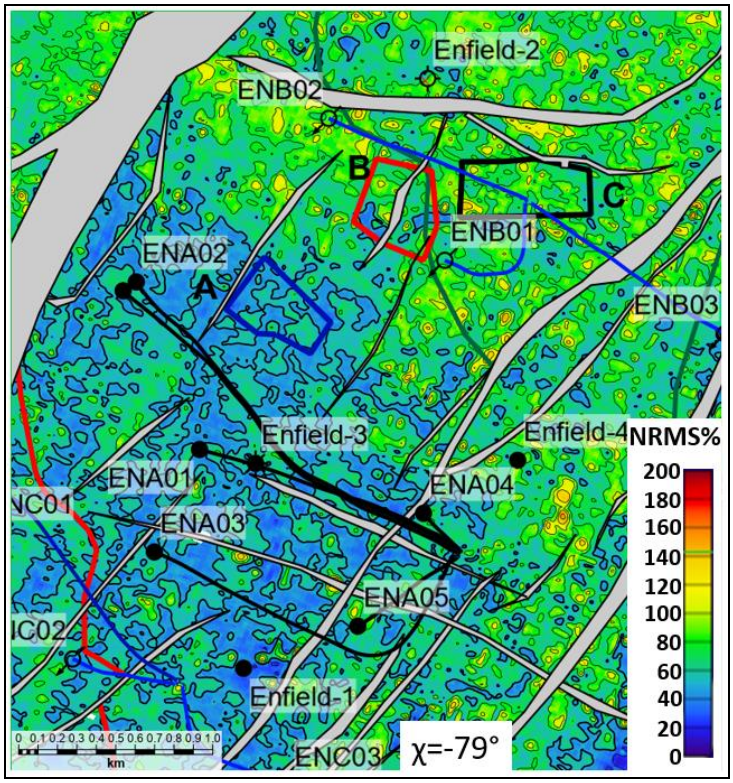

i)

Figure 57. NRMS maps for the time-lapse difference volumes (M1P − BaseP): a) Near stack, b) Mid stack, c) Far stack, d) Intercept, Gradient Intercept/Gradient rotated to f) χ=+13°, g) χ=+42°, h) χ=-60° and i) χ=-79° with the results shown in Figure 8 of the main text body. Contour interval is 25%, highlighted contour is 50% for all Figures 57a-57i.

B.2 Modelling

Given the seismic data used in the thesis were not of excellent quality and some information was not available, I used modelling to simulate conditions of the reservoir for assessment of some issues that may affect the quality of the final results. One of the main issues is relatively excessive noise in the repeatability of BaseP and M1P seismic volumes rotated to χ=+42° and χ=-79° with NRMS=50%, which I used for saturation and pressure determination respectively. Several scenarios of pressure and saturation changes with introduced noise were simulated to observe the detectability of pressure and saturation changes. The thin-bed reservoir tuning and leakage between saturation and pressure predictions were also modelled and assessed quantitatively. The fluid substitution modelling was performed for QC purposes using publicly available data. Some aspects of the potential changes to the overburden due to changes in the reservoir were also investigated.

B 2.1 Synthetic modelling approach for evaluation of noise and thin-bed effects

The partial Near, Mid and Far stacks, as well as small angle, rotated volume for χ=+13° has low NRMS from 10% to 30% are typical for repeated datasets of good quality (Kragh and Christie, 2001, Kragh and Christie, 2002, Eiken et al., 2003). The effects of relatively high noise (NRMS values) for large χ angle rotated volumes for χ=+42° and χ=-79° calculated for 4D Enfield seismic survey were assessed as quality control by performing seismic synthetic modelling. These rotated volumes were used in calculations of pressure and saturation change and it was important to evaluate how noise may affect the results. Although my quantitative interpretation was purposely conducted within the areas of a thick reservoir (Polygons A, B and C), I modelled and assessed for quality control the reservoir thin-bed effects that present within some parts of the field (Figure 44).

Kragh and Kristie (2001) also noted that NRMS measurements alone do not provide a full assessment of data repeatability. Additionally, the 50% NRMS value look like a large value although the maximum of NRMS values NRMS is 200%. The assessment of the effect of noise was also done by measuring the change in the modelled signal amplitude to the original signal using the RMS formula.

The effect of modelled noise, for χ=+42° and χ=-79° time-lapse seismic volumes 50% and 48% respectively were simulated separately for pressure and saturation changes. The commercial software RokDoc, 2022.3 (Ikon Science) was used for simulating models, making use of their standard Gassmann fluid-substitution algorithm. A 2D module within RokDoc was used with the arbitrary 2D line chosen to go through the Enfield-3 well and the polygons A, B and C (Figure 6) where qualitative interpretation was performed in the project and was not affected by thin-bed effects. The interpreted top and base horizons of the Macedon Sand reservoir were imported into the RokDoc module (Figure 61). The logs DTC, DTS, Density from the Enfield-3 well, known porosity, and lithology were used for simulating the rock physics properties of the reservoir and seal. The required synthetic models with values of NRMS 50% were generated by iterations of the RokDoc's parameter Noise Standard Deviation introduced values of the V_P, V_S, Rho and GR logs, to achieve the required NRMS values. The software allows the user to generate the seismic synthetic as rotated Extended Elastic impedance volumes. These volumes then were convolved with a wavelet to generate reflectivity volumes for NRMS calculation. To explore thin-bed effects, part of the horizons (traces 10-14 from the arbitrary line (Figure 61-65)) were edited manually to make the reservoir thinner. Then the synthetic models were imported into the DUG Insight for further processing. The data that was used in the modelling is summarised in Table 3 and Figure 60.

The following parameters were used for synthetic modelling:

Macedon Reservoir Sand: Quartz: 90%; Shale: 10%. Upper and below shales: Shale: 100%

Reservoir porosity: 24%

For modelling, I used a generated 65Hz Ricker wavelet from RokDoc library (Figure 59). The reservoir centre frequency was selected by extracting wavelet from BaseP intercept-gradient seismic volumes rotated to +42° and -79° for the Macedon Sand reservoir predominant time window of 1800-2400ms (Figure 58).

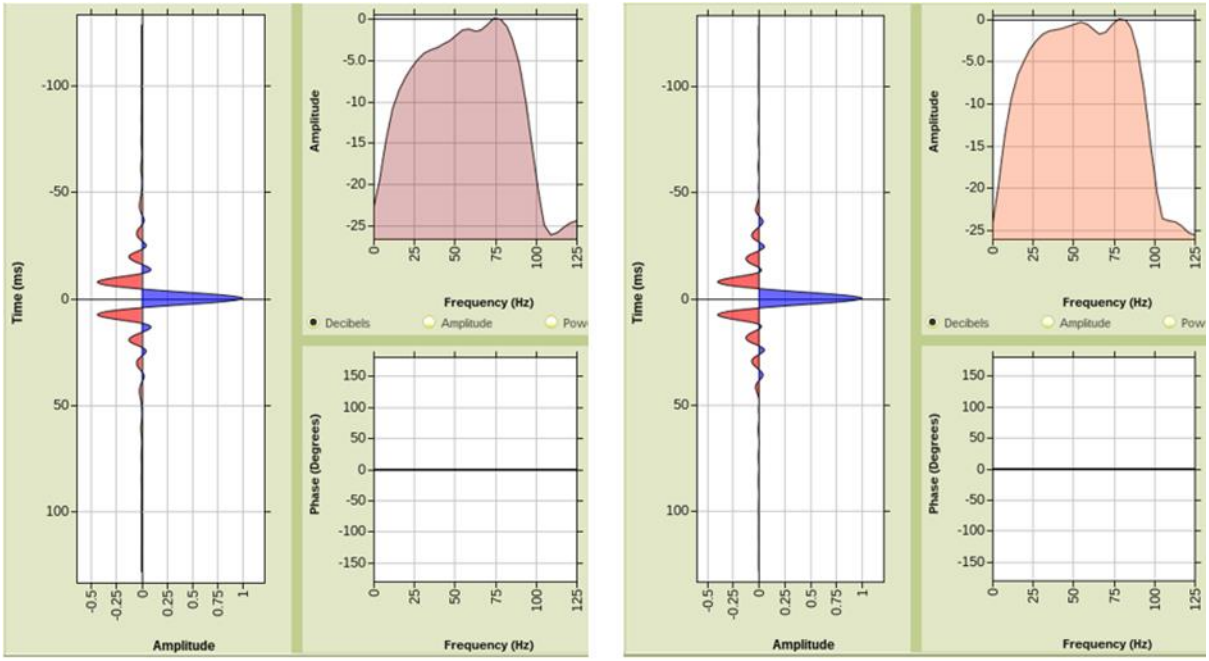

a) b)

Figure 58. Extracted statistical wavelet from BaseP intercept-gradient seismic volumes rotated to a) -79° and b) +42° for the Macedon Sand reservoir predominant time window of 1800-2400ms.

For the mineral properties I used default values from the RokDoc library (Fig.60). Fluid properties were obtained from the operator's exploration and apprises well reports (Table 3). V_P for fluids input was calculated using Batzle and Wang Models (Batzle and Wang, 1992) subroutine from Seismic Petrophysics Worksheets Version 1.7 (Pennington, 2019). The same fluid properties were used for the models with initial and increased pressures based on the results of Batzle and Wang, modelling showing a negligible change of the fluid properties with pressure (Figure 67 and Figure 68).

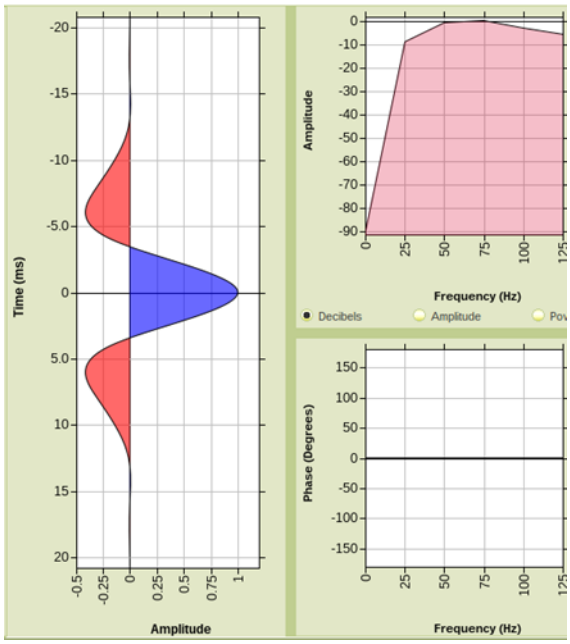

Figure 59. Ricker wavelet 65Hz was used to generate seismic reflectivity volumes.

Parameters	Value	Source
Reservoir temperature	66°C	Enfield-3 Well Completion Report (WCR) Basic Data (Willis, 2001)
Gas gravity	0.624	Enfield-4 WCR Basic Data (Willis, 2002)
GOR	248Scf/Stbbl	Enfield-4 WCR Basic Data (Willis, 2002)
Water formation salinity	38000mg/L	Enfield-4 WCR Basic Data (Willis, 2002)
Water formation density	1.025g/cc	Enfield-4 WCR Basic Data (Willis, 2002)
Oil gravity	22°API	Enfield-2 WCR Basic Data (Willis, 1999)
Oil density	0.812g/cc	Enfield-1 WCR Basic Data (Willis, 1999)

Table 3. Fluid properties were used in the synthetic models and fluid substitution modelling.

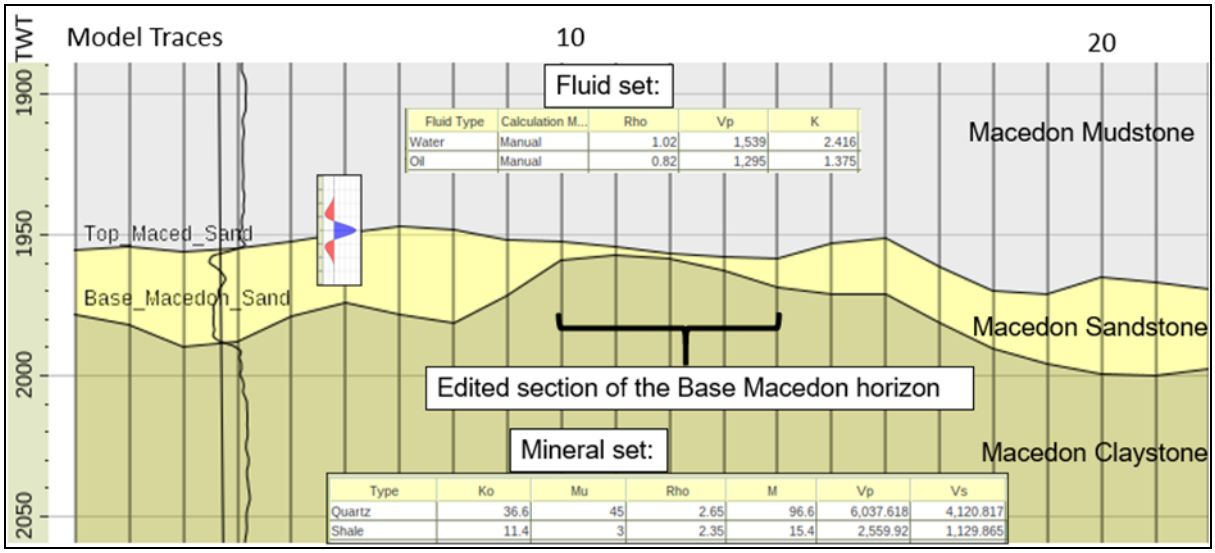

Figure 60. The cross-section of the model with rock-physics parameters were used in synthetic modelling. The used wavelet is superimposed and scaled to the model. The position of the arbitrary 2D line of the model is shown in Figure 6.

B 2.2 Effect of noise for reservoir saturation changes models

Two scenarios of saturation changes with constant reservoir pressure were explored. Scenario 1: Maximum reservoir saturation change simulated from the initial Sw=0.2 (minimum irreducible water saturation) to residual oil saturation with Sw=0.8 (maximum water saturation). This scenario simulates the condition change for time-lapse Enfield data around the injector ENB02 (Figure 20). The model in Figure 61a shows the difference of the rotated to $\chi = +42°$ seismic reflectivity for fluid substitution, Monitor (Sw=0.8) – Base (Sw=0.2) without noise. The same scenario with introduced noise NRMS=50% is shown in Figure 61b.

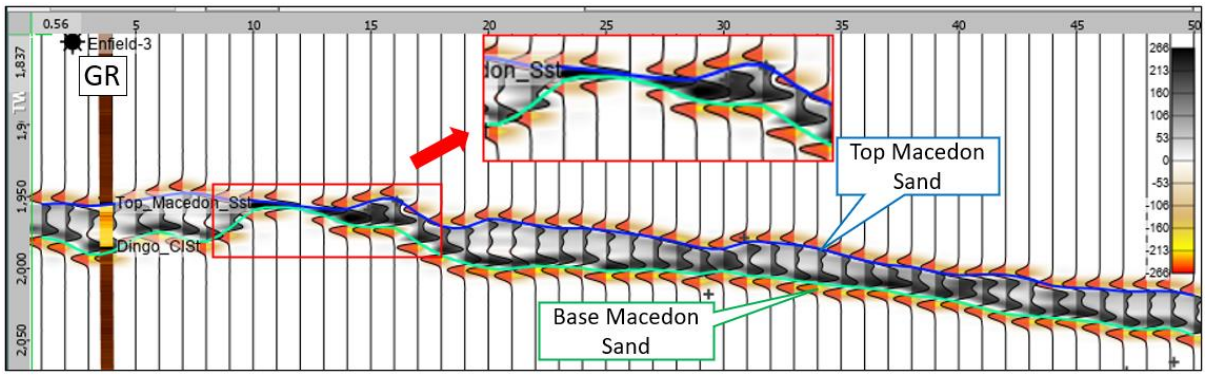

a)

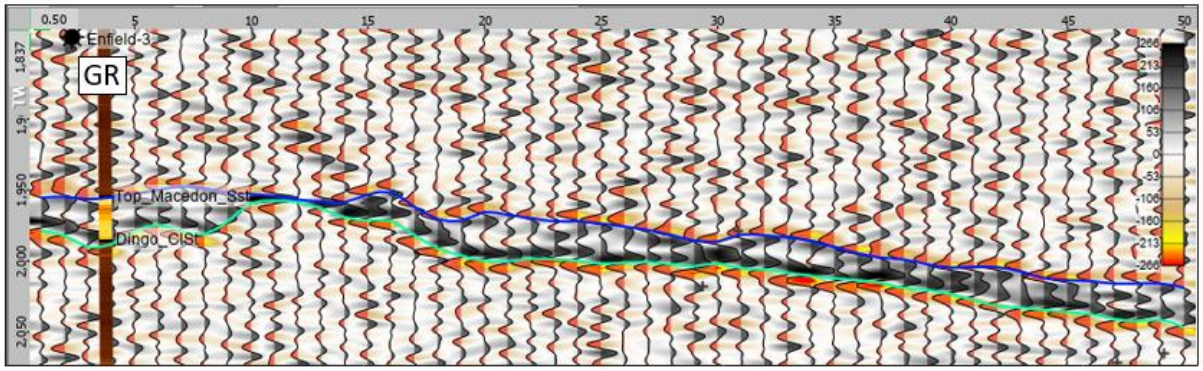

b)

Figure 61. Seismic synthetic model: a) The difference of the rotated to χ = +42° seismic reflectivity for fluid substitution, Monitor (Sw=0.8) – Base (Sw=0.2) without noise. b) The difference of the rotated to χ = +42° seismic reflectivity for fluid substitution, Monitor (Sw=0.8) – Base (Sw=0.2) with introduced noise NRMS=50%.

Scenario 2: Reservoir saturation change simulated from the initial Sw=0.2 (minimum irreducible water saturation) to Sw=0.5. This is 50% of the saturation change that had been used in scenario 1. The model in Figure 62a shows the difference Monitor (Sw=0.5) – Base Sw=0.2) without noise. The same scenario with introduced noise NRMS=50% is shown in Figure 62b.

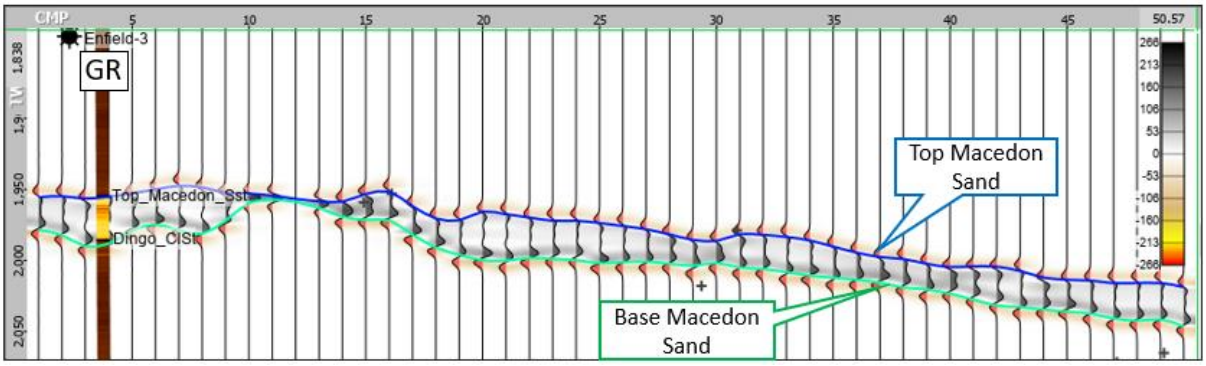

a)

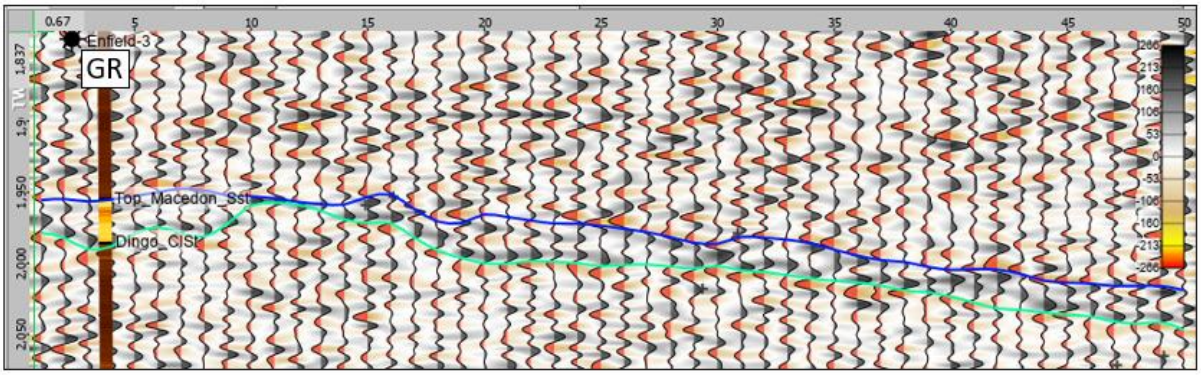

b)

Figure 62. Seismic synthetic model: a) The difference of the rotated to $\chi = +42°$ seismic reflectivity for fluid substitution, Monitor (Sw=0.5) – Base (Sw=0.2) without noise. b) The difference of the rotated to $\chi = +42°$ seismic reflectivity for fluid substitution, Monitor (Sw=0.5) – Base (Sw=0.2) with introduced noise NRMS=50%.

B 2.3 Effect of noise on reservoir (pore) pressure changes models

Pressure change has two scenarios with no change in saturation. Sw=0.2 water saturation was held constant in the reservoir layer for this modelling:

Scenario 1: Change reservoir pressure from the initial reservoir pressure at ENB01 injector of 3220psi (Depth 2000m) to 4270psi (calculated by the operator) (Figure 43). This scenario simulates the pressure change for time-lapse Enfield data around the injector ENB01 and is known as the maximum pressure difference within the reservoir. The model in Figure 63a shows the seismic reflectivity difference rotated to $\chi = -79°$ for pressure difference

Monitor (P=4270psi) – Base (P=3220psi) without noise. The same scenario with introduced noise NRMS=48% is shown in Figure 63b.

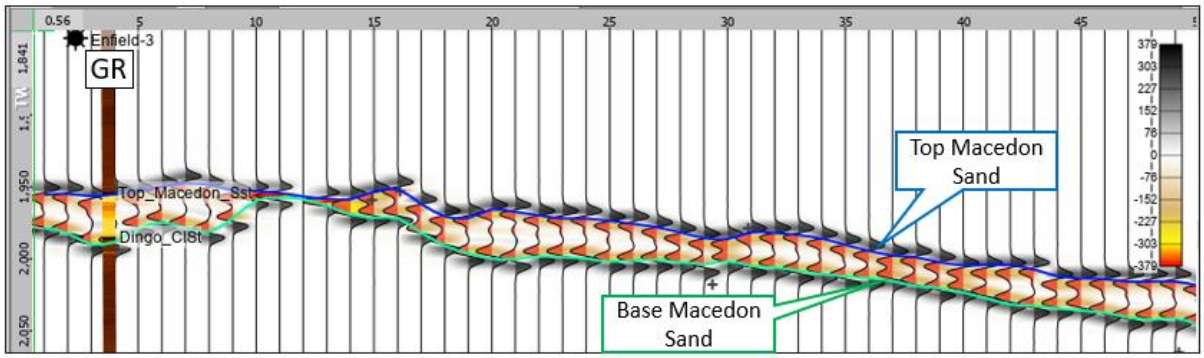

a)

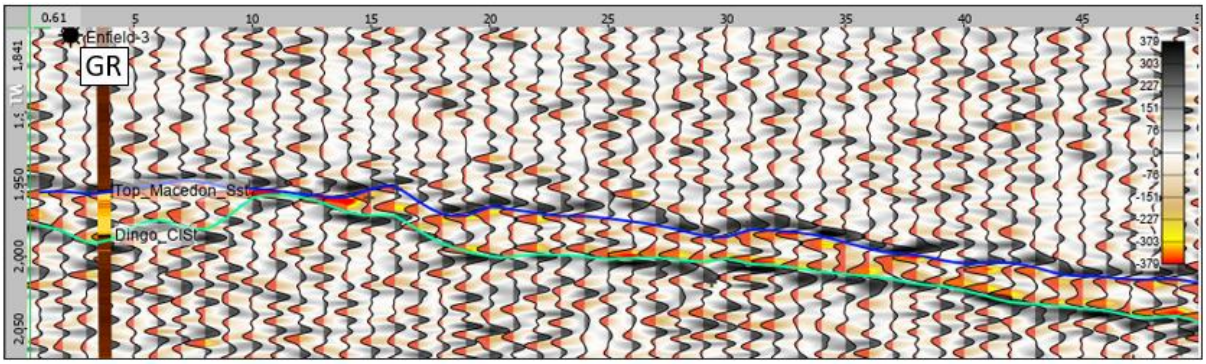

b)

Figure 63. Seismic synthetic model: a) The difference of the rotated to χ = -79° seismic reflectivity for pressure difference, Monitor (P=4270psi) – Base (3220psi) without noise. b) The difference of the rotated to χ = +79° seismic reflectivity for pressure increase, Monitor (P=4270psi) – Base (3220psi) with introduced noise NRMS=48%.

Scenario 2: Change reservoir pressure from the initial reservoir pressure at ENB01 injector of 3220psi (Depth 2000m) to 3745psi. This is the 50% of maximum pressure difference within the reservoir from scenario 1. The model in Figure 64a shows the difference Monitor (P=3745psi) – Base (P=3220psi) without noise. The same scenario with introduced noise NRMS=48% is shown in Figure 64b (Analysis of these results is given in the following section).

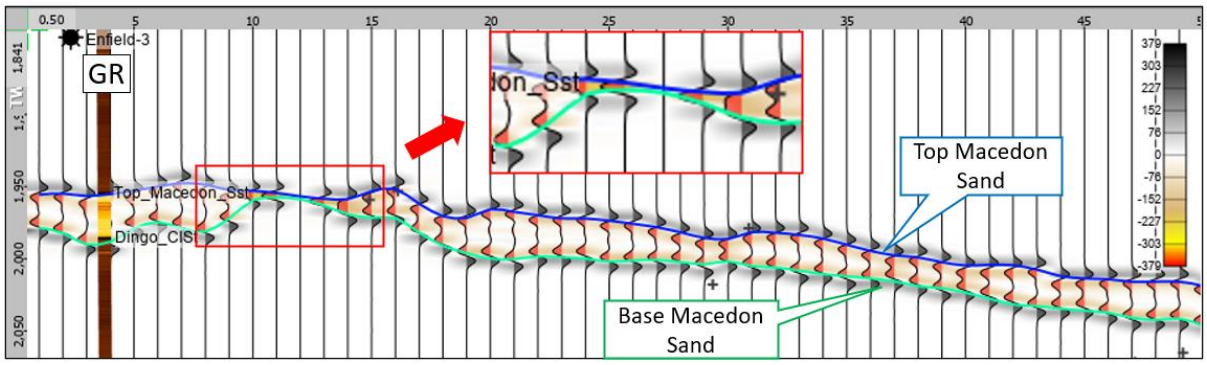

a)

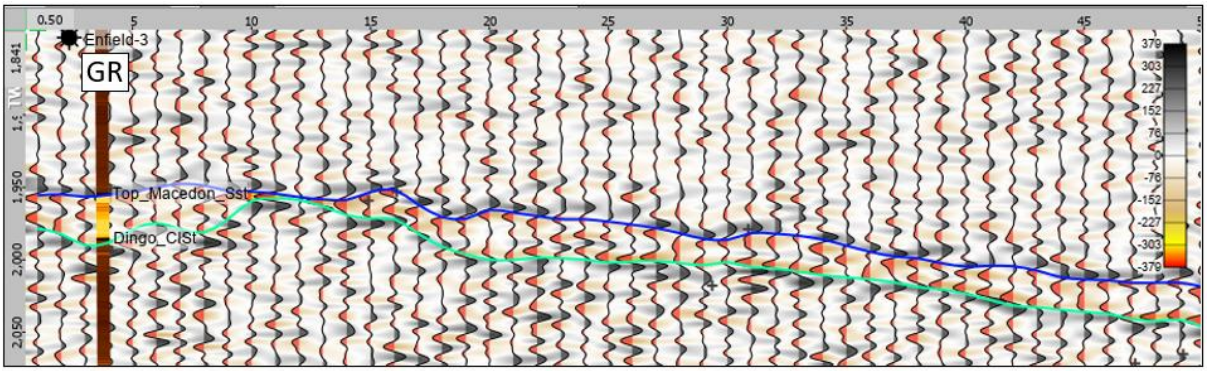

b)

Figure 64. Seismic synthetic model: a) The difference of the rotated to χ = -79° seismic reflectivity for pressure difference, Monitor (P=3745psi) – Base (P=3220psi) without noise. b) The difference of the rotated to χ = +79° seismic reflectivity for pressure increase, Monitor (P=3745psi) – Base (3220psi) with introduced noise NRMS=48%.

B 2.4 Thin-bed effects from modelling

The seismic reflectivity synthetic model for the angle of incidence θ=0° was generated using the same rock-physics and petrophysics data as for previous models using Sw=0.2 for the reservoir (Figure 65).

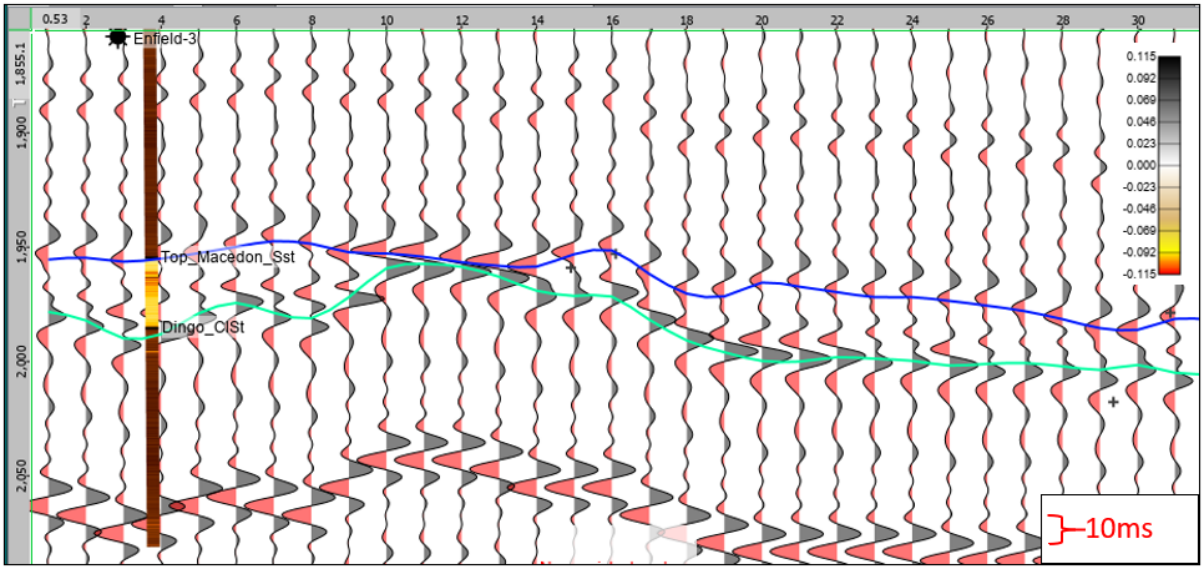

Figure 65. The seismic reflectivity synthetic model for the angle of incidence θ=0° was generated using Ricker 65Hz wavelet and the same rock-physics and petrophysics data as for previous models using Sw=0.2 for the reservoir. Note, that only 31 traces of the 2D line are shown.

B 2.5 Analyses and results from modelling

For the assessment of the noise and thin bed effects a quantitative approach was used. RMS was calculated for the amplitude change along the arbitrary modelling line within the reservoir interface for all scenarios and models that are summarised in Table 4. The amplitudes were extracted from a time window from Top Macedon to +10ms using two functions: Simple Average and Absolute Minimum/Maximum Amplitude. The Simple Average function was used in creating maps from seismic reflectivity data and Absolute Minimum/Maximum was used for inversion maps. Detailed extracted data is presented in Table 5. The values for the section of the reservoir for traces 10-14, with a thin-bed effect, were excluded from the RMS calculation. The error was calculated using the formula

$$\delta = \left(\frac{Va - \mathrm{Ve}}{Ve}\right)100\%,$$

where δ is the percent error, *Va* is RMS with no Noise value, *Ve is* RMS with Noise value.

Notably, the signal from pressure change is two times stronger than that from saturation. The most affected signal by noise due to the introduction of the noise of NRMS=50% is the saturation change for the ΔSw = 0.5-0.2 with a maximum noise of 26% and 55% for Simple Average and Absolute Minimum/Maximum, respectively. The other scenarios show a small error of 5-6% for Simple average and 16-21% for Absolute Minimum/Maximum functions. Less affected by noise is pressure change data for all the scenarios due to a strong signal from pressure.

The modelling shows that the results from seismic data with NRMS=50% are still reliable except for the saturation change data with saturation change less than ΔSw = 0.5-0.2.

The seismic amplitude increases (trace 14) and then decreases for saturation and pressure change from 10ms and less within the thin bed's zone for traces 10-14 compared with the average values (Table 5). The zoomed-in area in Figure 61a shows an amalgamation of the two peaks that increases the anomaly at 10ms thickness in the thin-bed zone for saturation change. A similar situation is observed in Figure 64a where two troughs from Top and Base interfaces of the reservoir amalgamate into one strong negative amplitude for the pressure change. This may explain the false saturation change anomaly below OWC near ENB01 in Figure 20 and described in Chapter 6.2. In this area, the isopach map shows the reservoir thickness is close to 10ms (Figure 44). The thin-bed effect is also obvious using the standard approach visually from the modelled synthetic seismic reflectivity section for the angle of incidence θ=0° for traces 10-14 (Figure 65).

Appendix B

Amplitude Extraction function	RMS ΔSw=0.5-0.2 No Noise	RMS ΔSw=0.5-0.2 NRMS=50%	Error %	RMS ΔSw=0.8-0.2 No Noise	RMS ΔSw=0.8-0.2 NRMS=50%	Error %	RMS ΔP=3745-3220psi No Noise	RMS ΔP=3745-3220psi NRMS=48%	Error %	RMS ΔP=4270-3220psi No Noise	RMS ΔP=4270-3220psi NRMS=48%	Error %
Absolute Minimum/ Maximum Amplitude	41	91	55	104	132	21	115	146	21	206	246	16
Simple Average Amplitude	23	31	26	59	62	5	58	62	6	104	110	5

Table 4. The RMS values for Simple Average and Absolute Minimum/Maximum Amplitude functions for all modelling scenarios. The values for traces 10-14 (thin-bed interval) of the section were excluded from the calculation of the RMS amplitudes.

Appendix B

	ΔSw=0.5-0.2		ΔSw=0.8-0.2		ΔP=3745-3220psi		ΔP=4270-3220psi		
	No Noise	NRMS=50%	No Noise	NRMS=50%	No Noise	NRMS=48%	No Noise	NRMS= 48%	Reservoir Thickness (ms)
RMS for thickness >10 ms	23	31	59	62	58	62	104	110	
Traces	Simple Average Amplitudes (units)				Simple Average Amplitudes(units)				
1	27	-1	67	54	-67	-58	-119	-76	23
2	22	31	57	82	-66	-66	-118	-104	27
3	15	21	38	49	-40	-29	-71	-81	34
4	20	48	50	76	-60	-81	-107	-135	33
5	21	34	53	59	-50	-93	-89	-158	26
6	18	45	47	45	-60	-63	-108	-141	24
7	22	19	56	49	-62	-24	-111	-59	31
8	16	18	40	24	-42	-16	-74	-52	33
9	28	-7	70	37	-44	-73	-79	-96	20
10	29	12	74	60	-52	-83	-92	-132	7
11	22	20	56	35	-47	-35	-84	-89	3
12	0	23	0	15	0	40	0	18	2
13	22	14	55	48	-48	-51	-85	-124	5
14	72	51	180	154	-130	-119	-233	-299	10
15	44	61	110	118	-68	-85	-122	-133	15
16	29	12	73	64	-71	-79	-127	-103	20
17	19	26	49	58	-61	-66	-109	-96	20
18	24	33	60	58	-67	-93	-120	-157	20
19	24	23	61	55	-65	-93	-115	-158	24
20	14	31	36	68	-51	-83	-91	-154	34
21	20	28	51	28	-59	-64	-105	-64	33
22	16	5	41	42	-56	-68	-99	-130	28
23	24	12	61	40	-62	-19	-112	-77	27
24	24	52	61	84	-62	-60	-111	-118	28
25	15	2	39	23	-54	-47	-96	-72	28
26	24	51	61	71	-64	-45	-115	-54	25
27	21	25	53	68	-63	-71	-113	-98	23
28	32	44	79	96	-59	-48	-106	-80	21
29	21	28	53	62	-58	-28	-103	-55	18
30	47	45	117	113	-85	-59	-153	-120	15
31	27	3	67	52	-58	-72	-104	-148	24
32	20	25	52	69	-62	-73	-111	-162	24
33	24	-21	61	48	-66	-34	-118	-122	25
34	18	63	46	93	-60	-75	-107	-151	25
35	22	49	56	76	-64	-81	-115	-121	22
36	29	24	72	70	-67	-28	-119	-39	19
37	31	42	78	95	-75	-93	-135	-142	18
38	32	-4	81	82	-70	-77	-125	-174	20
39	27	25	69	53	-65	-34	-117	-52	18
40	37	65	93	93	-59	-31	-105	-37	19
41	19	6	47	24	-42	-71	-76	-113	23
42	19	59	47	55	-45	0	-81	-54	27
43	24	25	61	53	-66	-85	-118	-165	25
44	18	-16	45	27	-41	-57	-73	-103	22
45	18	22	45	58	-58	-43	-104	-80	22
46	21	22	54	51	-63	-73	-113	-101	23
47	24	17	61	76	-63	-43	-113	-68	25
48	24	15	61	42	-64	-76	-114	-178	27
49	24	51	61	65	-63	-60	-113	-128	26
50	23	-4	57	32	-66	-123	-118	-176	28

a)

Appendix B

	ΔSw=0.5-0.2		ΔSw=0.8-0.2		ΔP=3745-3220psi		ΔP=4270-3220psi		Reservoir Thickness (ms)
	No Noise	NRMS=50%	No Noise	NRMS=50%	No Noise	NRMS=48%	No Noise	NRMS=48%	
RMS for thickness >10 ms	41	91	104	132	115	146	206	246	
Traces	Absolute Maximum Amplitudes(units)				Absolute Minimum Amplitudes(units)				
1	33	36	85	74	-121	-169	-216	-255	23
2	32	69	80	128	-122	-159	-217	-227	27
3	45	36	112	122	-102	-107	-182	-223	34
4	34	104	87	116	-128	-183	-229	-301	33
5	53	119	133	189	-117	-231	-210	-419	26
6	32	83	80	128	-122	-158	-217	-238	24
7	33	111	84	91	-125	-142	-223	-197	31
8	45	87	112	120	-102	-157	-182	-220	33
9	68	82	170	110	-124	-187	-223	-291	20
10	132	137	331	332	-231	-343	-415	-433	7
11	112	134	280	278	-238	-336	-426	-487	3
12	0	103	0	35	0	19	0	-109	2
13	110	59	277	266	-238	-275	-426	-488	5
14	113	112	281	256	-160	-189	-286	-440	10
15	73	137	180	194	-123	-158	-221	-261	15
16	37	52	93	119	-121	-203	-216	-311	20
17	33	125	84	107	-121	-175	-216	-218	20
18	33	122	84	140	-121	-145	-216	-267	20
19	32	108	80	114	-122	-154	-217	-343	24
20	34	133	87	157	-128	-188	-229	-274	34
21	34	68	87	75	-128	-135	-229	-198	33
22	33	89	84	78	-125	-136	-223	-298	28
23	32	69	80	137	-122	-135	-217	-284	27
24	32	76	80	116	-122	-118	-217	-247	28
25	33	57	84	107	-125	-119	-223	-189	28
26	32	79	80	108	-122	-110	-217	-143	25
27	33	73	85	136	-121	-167	-216	-223	23
28	58	109	145	197	-123	-116	-220	-203	21
29	36	59	90	110	-123	-103	-219	-191	18
30	81	174	200	256	-124	-152	-222	-238	15
31	53	81	133	174	-117	-115	-210	-247	24
32	33	73	85	158	-121	-126	-216	-317	24
33	32	13	80	77	-122	-85	-217	-345	25
34	32	155	80	176	-122	-212	-217	-322	25
35	33	64	85	126	-121	-184	-216	-179	22
36	41	108	101	147	-123	-61	-219	-110	19
37	72	74	179	231	-122	-170	-218	-253	18
38	45	34	112	135	-123	-136	-219	-389	20
39	40	96	98	118	-123	-168	-219	-201	18
40	73	158	180	193	-123	-138	-221	-173	19
41	58	73	145	121	-123	-162	-220	-358	23
42	53	134	133	148	-117	-57	-210	-140	27
43	32	54	80	73	-122	-148	-217	-292	25
44	58	37	145	130	-123	-144	-220	-242	22
45	33	90	84	118	-121	-105	-216	-165	22
46	33	82	85	103	-121	-152	-216	-192	23
47	32	86	80	200	-122	-213	-217	-229	25
48	32	99	80	108	-122	-140	-217	-289	27
49	32	174	80	147	-122	-201	-217	-317	26
50	32	33	80	51	-122	-193	-217	-290	28

b)

Table 5. The amplitudes were extracted using a) Simple Average Amplitude and b) Absolute Minimum/Maximum Amplitude functions for the 2D modelling line for all 50 traces. The amplitude values for traces 10-14 with a thin-bed effect (equal and less than 10ms) were excluded from RMS amplitude values for the line.

B 2.6 Insights from modelling

Synthetic modelling is important for the validation of the results and can be used to estimate quantitatively the accuracy and therefore reliability of the pressure and saturation change maps.

High NRMS (50%) noise appears to not critically affect the signal from the top reservoir interface for high-pressure changes of 525psi and 1050psi modelled for the Enfield case field scenario. The results for the saturation change of less than 50% from the maximum irreducible saturation change are not reliable due to noise and weak signal and should be used with caution.

When the reservoir is 10ms or thinner, the seismic reflectivity for the angle rotated to χ = +42° and χ = -79° used for saturation and pressure change maps respectively is strongly distorted. The modelling of the seismic reflectivity for incidence angle θ=0° confirms the thin-bed 10ms limit in using the data. About 15% of the area of research has a reservoir that was affected by this thin-bed effect. Therefore, the results within most of the area of our interest should be reliable, in particular, pressure change anomalies around the injectors ENB02, ENB03, north of ENB01, ENC01 and pressure anomaly at Sliver Block. The saturation anomaly over 50% change around injector ENB02 is the most reliable according to the modelling and not reliable around other injectors.

The critical areas for quantitative interpretation within the polygons A, B and C were prudently chosen outside of the thin-bed effect.

B 2.7 Leakage between pressure and saturation changes

The definition of “leakage” between pressure and saturation changes can be looked at in two ways.

Landro M, (1999, 2001) who was one of the first to explore the separation of pressure and saturation changes in the reservoir from time-lapse data, defined the leakage as the saturation change anomaly within the water leg (below OWC) at the same location where a strong pressure anomaly has been identified from the pressure change map. I have a similar case in my results. The strong pressure anomaly I at the ENB01 injector in Figure 19 coincides with the saturation change anomaly below OWC in Figure 20. A similar scenario is observed to the west from Enfield-2 well. These saturation changes are below OWC and can be considered as a leakage from the pressure property. We know that the reservoir thickness in these areas is close to 10ms (Figure 44). We also know from the modelling, that the likely reason for this saturation change anomaly is the thin-bed reservoir effect. In this case, we can relate the leakage to thin the bed effect or noise.

Another way to quantify the leakage is to assess the interference by one of the signals in our interpretation of the other signal, in that the pressure effect is seen in the analysis of the fluid substitution or crosstalk. Although the whole concept of the thesis is to find maximum discrimination between saturation and pressure change with minimum leakage between properties, we may expect some leakage.

As already discussed in Chapter 3.3, the saturation changes and rigidity changes must be orthogonal as long as Biot-Gassmann and the two-term approximation are both valid. My estimated angles for saturation and pressure changes are not exactly orthogonal, because we prefer to employ a data-driven (adaptive) approach where the selected angles give the best indicators for those changes. Therefore, a straightforward approach in assessing and possibly quantifying the leakage is the difference between the orthogonal angle and the difference in our angles.

One way we can estimate the leakage as an angle difference is by applying linear or periodic formulas:

1. A linear formula approach of calculating error is L linear error = |(Diff-90|/90 = 34% where Diff = 31° is the difference between two effects in degrees.

2. The periodic function can be used and defined as L periodic error (cosine) = |cosine(Diff)| = 51% using the cosine function and L periodic error (sin) = 1-|sin(Diff)| = 14% using sine.

This approach is intuitive, and all three formulas give quite different numbers. Which one is applicable and can be used in noise assessment would need special research.

Another way to estimate the leakage quantitively is by applying Landro's method and making some amendments. First, we would need the right conditions within the field: the absence of a thin-bed effect in our case. These would be polygon C where we have a maximum pressure change anomaly with an average pressure change of 1000 psi and therefore more likely area to expect the leakage. There is some observed anomalous saturation change within the polygon that was calculated as average saturation change within polygon C (Figure 20). Considering a maximum leakage of 100% with a maximum saturation change of 100% the leakage calculated in polygon as the average of change 3% is negligible. The average saturation change in polygons A and B was also calculated for comparison (Table 6).

Average movable-oil-saturation change ΔSwM calculated for the polygons A, B and C		
A	**B**	**C**
3%	10%	3%

Table 6. The average movable-oil-saturation change ΔSwM for the polygons A, B and C.

B 2.8 Reservoir overburden implications

Although the typical oil shale fracking pressure is around 8,000 psi and pressure change in Enfield reservoir is around 1000 psi, the potential changes in the overburden caused by pressure increase have been investigated. Considering the high-pressure kinematic effect on the reservoir, some effect could also be expected in the overlaying shales as well as on shales at the base of the reservoir. The breaking of the shale frame matrix would lead to a similar effect as for rock-physics changes in the reservoir and therefore would affect the interface shale/sand property. This may lead to an erroneous interpretation of the reservoir changes.

The EEI inversion volumes rotated to $\chi = -60°$ for the shear modulus were used for the interpretation of overburden potential changes. Shear modulus is not affected by fluid changes but it is greatly affected by pressure changes. This is a similar case as for pressure changes angle $\chi = -79°$, but in this instance the most sensitive to reservoir pressure change angle is irrelevant.

Figure 66 shows the time-laps difference map for inverted EEI for angle $\chi = -60°$ using amplitude extraction 10 ms above Top Macedon reservoir. The fracking and crumbling shales around injectors would cause a decrease in velocity in the overburden and as the result, negative impedance change anomalies. Instead, we have positive anomalies around injectors. The map is very similar, but with the opposite sign to the map in Figure 18h which is for EEI angle $\chi = -60°$ amplitudes extracted within the reservoir. The positive anomalies can be explained by the modelling of the pressure from Figure 63a and Figure 64a as a bed boundary effect where the peak of the EEI reflectivity over the Top Macedon Sand had an effect on inversion results. This suggests that there is no evidence of pressure effect on overburden.

The shales at the reservoir base have not been examined due to the ambiguity of the structural interpretation of the Base Macedon Sand in some parts of the field and potential errors in the velocity model due to reservoir changes.

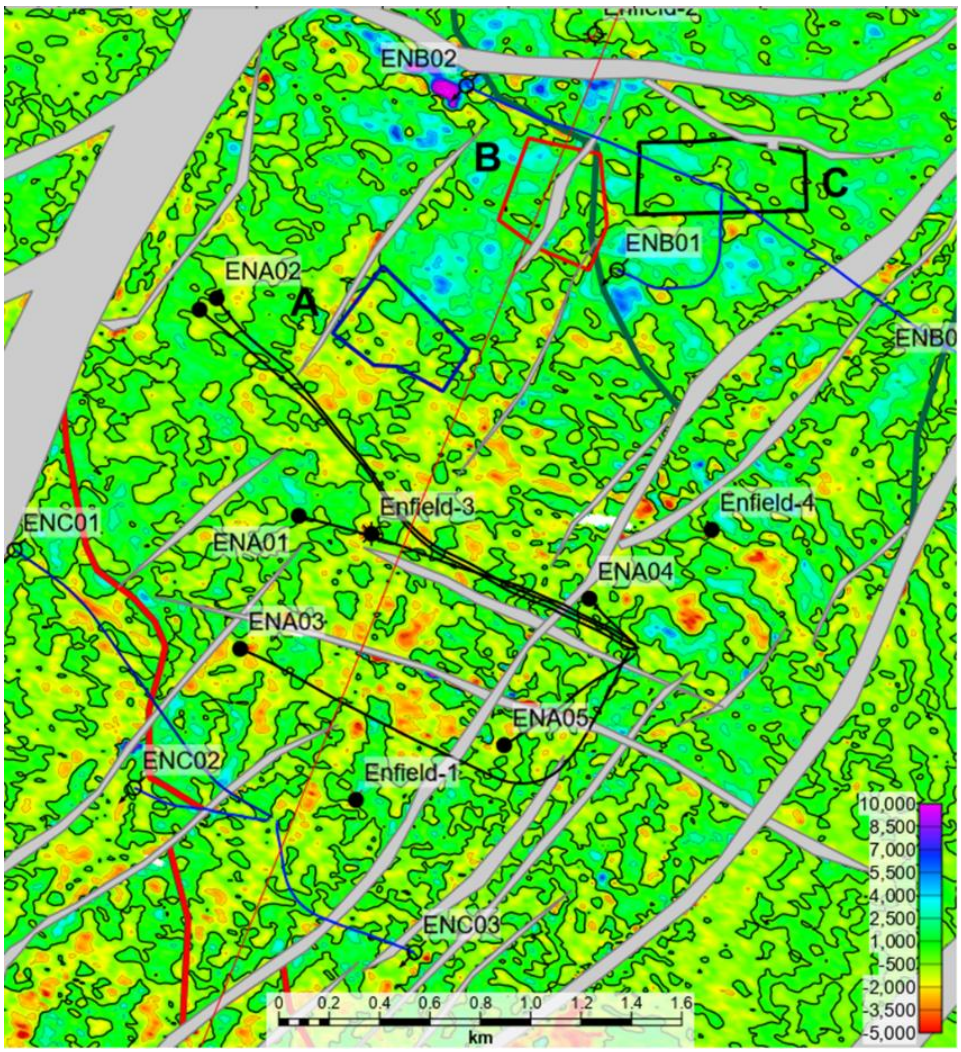

Figure 66. Inverted time-lapse difference maps for EEI angle χ=-60° showing extracted amplitudes within 10ms overburden from the Top Macedon Sand. The black highlighted contour is 0.

B 2.9 Fluid substitution modelling

For most of my project, I used the results of water substitution conducted by the operator. This decision was based on anticipation of these data being more reliable/accurate due to all information and insights into the fluid properties being available to the operator and not to the

public (Martin, 2002). I nevertheless conducted the water substitution modelling as the QC procedure using available software and publicly available data.

Figure 67a presents the results of fluid substitution modelling for Enfield-2 well conducted by the operator for 100% Gas, 100% Oil and 100% Brine scenarios. Figure 67b presents the QC modelling results using fluid properties and formation mineral parameters from Table 3 and Figure 60 used in Hampson-Russel software. The vertical and horizontal scales as well as the log's colours are the same for both Figures 67a and 67b. The modelling results are identical for both Figure 67a and Figure 67b.

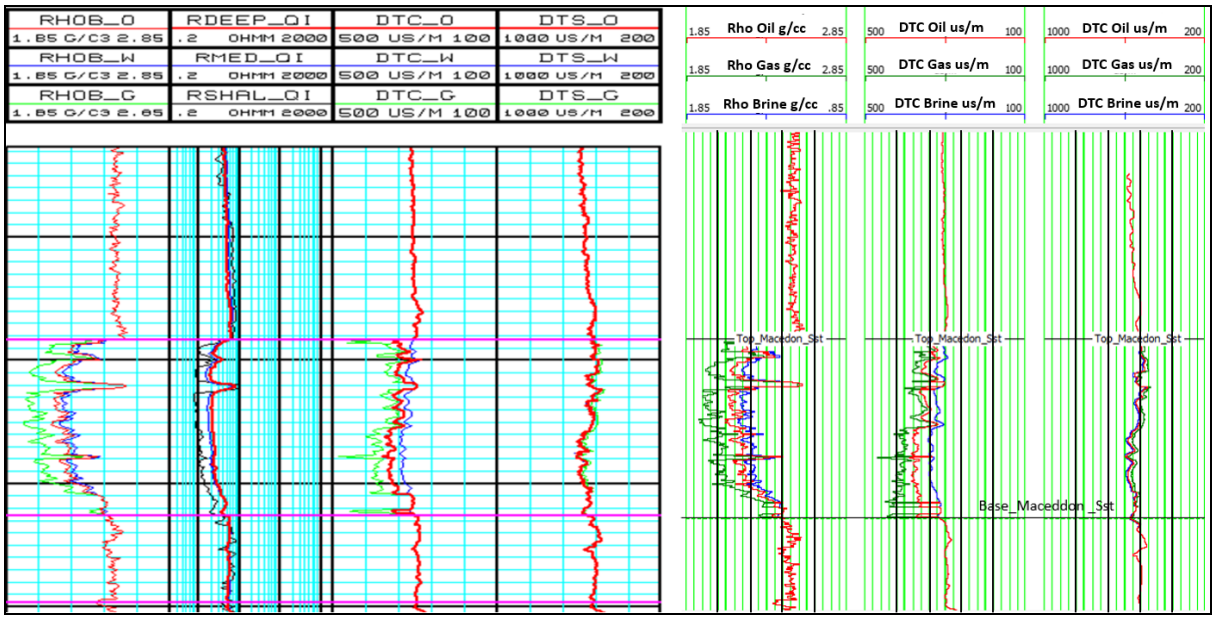

a) b)

Figure 67. a) Fluid substitution modelling for Enfield-2 well conducted by the operator for 100% Gas (green), 100% Oil (red) and 100% Brine (blue) scenarios within the reservoir (Martin, 2002). b) Fluid substitution modelling for Enfield-2 well conducted as QC procedure using public data. Black highlighted vertical lines correspond to blue vertical lines on a for scale references.

The pressure changes have two impacts on the reservoir rocks. The first is the effective stress changes leading to changes in the frame stiffness and hence in Vp and Vs which are described in the thesis in much detail. The second is the fluid acoustic properties, which may also change with pore pressure.

The pressure increase was modelled as the QC to quantitatively assess the effect on the fluid properties of the reservoir. The pressure modelling was done for the change of reservoir pressure from the initial value of 3,220psi to 4,270psi as the maximum increased pore pressure for the Enfield field. The modelling was done with the same parameters as were used for fluid substitution modelling.

First, the calculations for a single point were executed in Seismic Petrophysics Worksheets using Bazle and Wang module (Pennington, 2019) and applying fluid substitution parameters as for Enfield-2 logs (Figure 68). The changes in the output values are negligible.

Second, to test how these fluid changes may affect the Vp, Vs and Density and therefore EEI, the modelling of the above pressure change was simulated in Hampson Russell software applying fluid substitution parameters as for Enfield-2 (Figure 69). The logs were modelled for 100% Gas (Pure Gas), 100% Oil and 100% Brine scenarios for pressure 3,220psi and the same scenarios for pressure 4,270psi. The effect of pressure change on fluid properties is not visible on the logs display for all scenarios as the changes are minuscule.

Inputs		
Temperature	66	°C
Pressure	3,220	(psi)
Gas gravity	0.62	s.grav.
Gas-Oil Ratio	248	(scf/stb)
Oil Gravity	22	°API
Brine salinity	38,000	(ppm)

Results:		
Gas Density:	0.16	g/cm3
Gas Modulus:	47	MPa
Dead Oil Density:	0.90	g/cm3
Dead Oil Modulus:	1,812	MPa
Max GOR for this Oil:	469	scf/stb
Live Oil (max) Density:	0.78	g/cm3
Live Oil (max) Modulus:	1,050	MPa
Live Oil (spec) Density:	0.82	g/cm3
Live Oil (spec) Modulus:	1,290	MPa
Brine Density:	1.016	g/cm3
Brine Modulus:	2,691	MPa
Max GWR for this Brine:	13	scf/stb
Live Brine Modulus:	2,418	MPa

Inputs		
Temperature	66	°C
Pressure	4,270	(psi)
Gas gravity	0.62	s.grav.
Gas-Oil Ratio	248	(scf/stb)
Oil Gravity	22	°API
Brine salinity	38,000	(ppm)

Results:		
Gas Density:	0.20	g/cm3
Gas Modulus:	71	MPa
Dead Oil Density:	0.90	g/cm3
Dead Oil Modulus:	1,916	MPa
Max GOR for this Oil:	658	scf/stb
Live Oil (max) Density:	0.76	g/cm3
Live Oil (max) Modulus:	974	MPa
Live Oil (spec) Density:	0.82	g/cm3
Live Oil (spec) Modulus:	1,385	MPa
Brine Density:	1.019	g/cm3
Brine Modulus:	2,743	MPa
Max GWR for this Brine:	15	scf/stb
Live Brine Modulus:	2,415	MPa

Figure 68. The modelling of the fluid properties change for the initial reservoir 3,220psi and changed by injection 4,270psi pore pressure. The calculations were performed in Seismic Petrophysics Worksheets using Bazle and Wang models module (Pennington, 2019).

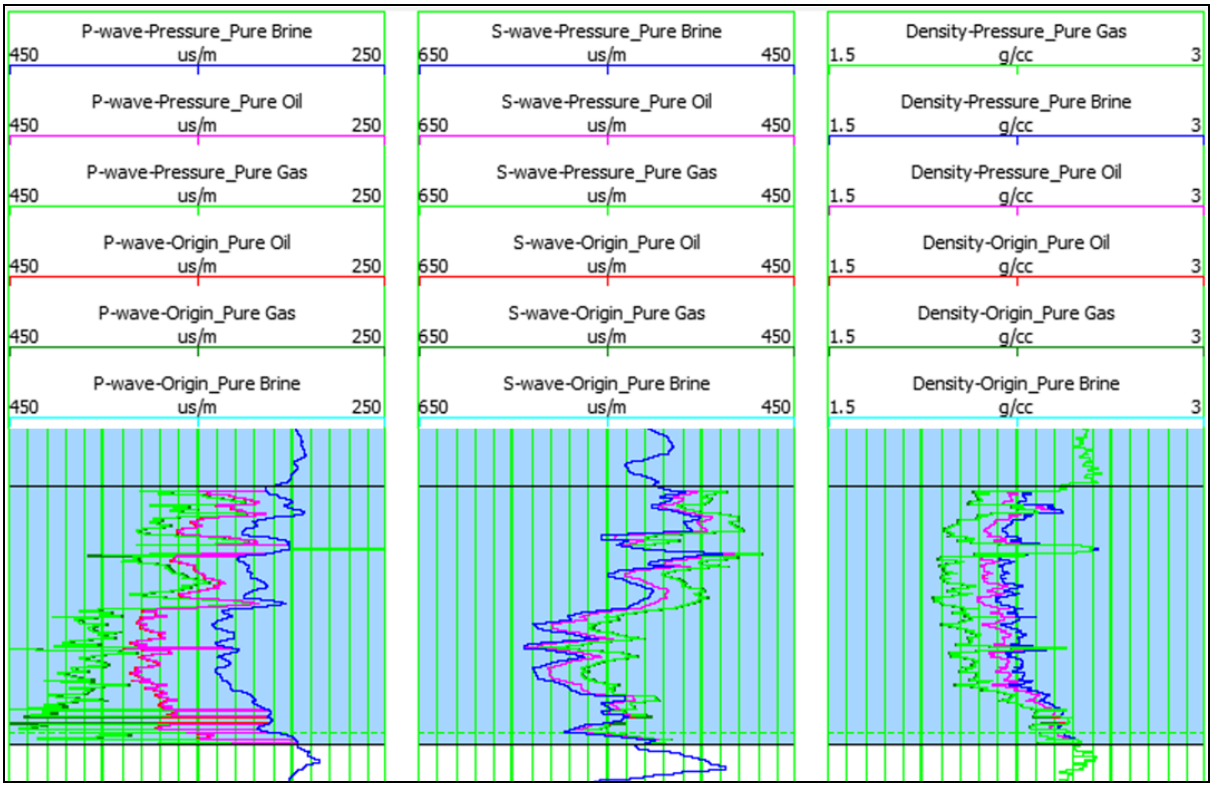

Figure 69. Pressure changes were modelled for 100% Gas (Green), 100% Oil (Red) and 100% Brine (Blue) scenarios. The top three curves in the header area are with initial pressure reservoir pressure of 3,220psi and they are at the top and visible in the curve section Gas (Light green), Oil (Magenta) and Brine (Dark blue) for each Vp (P-wave), Vs (S-wave) and Density. The three bottom curves section Gas (Dark green), Oil (Red) and Brine (Light blue) are for pressure 4,270psi and they are not visible due to small changes for the Vp, Vs and Density logs.

B 3.0 Comparing pressure and saturation changes with the results from the operator

Another QC test is to compare the results from EEI method with the technique used by the operator (Woodside Energy) for Enfield for pressure and saturation changes in the field development process. The company used the same surveys processed in the same way as used in this project after completing the Monitor 2007 survey (Smith, 2008).

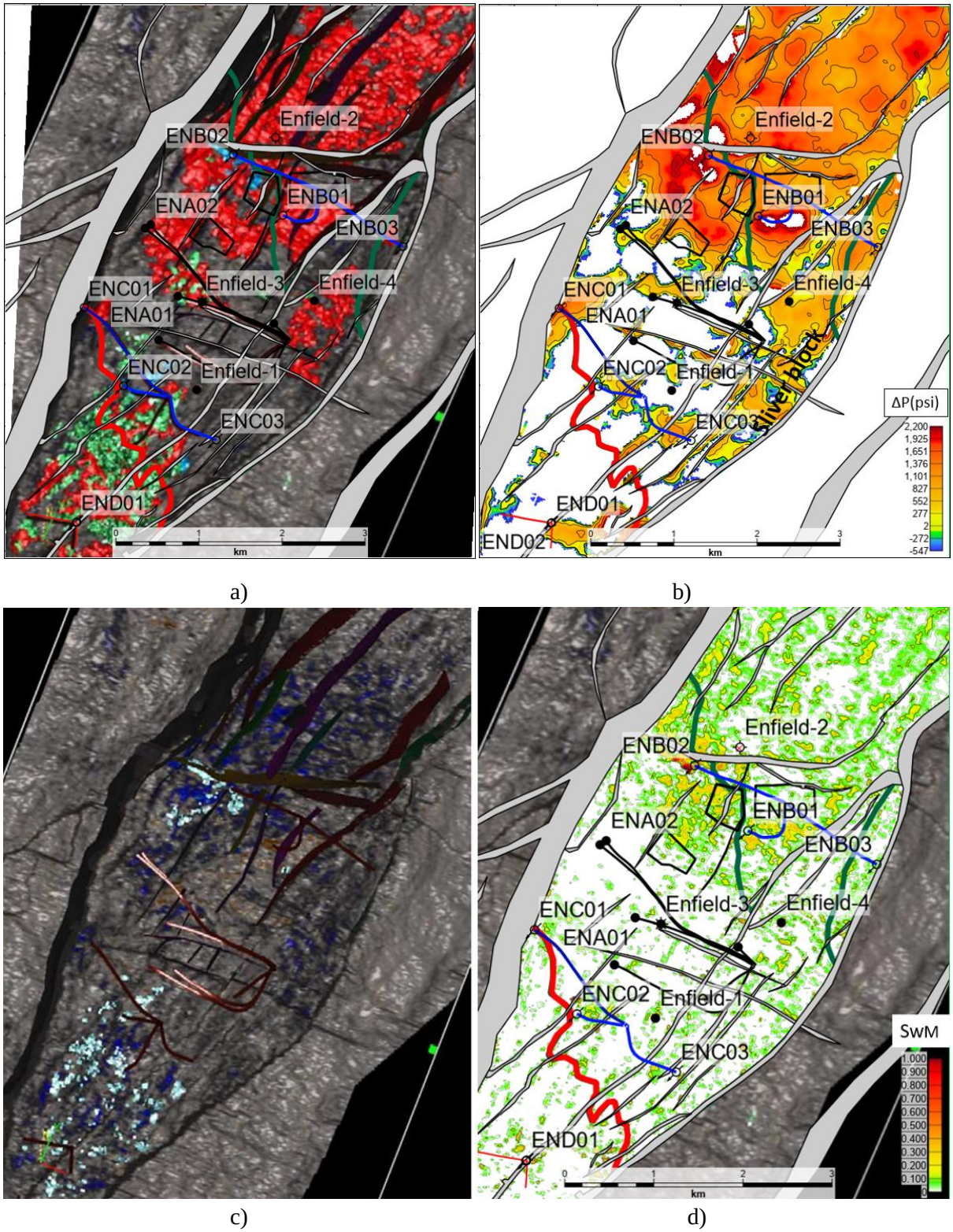

Figure 70. a) Reservoir pressure change (red) and c) water saturation change (blue) map using volume interpretation based on Acoustic Impedance and Poisson Ratio cross-plotting performed by an operator (Woodside Energy) modified from Smith (2008). b) Reservoir fluid-pressure change ΔP (psi). Contour interval ΔP=500 psi. The thick contour is 0. d) Movable-oil-saturation change ΔSwM.

Solid highlighted contour ΔSwM = 0.1 The red line is the GOC and the green is the OWC. The white colour on (b) and (d) represents null values. The maps are geographically rectified.

Two reservoir pressure and saturation change maps are presented in Figure 70. The operator's pressure change (red) map (Figure 70a) was calculated using volume interpretation based on Acoustic Impedance and Poisson Ratio cross-plotting (Smith, 2008). Both maps show a surprisingly good match, particularly coincidental pressure anomaly over the Sliver block that was penetrated by producer well up-dip of ENC05 in 2008 (Figure 39) to recover unswept oil from this block (Hamson, 2012). Another interesting high-pressure area north of Enfield-2 is evident on both maps. The pressure build-ups around all injector wells are better localised in Figure 70b including around gas injectors END01 and END02.

There are only a few saturation change anomalies (light blue) on the operator's map (Figure 70c). The anomaly around injector ENB02 coincides with high saturation, close to 100% of movable-oil saturation change. As modelling shows, the saturation change anomalies less than 50% of the maximum, are not reliable due to low signal-noise ratio. Also, the seven months of oil production did not change much the oil saturation within the field.

APPENDIX C

Published papers author's contribution

Acknowledgement of contribution for a paper: "Shevchenko, S., and W. D. Pennington, 2022, Pressure and Saturation Changes Estimated From Extended Elastic Impedance Properties Using Time-Lapse Seismic Data: Enfield field, NW Australia", The Leading edge, 41(11): 777-785, DOI:10.1190/tle41110777.1.

Author	Conceptualisation	Methodology	Software	Formal Analysis	Investigation	Resources	Data Curation	Supervision	Project administration	Writing - Original Draft	Writing - Review and Editing	Visualisation	Acknowledgement of contribution (signature)
Sergey Shevchenko		x	x	x	x	x	x		x	x	x	x	
Wayne D. Pennington	x	x		x	x			x			x		

Acknowledgement of contribution for a paper: "Shevchenko, S and W., D., Pennington, 2023, Extended Elastic Impedance concept as a simple tool to monitor producing reservoirs", Australian Exploration Geoscience Conference, Extended abstract, Brisbane 2023, https://doi.org/10.5281/zenodo.7980186.

Author	Conceptualisation	Methodology	Software	Formal Analysis	Investigation	Resources	Data Curation	Supervision	Project administration	Writing - Original Draft	Writing - Review and Editing	Visualisation	Acknowledgement of contribution (signature)
Sergey Shevchenko		x	x	x	x	x	x		x	x	x	x	
Wayne D. Pennington	x	x		x	x			x			x		

Bibliography

Aki, K., and P. G. Richards, 1980, Quantitative Seismology: Theory and Methods, Freeman, San Francisco.

Alebouyeh, M., and A. Chehrazi, 2018, Application of extended elastic impedance (EEI) inversion to reservoir from non reservoir discrimination of Ghar reservoir in one Iranian oil field within Persian Gulf: Journal of Geophysics and Engineering, **15**, 1204–1213.

Ali, A., L. Taggart, B. Mee, M. Smith, A. Gerhardt and L. Bourdon, 2008, Integration 4D seismic data with production related effects at Enfield, North West Shelf, Australia: 2008 SPE APOGCE.

Avseth, P., T. Murkerji and G. Mavko, 2005, Quantitative seismic interpretation, Cambridge University Press.

Avseth, P., and N. Skjei, 2011, Rock physics modelling of static and dynamic reservoir properties; A heuristic approach for cemented sandstone reservoirs: The Leading Edge, **30**, 90–96. https://doi.org/10.1190/1.3535437.

Ball, V., L. Tenorio, C. Schiott, M. Thomas, and J. P. Blangy, 2018, Three-term amplitude-variation-with-offset projections, Geophysics, **83**, 51–65, https://doi.org/10.1190/geo2017-0763.1.

Batzle, M. L. and Wang, Z. 1992, Seismic properties of pore fluids. Geophysics, 57, 1396-1408, https://doi.org/10.1190/1.1443207.

Bentley, R., 2010, Simultaneous analysis of the seismic time shifts and amplitude changes due to water Injection, Curtin University of Technology, Department of Exploration Geophysics, Report GPH 4/10.

Bortfeld, R., 1961, Approximations to the Reflection and Transmission Coefficients of Plane Longitudinal and Transverse Waves, Geophysical Prospecting, **9**, 485–502, https://doi.org/10.1111/j.1365-2478.1961.tb01670.x.

Brevik, I., 1999, Rock model-based inversion of saturation and pressure changes from time-lapse seismic data, 69th Annual International Meeting: Society of Exploration Geophysics, 1044–1047.

Bussell, M.R., D. Jablonski, T. Enman, M. J. Wilson, and A. N. Bint, 2001, Deepwater Exploration: North Western Australia compared with Gulf of Mexico and Mauritania, The APPEA Journal, **41** (1), 289–319.

Chakraborty, S., R. Chatterjee, and A. Yadav, 2020, Time lapse rock physics template and seismic quantitative analysis amid the production phase: Journal of Applied Geophysics, 174, 103956, https://doi.org/10.1016/j.jappgeo.2020.103956.

Chan, C., J. Sun, S. Birdus, K. M. Lee, O. Tang, and M. Wang, 2008, CGGVeritas, Veritas Geophysical (Asia Pacific) Pty Ltd, Enfield 4D Survey, Nortwest Cape, Western Australia, Seismic Data processing Report.

Cole, S., D. Lumley, M. Meadows, and A. Tura, 2002, Pressure and saturation inversion of 4D seismic data by rock physics forward modelling: 72nd Annual International Meeting: Society of Exploration Geophysics, Expanded Abstracts, pp. 2475–2478.

Connolly, P., 1999, Elastic impedance: The Leading Edge, **18**, 438–452, https://doi.org/10.1190/1.1438307.

Connolly, P., 2010, Robust Workflows for Seismic Reservoir Characterisation, SEG distinguished lectures.

Dai, X., and L. Mei, 2014, Time-lapse extended elastic impedance application in estimation of fluid saturation and pressure changes: International Geophysical Conference & Exposition, SEG and CPS, Global Meeting Abstracts, 974–977, https://doi.org/10.1190/IGCBeijing2014-246.

Dong, W., 1996, A sensitive combination of AVO slope and intercept for hydrocarbon indication, Conference Proceedings, 58th EAGE Conference and Exhibition, https://doi.org/10.3997/2214-4609.201408728.

Duffy, J., and R. D. Mindlin, 1957, Stress–strain relations and vibrations of a granular media: Journal of Applied Mechanics, Transactions ASME, X, 585–593.

DUG Insight, 2021, Windows/Linux/Mac. Perth, Western Australia: DUG Technology Ltd (http://www.dug.com).

Eiken, O., G. Geir, U. Haugen, M. Schonewille and A. Duijndam, 2003, A proven method for acquiring highly repeatable towed streamer seismic data, Geophysics, **68**, 1303–1309, https://doi.org/10.1190/1.1598123.

Gardner, G. H. F., L. W. Gardner and A. R. Gregory, 1974, Formation velocity and density—The diagnostic basics for stratigraphic traps, Geophysics, **39**, 770–780, https://doi.org/10.1190/1.1440465.

Gassman, F., 1951, Elastic waves through a packing of spheres, Geophysics, **16**, 673–685, https://doi.org/10.1190/1.1437718.

Geertsma, J., and D. C. Smith, 1961, Some Aspects of Elastic Wave Propagation in Fluid-Saturated Porous Solids, Geophysics, **26**, 169–181, https://doi.org/10.1190/1.1438855.

Hamson, G., 2012, Leveraging 4D Seismic and Production Data to Advance the Geological Model of the Enfield Oil Field, Western Australia, Search and Discovery Article 20172, Adapted from oral presentation at AAPG Annual Convention and Exhibition, Long Beach, California, April 22–25.

Han, W., 2004, Permits: WA-271-P, Area: North West Cape of Western Australia, Survey: Enfield 2004 3D, Data processing report, WesternGeco, June 2004.

Hendrickson, J., 1999, Stacked: Geophysical Prospecting, **47**, 663–706, https://doi.org/10.1046/j.1365-2478.1999.00150.x.

Hicks, W. G., and J. E. Berry, 1956, Application of continuous velocity logs to determination of fluid saturation in reservoir logs, Geophysics, **21**, 739–754, https://doi.org/10.1190/1.1438267.

Jack, I., 2017, 4D seismic – Past, present, and future, The Leading Edge, **36**, Issue 5, 370–456, https://doi.org/10.1190/tle36050386.1.

Johnston, D. H, 2013, Practical Applications of Time-Lapse Seismic Data, Society of Exploration Geophysicists, https://doi.org/10.1190/1.9781560803126.

Koster, K., P. Gabriels, M. Hartung, J. Verbeek, G. Deinum, and R. Staples, 2000, Time–lapse seismic surveys in the North Sea and their business impact: The Leading Edge, 19, 290–299.

Kragh, E., and P. Christie, 2001, Seismic repeatability, normalized rms, and predictability: SEG International Exposition and Annual Meeting, San Antonio, Texas, September 9–14.

Kragh, E., and P. Christie, 2002, Seismic repeatability, normalized rms, and predictability: The Leading Edge, **21**, 640–647, https://doi.org/10.3997/2214-4609-pdb.5.a015.

Landro, M., 1999, Discrimination between pressure and fluid saturation changes from time lapse seismic data: 69th Annual International Meeting: Society of Exploration Geophysics, Expanded Abstracts, 1651–1654, https://doi.org/10.1190/1.1820848.

Landro, M., 2001, Discrimination between pressure and fluid saturation changes from time–lapse seismic data: Geophysics, **66**, 836–844, https://doi.org/10.1190/1.1444973.

Longley., I. M., C. Buessenschuett, L. Clydsdale, C. J. Cubitt, R. C. Davis, M. K. Johnson, N. M. Marshall, A. P. Murray, R. Somerville, T. B. Spry and N. B. Thompson, 2002, The North West Shelf of Australia – a Woodside perspective, The Sedimentary Basins of WA, v. 3, AAPG.

Lumley, D., M. Meadows, S. Cole, and D. Adams, 2003, Estimation of reservoir pressure and saturations by crossplot inversion of 4D seismic attributes: 73rd Annual International Meeting, SEG, Expanded Abstracts, 1513–1516.

MacBeth, C., 2004, A classification for the pressure–sensitivity properties of a sandstone rock frame, Geophysics, **69**, 497–510, https://doi.org/10.1190/1.1707070.

Macpherson, S. D., 2009, AVO, Inversion, and Attributes: Principles and Applications, PetroSkills Course, PetroSkills, LLC, 2009.

Martin, P., 2002, WA271P well log summaries, NOPIMS database, Enfield-4, ID - D00018561.

McFadzean, G., 2006, Seismic Interpretation report, WA-28-L, Enfield 3D Marine Seismic Survey, Exmouth Sub-Basin, Woodside Company Report.

Meadows, M., D. Adams, R. Wright, A. Tura, S. Cole and D. Lumley, 2002, Rock physics analysis for time–lapse seismic at Schiehallion Field, North Sea, SEG International Exposition and 72nd Annual Meeting, Salt Lake City, Utah, October 6–11.

Merkel, R. H., R. D. Barree and G. Towle, 2001, Seismic response of Gulf of Mexico reservoir rocks with variations in pressure and water saturation: The Leading Edge, **20**(3), 286–293.

Murphy, J. A, 1952, Good Field Data are Necessary for Good Reservoir Engineering, The Petroleum Engineer, v. 24, B-91–B-99.

Richards, P. G., and C. W. Frasier, 1976, Scattering of elastic wave from depth-dependent inhomogeneities, Geophysics, 41, 441–458, https://doi.org/10.1190/1.1440625.

Saul, M., and D. Lumley, 2015, The combined effects of pressure and cementation on 4D seismic data, Geophysics, **80**, No. 2, WA135–WA148, https://doi.org/10.1190/geo2014-0226.1.

Sayers, C. M,. 2007, Asymmetry in the time-lapse seismic response to injection and depletion, Geophysical Prospecting, **55**, 699–705, https://doi.org/10.1111/j.1365-2478.2007.00636.x.

Sheriff, R. E., and L. P. Geldart, 1995, Exploration seismology (2nd Edn). Cambridge University Press.

Shevchenko, S., and W. D. Pennington, 2022, Pressure and Saturation Changes Estimated From Extended Elastic Impedance Properties Using Time-Lapse Seismic Data: Enfield field, NW Australia, The Leading edge, **41**(11): 777-785, DOI:10.1190/tle41110777.1.

Shevchenko, S and W., D., Pennington, 2023, Extended Elastic Impedance concept as a simple tool to monitor producing reservoirs, Australian Exploration Geoscience Conference, Extended abstract, Brisbane 2023, https://doi.org/10.5281/zenodo.7980186.

Shuey, R. T., 1985, A simplification of the Zoepprtz equations. Geophysics, **50**, 609–614, https://doi.org/10.1190/1.1441936.

Simm, R., and M. Bacon, 2014, Seismic Amplitude An Interpreter's Handbook, Cambridge University Press.

Smith, M., A. Gerhardt, B. Mee, T. Ridsdill-Smith, A. Wulff, and L. Bourdon, 2008, The Benefits of Early 4D Seismic Monitoring to Understand Production Related Effects at Enfield, North West Shelf, Australia: SEG Las Vegas 2008 Annual Meeting, 3159–3163, https://doi.org/10.1190/1.3064002.

Smith, M., 2008, Enfield 4D Monitor 1 2007 Interpretation Report, Woodside Company Report.

Tindale, K., N. Newell, J. Keall, and N. Smith, 1998, Structural evolution and charge history of the Exmouth Sub-basin, northern Carnarvon Basin, Western Australia, in Purcell, P. G., and R. R. Purcell, (Eds), The Sedimentary Basins of Western Australia 2: Proceedings of the Petroleum Exploration Society of Australia, Perth, 447–472.

Tura, A., and D. E. Lumley, 1999, Estimating pressure and saturation changes from time-lapse AVO data: 69th Annual International Meeting, SEG, Expanded Abstracts, 1655–1658, https://doi.org/10.3997/2214-4609.201407758.

Vernik, L., 2016, Seismic Petrophysics in Quantitative Interpretation, SEG, Investigations in geophysics No. 18.

Whitcombe, N. D., and J. G. Fletcher, 2001, The AIGI crossplot as an aid to AVO analysis and calibration, SEG International Exposition and Annual Meeting, San Antonio, Texas, September 9–14, 2001, https://doi.org/10.1190/1.1816574.

Whitcombe, N. D., 2002, Short Note Elastic impedance normalization: Geophysics, **67**, 60–62, https://doi.org/10.1190/1.1451331.

Whitcombe, N. D., P. A. Connolly, R. L. Reagan and T. C. Redshaw, 2002, Extended elastic impedance for fluid and lithology prediction, Geophysics, **67**, 63–67, https://doi.org/10.1190/1.1815660.

Wickham, J., B. Burmaz, L. Abzalov and S. Malajczuk, 2007, PGS Data Processing A/P Pty. Ltd. Data Processing Report 4D seismic survey Enfield 4D Northwest Cape, Western Australia for Woodside Energy Limited.

Willis, S., 1999, Enfield-1 well completion report (Basic Data), WA-271-P, Carnarvon Basin, Woodside Company Report.

Willis, S., 1999, Enfield-2 well completion report (Basic Data), WA-271-P, Carnarvon Basin, Woodside Company Report.

Willis, S., 2001, Enfield-3 well completion report (Basic Data), WA-271-P, Carnarvon Basin, Woodside Company Report.

Willis, S., 2002, Enfield-4 well completion report (Basic Data), WA-271-P, Carnarvon Basin, Woodside Company Report.

Willis, S., 2003, Enfield-5 well completion report (Interpretive Data), WA-271-P, Carnarvon Basin, Woodside Company Report.

Wulff, A., A. Gerhardt, T. Ridsdill-Smith and M. Smith, 2008, The role of rock physics for the Enfield 4D seismic monitoring project. Exploration Geophysics, **39**, 108–114, https://doi.org/10.1071/eg08015.

Zoeppritz, K., 1919, Erdbebenwellen VIIIB. ŰberReflexion und Durchgang seismischer Wellen durch Ustetigkeitsflα̈chen, Gôttinger Nachrichten, I, 66–84.